J. Mech. Phys. Solids 208 (2026) 106430

Contents lists available at ScienceDirect

Journal of the Mechanics and Physics of Solids

journal homepage: www.elsevier.com/locate/jmps

Wrinkling mechanics of immersed magneto-active hydrogels

Guozhan Xia [a,b,*], Renwei Mao [c,d], Weiqiu Chen [c,d,e], Yipin Su [c,d,*]

[a] Department of Mechanics and Aerospace Engineering, Southern University of Science and Technology, Shenzhen 518055, China
[b] Department of Civil, Environmental and Mechanical Engineering, University of Trento, Trento 38123, Italy
[c] Huanjiang Laboratory, Zhuji 311800, China
[d] Department of Engineering Mechanics, Zhejiang University, Hangzhou 310027, China
[e] Faculty of Mechanical Engineering and Mechanics, Ningbo University, Ningbo 315211, China

ARTICLE INFO

Keywords:
Magneto-active hydrogel
Wrinkling instability
Geometric constraint
Surface impedance matrix method
Finite deformation

ABSTRACT

This study explores the tunable wrinkling of a magneto-active hydrogel (MAH) block immersed in a tank filled with a magnetic solvent. An electromagnet, with two poles positioned at the top and bottom of the tank, generates a uniform magnetic biasing field via energized coils. Within the framework of nonlinear magneto-elastic theory and non-equilibrium thermodynamics of hydrogels, the mechanical behaviors of small-amplitude wrinkling are modeled, incorporating the influence of external Maxwell stress. By employing the surface impedance matrix method combined with the Stroh formulation, the bifurcation relations governing wrinkling onset are decoupled into symmetric and antisymmetric modes. For the first time, explicit expressions are established in a compact form for compressible soft materials with general free energy functions. As representative examples, generalized neo-Hookean and Gent ideal MAH blocks are examined. Numerical results show that blocks with a smaller permeability than that of the surroundings (i.e., the normalized permeability $\overline{\mu} < 1$), exhibit wrinkling behaviors largely similar to those without an external magnetic field, albeit with minor differences in certain details. Notably, a distinct "mutation" in wrinkling is observed for extremely thick blocks, which is attributed to a geometric constraint associated with the normalized thickness of the block relative to the tank. However, for blocks with higher permeability ($\overline{\mu} > 1$), the tensile Maxwell stress significantly destabilizes the system, resulting in distinct wrinkling patterns that differs from those in low-permeability blocks. Intriguingly, wrinkling can emerge during the simultaneous thickening and area expansion of the block, but this phenomenon may be suppressed by geometric constraints. These findings offer valuable insights into the behavior of magneto-active hydrogels, potentially advancing their theoretical understanding and practical applications.

1. Introduction

Magneto-active hydrogel (MAH) typically consists of a crosslinked polymer network and solvent molecules, with magnetic particles of varying sizes distributed either randomly or in an orderly manner. It is not only capable of undergoing large deformations in response to an external magnetic field but is also characterized by excellent biocompatibility, lower toxicity, smaller elastic modulus, tissue-like higher fluid content and permeability. In the last few decades, it has emerged as a novel smart material with tunable physical properties (Li et al., 2013; Wu et al., 2011), offering a wide range of practical applications, including magneto-responsive soft

* Corresponding authors.
E-mail addresses: xiagz@sustech.edu.cn (G. Xia), su_yp@zju.edu.cn (Y. Su).

https://doi.org/10.1016/j.jmps.2025.106430
Received 7 July 2025; Received in revised form 16 November 2025; Accepted 18 November 2025
Available online 24 November 2025
0022-5096/

robotics (Chen et al., 2023; Chen et al., 2019), deformable actuators and sensors (Khan et al., 2020; Rotjanasuworapong et al., 2023), pollutant absorption/adsorption for environmental improvement (Meng et al., 2019; Yu et al., 2013), and biomedical devices for drug delivery and medical diagnosis (Jahanban-Esfahlan et al., 2020; Liu et al., 2021; Zhao et al., 2011).

The application of mechanical and magnetic loads on MAH may introduce the risk of instability and potential failure, even as it enables the related devices to achieve exceptional performance. Apart from its unique solvent diffusion characteristics, MAH can be considered a magneto-responsive elastomer composed of a soft polymeric matrix and embedded magnetic dopants. It was early recognized on that magnetic-elastic structures buckle when subjected to a certain magnitude of magnetic field (Miya et al., 1978; Moon and Pao, 1968). Recently, such instability has been exploited to achieve active control of deformation patterns for both academic interests and practical purposes (Goshkoderia et al., 2020; Hou et al., 2018; Psarra et al., 2017; Psarra et al., 2019). For example, Psarra et al. (2017, 2019) investigated the induction of wrinkling and crinkling on the surface of a thin magnetorheological elastomer (MRE) film placed on a soft passive substrate by tuning the combination of uni-axial pre-compression and magnetic field (see Fig. 1). Inspired by their experimental observations, Wu and Destrade (2021) revisited the wrinkling instability of incompressible soft magneto-active plates from the theoretical aspect. They first derived the Stroh formulation of the governing equations for wrinkling problem and then used the surface impedance matrix method to obtain explicit expressions of the bifurcation equations. Most recently, Xia (2024) has promoted this method to better grasp the impact of compressibility on wrinkling of magnetic soft plates. They suggested that a perfectly incompressible model may not accurately represent the behaviors of a nearly incompressible plate under plane-strain loading, particularly when the permeability of the plate is exceeds that of its surroundings. It is worth noting that, in the works mentioned above, magneto-active media are typically placed in vacuum or a fixed passive environment. The potential coupling between the media and dynamic, active environments has received less attention. Therefore, investigating the instability behaviors of MAHs in liquid surroundings with tunable properties becomes particularly intriguing. Unique challenges arise in both physical and mathematical aspects, such as the complexity of modeling interactions at the solid-liquid interface.

As depicted in Fig. 2(a), this study investigates the wrinkling of an MAH block immersed in a magnetic solvent with permeability μ_f and chemical potential Φ_c. Following Rosensweig's theory, the surrounding fluid is modeled as a homogeneous and mechanically passive continuum with an effective, field-independent permeability (Rosensweig, 1985). To ensure uniform magnetoelastic coupling in the MAH, the magnetic components and the polymer network are assumed to be connected by covalent bonds—a condition achievable experimentally through methods like the grafting-onto technique (Li et al., 2013). Under these conditions, the application of a magnetic field generates Maxwell stress without altering the rheological properties of either the solvent or the MAH block, both of which exhibit isotropic and homogeneous properties. These assumptions have also been implicitly adopted by many other researchers (Ahmadinejad and Marshall, 2024; Gebhart and Wallmersperger, 2019; Liu et al., 2023; Tang et al., 2025).

Using a virtual dry state as the reference, the polymer network expands isotropically by a stretch λ_0 when immersed in the solvent, forming a gel block in a free swelling state with thickness L_g and permeability μ_g. Under mechanical loading in the x_1-x_2 plane and a

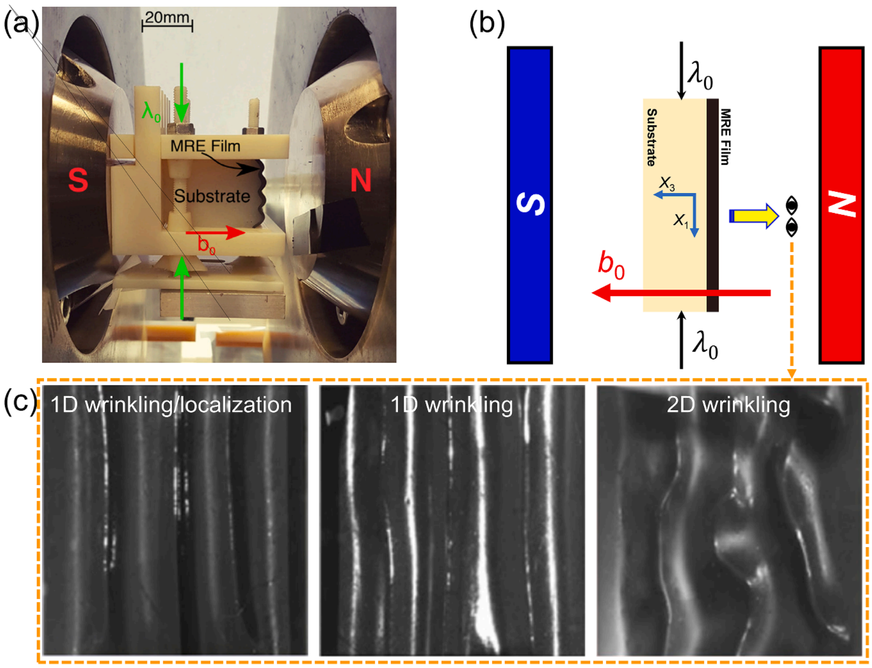

Fig. 1. An experimental study of the wrinkling of a magnetic soft film subjected to a transverse magnetic field, reproduced from Psarra et al. (2019). (a) A pre-compressed MRE film wrinkles under a magnetic biasing field generated by two poles of the electromagnet when bonded to a soft passive substrate. (b) Schematic diagram for the experimental setting for magnetic-induced wrinkling of the film-substrate system shown in (a). (c) Representative morphologies of wrinkling observed on the surface of the MRE film under three typical domains of pre-compression.

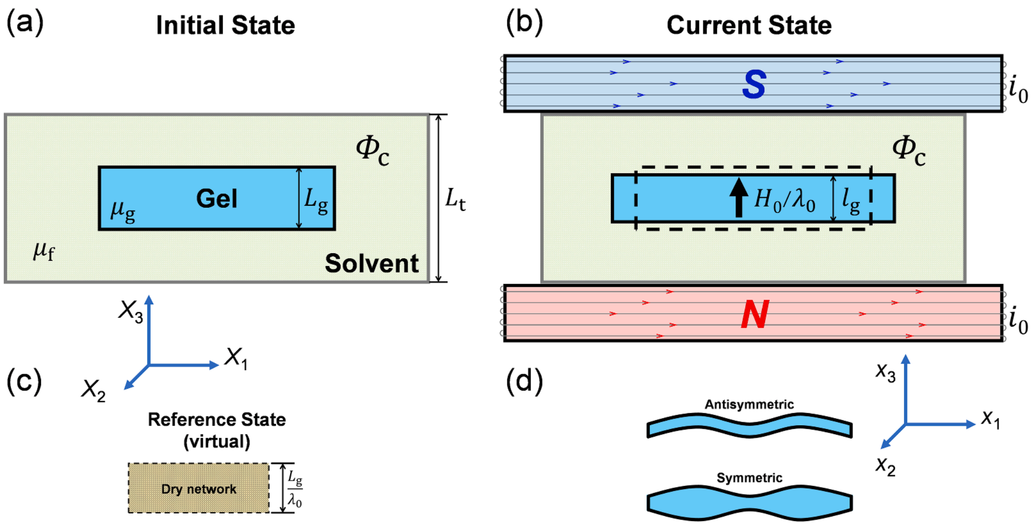

Fig. 2. A rectangular MAH block is immersed in a tank filled with a magnetic solvent. (a) In the free swelling state, the top and bottom faces of the tank are covered by films with perfect diamagnetism. (b) The block is activated by an in-plane mechanical loading (not displayed here) and a nominal transverse magnetic field intensity H_0, produced by energized coils carrying free current density i_0. (c) The virtual dry network of the gel is shown. (d) Antisymmetric and symmetric wrinkling are sketched for illustration. The gel block, with an initial thickness of L_g, and the solvent have permeabilities of μ_g and μ_f, respectively. The chemical potential of the solvent Φ_c and the distance between the top and bottom of the tank L_t are assumed to remain constant, while the thickness of the gel becomes l_g under biasing fields.

uniform magnetic biasing field along the thickness direction, the block further deforms further into a new homogenous state with principal stretches of λ_i ($i = 1, 2, 3$) relative to the dry network reference state. Consequently, the block's thickness becomes

$$l_g = \lambda_3 L_g / \lambda_0. \tag{1}$$

In this work, the magnetic biasing field is specialized to the magnetic field intensity as shown in Fig. 2(b), referred to as the H-controlled mode. The nominal magnetic field intensity H_0 in the block is generated by an electromagnet composed of energized coils with a direct current intensity i_0 (A/m). The radial dimensions of the coils and tank are equal and much larger than the lateral dimensions of the tank, ensuring a uniform magnetic field across the tank. Additionally, the in-plane mechanical loading protocol is quite flexible in practice, encompassing fixed-stretch, dead-load and even stretch-load mixed types. For conciseness, these loading protocols are not displayed in Fig. 2(b). The reader is referred to Xia (2024) for complete depictions.

The magneto-mechanical coupling and nonlinear response of the block are modelled by the nonlinear magneto-elastic theory (Dorfmann and Ogden, 2014). Meanwhile, the diffusion of solvent molecules and their mixing with polymer network in hydrogels are considered by invoking the non-equilibrium thermodynamic theory (Hong et al., 2008). This combination bears partial resemblance to the field theory for polyelectrolyte gels, yet it neglects the contribution of mobile ions to the free energy from the entropy of mixing. It should be recognized that the modelling of MAHs with magneto-chemo-mechanical coupling has advanced significantly beyond the foundation laid by Hong et al. (2008). However, more sophisticated models (Garcia-Gonzalez and Landis, 2020; Gebhart and Wallmersperger, 2019; Liu et al., 2017) are unnecessary for the current study, which focuses on obtaining *benchmark* solutions of wrinkling predictions. Without loss of generality, we assume that all biasing fields are applied slow enough that the gel remains in an equilibrium state. The effects of related time-dependent behaviors (Galli and Comley, 2009; Kaufman et al., 2008; Liu et al., 2009) can be tentatively compromised, although the phenomenological poroelastic parameters has been correlated to the thermodynamic properties of gels using the Flory-Huggins theory in the energy function (Hong et al., 2008). It should also be noted that the difference in permeability between the MAH block and the solvent may induce a nonuniform magnetic field near the block-solvent interface, particularly at the lateral boundary of the block. This phenomenon, recognized as an unexpected edge/shape effect, could lead to an underestimation of transverse magnetic components (Stewart and Anand, 2025). To mitigate this issue, the lateral dimensions of the block have been designed to be significantly larger than its thickness, thereby allowing the influence of such effects be reasonably neglected.

In the present study, we adopt the general framework of the Stroh formulation and surface impedance matrix method, as proposed for compressible magnetoelastic soft plates (Xia, 2024), as analytical tools to predict the onset of wrinkling in immersed magneto-active hydrogels. While the general solution to the governing equations remains unchanged, the intrinsically distinct conditions of this problem—such as the size effect induced by geometric constraints and the chemical potential difference between the gel and the solvent—introduce unique considerations, resulting in novel and highly tunable wrinkling behaviors. The remainder of the paper is organized as follows.

In Section 2, we present the governing equations for the equilibrium of a MAH block subjected to in-plane mechanical loading and a transverse magnetic biasing field. The nonlinear response of the constrained swelling block is first derived in terms of the true magnetic induction field, which is consistently followed in all subsequent equations unless stated otherwise. Naturally, these equations can be specialized to the specific set-up of magnetic protocols as shown in Fig. 2(b) without any difficulty.

Then, in Section 3, we present analytical bifurcation relations for the antisymmetric and symmetric wrinkles of the MAH block, respectively. Extending far beyond earlier works (Wu and Destrade, 2021; Xia, 2024), explicit expressions are derived based on general compressible models. Two special limits of the thin-plate (long-wave) and thick-plate (short-wave) are examined to identify the so-called global and wavelength-independent instability domains for MAH blocks with specific dimensions.

In Section 4, we perform numerical discussions for constrained swelling neo-Hookean and Gent ideal MAH blocks subjected to a transverse magnetic biasing field. For the magnetic loading protocol, critical curves for the onset of wrinkling under certain magnetic biasing fields are plotted in terms of normalized current. Finally, in Section 5, we present the conclusions of our study, discuss its limitations, and outline potential implications.

2. Large actuation of immersed MAH blocks

We begin by considering the magnetic biasing field applied to the MAH block and assume the nominal magnetic field intensity in the block to be H_0. According to the Ampère's circuital law, which relates magnetic field intensity to free current, we derive the following equations:

$$H_0 L_g/\lambda_0 + H_3^*\left(L_t - l_g\right) = i_0 L_t, \tag{2a}$$

or, alternatively,

$$H_0\left[(1-\overline{\mu})L_g/\lambda_0 + \overline{\mu}L_t/\lambda_3\right] = i_0 L_t, \tag{2b}$$

where H_3^* denotes the magnetic field intensity in the solvent and $\overline{\mu} = \mu_g/\mu_f$ is a nondimensional measure of permeability, referred to as normalized permeability. Here and throughout the text, the superscript "$*$" is used to denote quantities defined outside the region occupied by the block, i.e., in the solvent.

We then introduce a free energy function $W(\boldsymbol{F}, \boldsymbol{B}_l)$ to describe the constitutive relation of the MAH block, where $\boldsymbol{F}$ is deformation gradient and $\boldsymbol{B}_l$ is nominal magnetic induction. For ease of analysis, six independent invariants for the isotropic gel are defined as functions of $\boldsymbol{F}$ and $\boldsymbol{B}_l$: $I_1 = \mathrm{tr}\boldsymbol{c}$, $I_2 = \left[(\mathrm{tr}\boldsymbol{c})^2 - \mathrm{tr}\boldsymbol{c}^2\right]/2$, $I_3 = \det\boldsymbol{c}$, $I_4 = \boldsymbol{B}_l\cdot\boldsymbol{B}_l$, $I_5 = \boldsymbol{B}_l\cdot(\boldsymbol{c}\boldsymbol{B}_l)$, and $I_6 = \boldsymbol{B}_l\cdot\left(\boldsymbol{c}^2\boldsymbol{B}_l\right)$, where $\boldsymbol{c} = \boldsymbol{F}^{\mathrm{T}}\boldsymbol{F}$ denotes right Cauchy-Green tensor. By invoking the nonlinear theory of magnetoelasticity for a compressible MAH block in equilibrium (Dorfmann and Ogden, 2014), the non-zero components of the Cauchy stress tensor $\boldsymbol{\tau}$ and the true magnetic field intensity $\boldsymbol{H}$ yield

$$\begin{aligned}
\tau_{11} - \tau_{33} &= \frac{2}{J}(b_{11} - b_{33})(W_1 + b_{22}W_2) - 2JB_3^2(W_5 + 2b_{33}W_6),\\
\tau_{22} - \tau_{33} &= \frac{2}{J}(b_{22} - b_{33})(W_1 + b_{11}W_2) - 2JB_3^2(W_5 + 2b_{33}W_6),\\
H_3 &= 2JB_3\left(W_4\lambda_3^{-2} + W_5 + W_6\lambda_3^2\right),
\end{aligned} \tag{3}$$

where $W_m = \partial W/\partial I_m$ for $m = 1, 2, \ldots, 6$, τ_{ii} and b_{ii} ($i = 1, 2, 3$) are the principal component of the total Cauchy stress tensor and the left Cauchy-Green tensor $\boldsymbol{b} = \boldsymbol{F}\boldsymbol{F}^{\mathrm{T}}$ of the block in the x_i-direction, respectively. Additionally, H_3 and B_3 are the only non-zero components of the true magnetic field intensity and the true magnetic induction field in the x_3-direction inside the block, respectively. For more details, the reader is referred to Appendix A. For the considered problem, the deformation gradient simplifies to $\boldsymbol{F} = \mathrm{diag}(\lambda_1, \lambda_2, \lambda_3)$, and the volume ratio $J = \det\boldsymbol{F} = \sqrt{I_3}$ equals to $\lambda_1\lambda_2\lambda_3$. Substituting the last equation of Eq. (3) into Eq. (2) with the magnetic continuity condition across the block-solvent interface, i.e., $B_3^* = B_3$, and the push-forward relation between the true magnetic field intensity and its Lagrangian counterpart, i.e., $\boldsymbol{H} = \boldsymbol{F}^{-\mathrm{T}}\boldsymbol{H}_l$, we rewrite Eq. (2) as

$$\left[2J\left(W_4\lambda_3^{-1} + W_5\lambda_3 + W_6\lambda_3^3\right)L_g\Big/\lambda_0 + \mu_f^{-1}\left(L_t - l_g\right)\right]B_3 = i_0 L_t. \tag{4}$$

Here, we assume that the solvent is ideally magnetic, meaning its magnetic properties remain unchanged under deformation. The connection between H_0 and B_3 is determined by the constitutive relation of the gel.

Assume that the gel block is subjected to in-plane nominal stress s_1 and s_2 in the x_1- and x_2-directions, respectively, while its top and bottom surfaces $x_3 = \pm l_g/2$ are mechanically traction-free. The mechanical continuity condition thus leads to

$$s_1 = J\lambda_1^{-1}\lambda_0^{-2}\left(\tau_{11} - \tau_{11}^*\right),\ s_2 = J\lambda_2^{-1}\lambda_0^{-2}\left(\tau_{22} - \tau_{22}^*\right),\ \tau_{33} = \tau_{33}^*, \tag{5}$$

where the non-zero components of the Maxwell stress tensor in the solvent are given by

$$\tau_{11}^* = \tau_{22}^* = -\tau_{33}^* = -\frac{B_3^2}{2\mu_f}. \tag{6}$$

By combining Eqs. (3) and (6), the nonlinear response of the gel block in three principal directions is derived as

$$
\begin{aligned}
&s_1 = J\lambda_1^{-1}\lambda_0^{-2}\left[\frac{2}{J}(b_{11}-b_{33})(W_1+b_{22}W_2) - 2JB_3^2(W_5+2b_{33}W_6) + \left(\tau_{33}^{*}-\tau_{11}^{*}\right)\right],\\
&s_2 = J\lambda_1^{-1}\lambda_0^{-2}\left[\frac{2}{J}(b_{22}-b_{33})(W_1+b_{11}W_2) - 2JB_3^2(W_5+2b_{33}W_6) + \left(\tau_{33}^{*}-\tau_{22}^{*}\right)\right],\\
&\frac{b_{33}}{J}\left[W_1+W_2(b_{11}+b_{22})\right] + JW_3 + JB_3^2(W_5+2b_{33}W_6) - \frac{B_3^2}{4\mu_{\mathrm{f}}} = 0.
\end{aligned}
\tag{7}
$$

It is noted that, the third expression in Eq. (7) can be used to determine the out-of-plane stretch of the gel under certain basing fields.

3. Wrinkling analysis for immersed ideal MAH blocks

We now consider the wrinkling formation of the immersed MAH blocks using the linearized incremental theory. Although a general framework for wrinkling analysis of compressible magnetoelastic has been preliminarily developed (Xia, 2024), the most general bifurcation relations are often lengthy and cumbersome. Except for the reduced form derived for the simplest neo-Hookean model, directly applying these relations can lead to numerical instability, significantly limiting their practical utility. To overcome this limitation, we further examine the energy function W of the MAH block as mentioned in Section 2, where the first and the third invariants are typically decoupled without loss of generality, i.e., $\partial^2 W/(\partial I_1 \partial I_3) = 0$ (Holzapfel, 2000). Following the standard procedures summarized in Appendix B and assuming surface wrinkles that are harmonic in the x_1-direction, we obtain following explicit expressions for the bifurcation equations of general ideal MAH blocks

$$
\begin{aligned}
\frac{\mathrm{i}(1-\overline{\mu})^2\overline{B}_3^2}{1+\overline{\mu}\tanh(k_{\mathrm{w}}\widetilde{h}/2)\tanh^{\pm1}(k_{\mathrm{w}}l_{\mathrm{g}}/2)} = {}& \frac{\left[\left(\frac{\overline{\mu}}{2}-1\right)\overline{B}_3^2\overline{\eta}_2^{(3)}+\overline{\eta}_4^{(3)}\right]\left(\frac{\overline{\mu}}{2}\overline{B}_3^2-\overline{\eta}_5^{(2)}\right)}{\left(\overline{\eta}_4^{(2)}\overline{\eta}_2^{(3)}-\overline{\eta}_4^{(3)}\overline{\eta}_2^{(2)}\right)}\left[\frac{\tanh(k_{\mathrm{w}}l_{\mathrm{g}}r_2/2)}{\tanh(k_{\mathrm{w}}l_{\mathrm{g}}/2)}\right]^{\pm1}\\
&-\frac{\left[\left(\frac{\overline{\mu}}{2}-1\right)\overline{B}_3^2\overline{\eta}_2^{(2)}+\overline{\eta}_4^{(2)}\right]\left(\frac{\overline{\mu}}{2}\overline{B}_3^2-\overline{\eta}_5^{(3)}\right)}{\left(\overline{\eta}_4^{(2)}\overline{\eta}_2^{(3)}-\overline{\eta}_4^{(3)}\overline{\eta}_2^{(2)}\right)}\left[\frac{\tanh(k_{\mathrm{w}}l_{\mathrm{g}}r_3/2)}{\tanh(k_{\mathrm{w}}l_{\mathrm{g}}/2)}\right]^{\pm1},
\end{aligned}
\tag{8}
$$

where $\widetilde{h} = (1/\overline{L} - \lambda_3/\lambda_0)L_{\mathrm{g}}$, k_{w} is the positive 'wavenumber', the exponents "±1" identify the antisymmetric and symmetric winkling, respectively, and

$$
r_{2,3} = -\mathrm{i}p_{2,3},\quad \overline{\eta}^{(1)} = \begin{bmatrix} 0\\ 0\\ \mathrm{i}\\ \overline{B}_3\\ \mathrm{i}\overline{B}_3\\ -1 \end{bmatrix}_{p_1=\mathrm{i}},\quad \overline{\eta}^{(2,3)} = \begin{bmatrix} \dfrac{\alpha-\gamma-\beta\lambda_1^2\lambda_3^2+2\overline{B}_3^2-\overline{\tau}_{33}}{(\alpha+\overline{B}_3^2+\overline{\tau}_{11}-\overline{\tau}_{33})/p_{2,3}+(\gamma+\beta\lambda_3^4-2\overline{B}_3^2+\overline{\tau}_{33})p_{2,3}}\\[2ex]
\dfrac{(\alpha+\overline{B}_3^2-\overline{\tau}_{33})(\alpha-\gamma-\beta\lambda_1^2\lambda_3^2+2\overline{B}_3^2-\overline{\tau}_{33})}{(\alpha+\overline{B}_3^2+\overline{\tau}_{11}-\overline{\tau}_{33})/p_{2,3}+(\gamma+\beta\lambda_3^4-2\overline{B}_3^2+\overline{\tau}_{33})p_{2,3}}+\alpha p_{2,3}\\[2ex]
\dfrac{\alpha-\gamma-\beta\lambda_1^2\lambda_3^2+2\overline{B}_3^2-\overline{\tau}_{33}}{\frac{\alpha+\overline{B}_3^2+\overline{\tau}_{11}-\overline{\tau}_{33}}{p_{2,3}^2(\gamma+\beta\lambda_3^4-2\overline{B}_3^2+\overline{\tau}_{33})}+1}-2(\alpha+\overline{B}_3^2-\overline{\tau}_{33})+\gamma+\beta\lambda_1^2\lambda_3^2\\[2ex]
\dfrac{-\overline{B}_3(\alpha-\gamma-\beta\lambda_1^2\lambda_3^2+2\overline{B}_3^2-\overline{\tau}_{33})}{(\alpha+\overline{B}_3^2+\overline{\tau}_{11}-\overline{\tau}_{33})/p_{2,3}+(\gamma+\beta\lambda_3^4-2\overline{B}_3^2+\overline{\tau}_{33})p_{2,3}} \end{bmatrix}_{p_{2,3}},
\tag{9}
$$

$$
p_{2,3} = \mathrm{i}\sqrt{\frac{\left(\overline{B}_3^2-2J^3\overline{W}_{33}-\frac{\overline{\tau}_{33}}{2}\right)\left[(\lambda_1^2+\lambda_3^2)+2(\lambda_1^2-\lambda_3^2)^2\frac{\overline{W}_{11}}{\overline{W}_1}\right]-\frac{\lambda_3\overline{W}_1}{\lambda_1\lambda_2}\left[(\lambda_1^2-\lambda_3^2)+2\lambda_3^2(3\lambda_1^2-\lambda_3^2)\frac{\overline{W}_{11}}{\overline{W}_1}\right]}{2\lambda_3^2\left[\overline{B}_3^2-2J\lambda_3^2\left(\frac{\overline{W}_{11}}{\lambda_1^2\lambda_2^2}+\lambda_1^2\lambda_2^2\overline{W}_{33}\right)-\frac{\overline{\tau}_{33}}{2}\right]}\pm\frac{\sqrt{\left\{\left(\overline{B}_3^2-2J^3\overline{W}_{33}-\frac{\overline{\tau}_{33}}{2}\right)\left[2(\lambda_1-\lambda_3)^2\frac{\overline{W}_{11}}{\overline{W}_1}+1\right]+\frac{\lambda_3\overline{W}_1}{\lambda_1\lambda_2}\left[2\lambda_3(\lambda_3-2\lambda_1)\frac{\overline{W}_{11}}{\overline{W}_1}+1\right]\right\}\left\{\left(\overline{B}_3^2-2J^3\overline{W}_{33}-\frac{\overline{\tau}_{33}}{2}\right)\left[2(\lambda_1+\lambda_3)^2\frac{\overline{W}_{11}}{\overline{W}_1}+1\right]+\frac{\lambda_3\overline{W}_1}{\lambda_1\lambda_2}\left[2\lambda_3(\lambda_3+2\lambda_1)\frac{\overline{W}_{11}}{\overline{W}_1}+1\right]\right\}}}{\frac{2\lambda_3^2}{(\lambda_1+\lambda_3)|\lambda_1-\lambda_3|}\left[\overline{B}_3^2-2J\lambda_3^2\left(\frac{\overline{W}_{11}}{\lambda_1^2\lambda_2^2}+\lambda_1^2\lambda_2^2\overline{W}_{33}\right)-\frac{\overline{\tau}_{33}}{2}\right]}},
\tag{10}
$$

$$
\alpha = \frac{2\lambda_3}{\lambda_1\lambda_2}\overline{W}_1,\ \beta = \frac{4}{J}\overline{W}_{11},\ \gamma = 4J^3\overline{W}_{33},\ \overline{\tau}_{11} = \overline{\tau}_{33} - \overline{B}_3^2 + 2(\lambda_1^2-\lambda_3^2)\overline{W}_1\Big/J,\ \overline{\tau}_{33} = \overline{\mu}\overline{B}_3^2\Big/2.
\tag{11}
$$

Here and below, the following normalization notations have been applied that

$$\overline{W} = \frac{W}{G},\ \overline{W}_m = \frac{\partial \overline{W}}{\partial I_m},\ \overline{W}_{mn} = \frac{\partial^2 \overline{W}}{\partial I_m \partial I_n},\ \overline{B}_3 = \frac{B_3}{\sqrt{G\mu_g}}, \tag{12}$$

where $m, n = 1,\ 3$, and G tentatively refers to the initial shear modulus of the MAH block.

4. Discussions for generalized neo-Hookean and Gent ideal MAH blocks

We now restrict our attention to specific constrained swelling MAH blocks subjected to a certain magnetic biasing field, as illustrated in Fig. 2(b). Following previously published works (Hong et al., 2009; Wu and Destrade, 2021; Xia et al., 2025), we consider the gel with following neo-Hookean and Gent ideal magnetoelastic energy function

$$\begin{aligned} &W(\boldsymbol{F}, \boldsymbol{B}_l) = W_{\mathrm{nH(G)}}(I_1, I_3) - \frac{\Phi_c}{\varpi}\left(\sqrt{I_3} - 1\right) + \frac{I_5}{2\mu_g\sqrt{I_3}} - \frac{kT}{\varpi}\left[\left(\sqrt{I_3} - 1\right)\ln\left(1 + \frac{1}{\sqrt{I_3} - 1}\right) + \frac{\chi}{\sqrt{I_3}}\right], \\ &W_{\mathrm{nH}}(I_1, I_3) = \frac{NkT}{2}(I_1 - 3 - \ln I_3),\ W_{\mathrm{G}}(I_1, I_3) = \frac{NkT}{2}\left(J_{\mathrm{m}}\ln\left(1 - \frac{I_1 - 3}{J_{\mathrm{m}}}\right) - \ln I_3\right). \end{aligned} \tag{13}$$

Here, N is the number of polymer chains per unit volume of the dry network, T and k are the temperature and the Boltzmann constant, respectively, ϖ is the volume per solvent molecule, χ is a nondimensional parameter characterizing the enthalpy of mixing, and J_{m} is the chain extension limit of the polymer network. In this case, the explicit expressions of the coefficients in Eq. (11) are given by

$$\begin{aligned} &\overline{a}_1 = \frac{\lambda_3^2}{J},\ \overline{a}_2 = \frac{\lambda_3^2 + \zeta}{J},\ \overline{a}_3 = \frac{\psi}{J} - \frac{\overline{B}_3^2}{2},\ \overline{a}_4 = \frac{\lambda_3^2}{J} + \overline{B}_3^2,\ \overline{a}_5 = \frac{\lambda_1^2 + \zeta}{J} + \overline{B}_3^2,\ \overline{b}_1 = -\overline{B}_3,\ \overline{c}_1 = \overline{B}_3,\ \overline{c}_2 = -\overline{B}_3,\ \overline{d}_1 = 1, \\ &\overline{\tau}_{33} = \frac{\overline{\mu}}{2}\overline{B}_3^2,\ \overline{\tau}_{11} = \frac{\lambda_1^2 - \lambda_3^2}{J} + \overline{B}_3^2\left(\frac{\overline{\mu}}{2} - 1\right), \end{aligned} \tag{14}$$

with

$$\zeta = \frac{1}{N\varpi}\left(\frac{1}{J-1} - \frac{2\chi}{J}\right) + 1,\ \psi = \frac{J}{N\varpi}\left[\ln\left(1 - \frac{1}{J}\right) + \frac{1}{J-1} - \frac{\chi}{J^2} - \frac{\Phi_c}{kT}\right], \tag{15}$$

where the initial shear modulus G has been replaced by NkT according to the specific energy density function (13).

4.1. Nonlinear response

The true magnetic induction field $\boldsymbol{B}$ is obtained from Eq. (4) using the energy function (13). The non-zero component and its Lagrangian counterpart have the following nondimensional forms:

$$\overline{B}_3 = \frac{\overline{I}}{(1-\overline{\mu})\overline{L}\lambda_3/\lambda_0 + \overline{\mu}},\ \overline{H}_0 = \frac{\overline{I}}{(1-\overline{\mu})\overline{L}/\lambda_0 + \overline{\mu}/\lambda_3}, \tag{16}$$

where $\overline{I} = i_0\sqrt{\mu_g/NkT}$ is the nondimensional free current density, and $\overline{L} = L_g/L_t$ is the non-dimensional initial block thickness.

For the concerned Gent gel described by Eq. (13), the in-plane nominal stress components s_1 and s_2 can be derived from Eqs. (6) and (7) in following non-dimensional forms:

$$\overline{s}_1 = \lambda_0^{-2}\left[\frac{J_{\mathrm{m}}}{3 - I_1 + J_{\mathrm{m}}}\lambda_1 - \frac{\lambda_3^2}{\lambda_1} + \lambda_2\lambda_3(\overline{\mu} - 1)\overline{B}_3^2\right],\ \overline{s}_2 = \lambda_0^{-2}\left[\frac{J_{\mathrm{m}}}{3 - I_1 + J_{\mathrm{m}}}\lambda_2 - \frac{\lambda_3^2}{\lambda_2} + \lambda_1\lambda_3(\overline{\mu} - 1)\overline{B}_3^2\right], \tag{17}$$

where $\overline{s}_i = \overline{s}_i/(NkT)$ and the out-of-plane stretch λ_3 is determined by

$$\frac{J_{\mathrm{m}}}{3 - I_1 + J_{\mathrm{m}}}\lambda_3^2 - (\zeta - \psi) + \frac{J}{2}(1 - \overline{\mu})\overline{B}_3^2 = 0. \tag{18}$$

By combining Eqs. (16) and (17), the relationship between the applied biasing field and the nonlinear response of the immersed MAH block can be expressed as

$$\frac{\overline{I}}{(1-\overline{\mu})\overline{L}\lambda_3/\lambda_0 + \overline{\mu}} = \sqrt{\frac{\lambda_1\lambda_0^2\overline{s}_1 - \dfrac{J_{\mathrm{m}}}{3 - I_1 + J_{\mathrm{m}}}\lambda_1^2 - \lambda_3^2}{J(\overline{\mu} - 1)}} = \sqrt{\frac{\lambda_2\lambda_0^2\overline{s}_2 - \dfrac{J_{\mathrm{m}}}{3 - I_1 + J_{\mathrm{m}}}\lambda_2^2 - \lambda_3^2}{J(\overline{\mu} - 1)}}. \tag{19}$$

A pull-in instability may occur when the nonlinear $\overline{I}$-$\lambda_{1(2)}$ relationship in Eq. (19) reaches a local maximum, i.e., $\mathrm{d}\overline{I}/\mathrm{d}\lambda_{1(2)} = 0$. Without loss of generality, considering the equi-biaxial case with $\lambda_1 = \lambda_2$ and $\overline{s}_1 = \overline{s}_2 = \overline{s}$, Eqs. (19) and (17) reduce to

$$\bar{I} = [(1-\bar{\mu})\bar{L}\lambda_3/\lambda_0 + \bar{\mu}]\sqrt{\frac{\bar{s}\lambda_0^2\Big/\lambda_1 - \dfrac{J_{\rm m}}{3-I_1+J_{\rm m}}1-\lambda_3^2\Big/\lambda_1^2}{\lambda_3(\bar{\mu}-1)}}, \tag{20}$$

with the nonlinear response given by

$$\bar{s} = \frac{\lambda_1}{\lambda_0^2}\left[\frac{J_{\rm m}}{3-I_1+J_{\rm m}}\left(1-\frac{\lambda_3^2}{\lambda_1^2}\right) + \lambda_3(\bar{\mu}-1)\bar{B}_3^2\right]. \tag{21}$$

The free swelling ratio λ_0 of the magnetic-driven block is obtained by combining Eqs. (16) and (20) for $\bar{s}=0$ under no magnetic field ($\bar{B}_3=0$). By taking the extension limit $J_{\rm m}\to\infty$, the expressions for the neo-Hookean case can be easily derived, as the Gent model reduces to the neo-Hookean model in this limit.

Combining Eqs. (16) and (20), we first plot the nonlinear responses of equi-biaxially deformed neo-Hookean and Gent ($J_{\rm m}=97.2$) ideal MAH blocks immersed in a solvent with different chemical potentials. The normalized permeability is set to $\bar{\mu}=0.1$, as shown in Fig. 3. We consider the normalized in-plane normal stress $\bar{s}=0,\ \pm 1$ and the relative thickness $\bar{L}=0.3,\ 0.8$ as examples. Typically, the response curve of a neo-Hookean material rises initially and then falls (Su et al., 2019). However, for the problem under consideration, we observe an N-shaped response curve, which is characteristic of strain-stiffening materials such as the Gent material (Su et al., 2018). This suggests that the presence of top and bottom walls of the tank induces a Gent-like deformation behavior in the neo-Hookean ideal MAH block when $\bar{\mu}<1$. The onset of pull-in instability, as determined by the *Hessian criterion* (Zhao and Suo, 2007), is then observed in Fig. 3(a, b) for both $\Phi_{\rm c}/kT=0,\ -0.01$ (see orange curves). This behavior is essentially similar to that shown in Fig. 3(c, d) for the Gent case. Interestingly, such phenomenon uniformly disappears as $\bar{\mu}$ increases to 0.6, even in the Gent case, as illustrated in Fig. C1. It is important to note that the out-of-plane stretch λ_3 is constrained by the top and bottom walls.

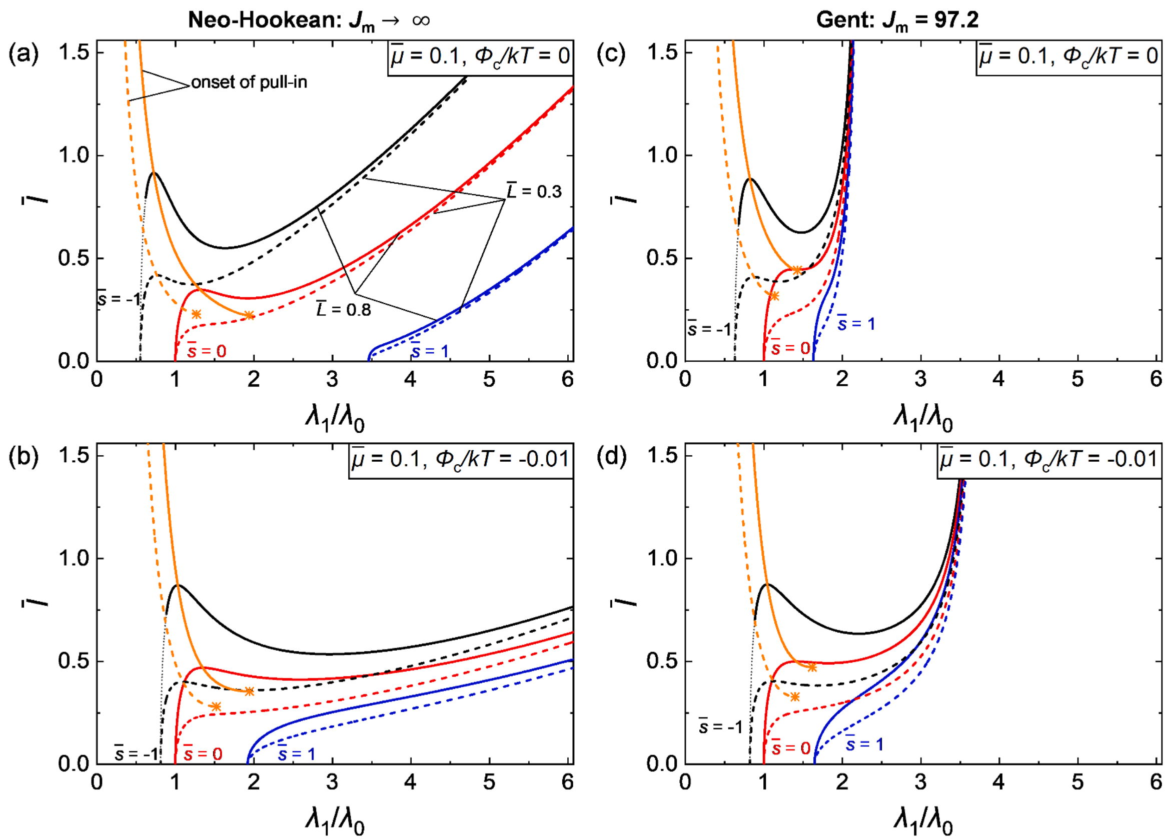

Fig. 3. Nonlinear responses of ideal MAH blocks immersed in a solvent with different chemical potentials are analyzed for the normalized permeability $\bar{\mu}=0.1$. The responses are plotted for $\bar{L}=0.8$ (solid curves) and $\bar{L}=0.3$ (dash curves), respectively. (a) $\Phi_{\rm c}/kT=0$ and (b) $\Phi_{\rm c}/kT=-0.01$ for the neo-Hookean case; (c) $\Phi_{\rm c}/kT=0$ and (d) $\Phi_{\rm c}/kT=-0.01$ for the Gent ($J_{\rm m}=97.2$) case. The normalized in-plane normal stress $\bar{s}=0,\ \pm 1$ correspond to the black, red, and blue curves, respectively. The dotted curves are excluded from the nonlinear responses due to the geometric constraint imposed by the tank ($\lambda_3\le\lambda_0/\bar{L}$). These panels demonstrate the occurrence of pull-in instability, which corresponds to the critical peaks ($\mathrm{d}\bar{I}/\mathrm{d}\lambda_1=0$) of the loading curves.

Therefore, the dotted parts of curves are excluded due to the geometric constraint ($\lambda_3 \le \lambda_0/\overline{L}$). This constraint must always be followed throughout the present discussion.

To further clarify the 'magneto-geometry' coupled pull-in instability, we plot the effect of normalized permeability on the onset of pull-in for ideal MAH blocks immersed in a solvent, as shown in Fig. 4. Taking $\overline{L} = 0.8$ as an example, Fig. 4(a, c) depict the contours of critical current for the neo-Hookean and Gent ($J_m = 97.2$) cases, respectively. These contours monotonically decrease with increasing in-plane normal stress. Notably, only in the neo-Hookean case does the critical bound for the onset of pull-in exhibit a non-monotonic character when the chemical potential difference between the block and the solvent vanishes, i.e., $\Phi_c/kT = 0$. Specifically, the corresponding cut-off permeability initially decreases as the in-plane normal stress increases to $\bar{s} =\sim 1.589$ and then conversely rises with the further increases in stress. Although the increase in cut-off permeability is relatively smooth, the green extreme point $(0.01005,\ 1.58897)$ in Fig. 4(a) indicates that the onset of pull-in becomes inevitable for MAH blocks with a normalized permeability small than ~ 0.010. However, this phenomenon is not observed in the case of $\Phi_c/kT = -0.01$ as shown in Fig. C2(a), nor in the Gent case of $\Phi_c/kT = 0,\ -0.01$, as seen in Figs. 4(b) and C2(b). This suggests that a negative chemical potential and a reduced extension limit may help suppress the onset of pull-in instability. On the other hand, the occurrence and vanishing of pull-in, as shown in Figs. 3 and C1, can be easily examined by the relative locations of the critical bounds of pull-in for $\overline{L} = 0.3,\ 0.8$ and $\Phi_c/kT = 0, -0.01$ and six representative cases. These cases are marked by star points (A-F) with $\overline{\mu} = 0.1,\ 0.6$ and $\bar{s} = \pm 1,\ 0$, as depicted in Fig. 4(b, d) for the neo-Hookean and the Gent cases, respectively.

We now examine the dependence of the in-plane stretch λ_1/λ_0 on the normalized electric current $\overline{I}$ for immersed neo-Hookean and Gent ideal MAH blocks with relative permeability $\overline{\mu} = 1.5$ and relative thickness $\overline{L} = 0.3,\ 0.8$, subject to in-plane normal stress $\bar{s} = \pm 1,\ 0$, as shown in Fig. 5. Unlike the cases depicted in Fig. 3 for $\overline{\mu} < 1$, the application of a current-induced magnetic field results in a decrease in λ_1 with varying $\overline{I}$, i.e., *lateral contraction*, a phenomenon similarly reported for incompressible soft dielectric plates (Su et al., 2020). Concurrently, as the out-of-plane stretch λ_3 increases, the block may experience push-out instability, characterized by a sudden increase in thickness when the current reaches a critical point at $\mathrm{d}\overline{I}/\mathrm{d}\lambda_1 = 0$. However, due to the geometric constraint of the tank, λ_3 cannot increase beyond the upper threshold $\lambda_0/\overline{L}$. No pull-out phenomena are observed except for the case of $(\overline{\mu},\ \bar{s}, \Phi_c/kT) = (2,\ 1,\ -0.01)$, as illustrated by the blue solid curves in Fig. C3(b, d). This suggests that, through careful structural and material design, it is possible to trigger the pull-out instability in the material before it reaches the edge of the tank.

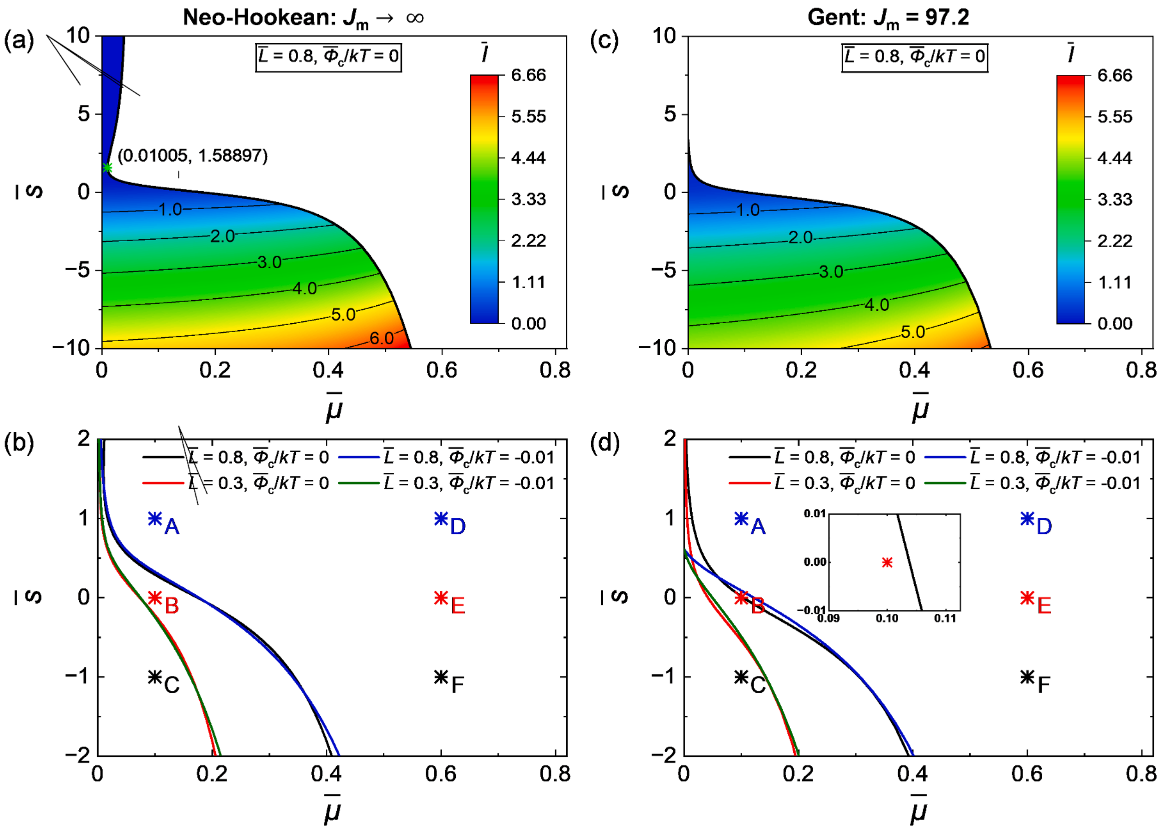

Fig. 4. Effect of normalized permeability on the pull-in instability of neo-Hookean and Gent ($J_m = 97.2$) ideal MAH blocks ($\overline{\mu} < 1$) immersed in a solvent. (a) and (c) Contours of critical current for $\overline{L} = 0.8$ and $\Phi_c/kT = 0$; (b) and (d) Critical bounds for $\overline{L} = 0.3,\ 0.8$ and $\Phi_c/kT = 0,\ -0.01$, respectively. The star points (A-F) represent complete cases composed of $\overline{\mu} = 0.1,\ 0.6$ and $\bar{s} = \pm 1,\ 0$.

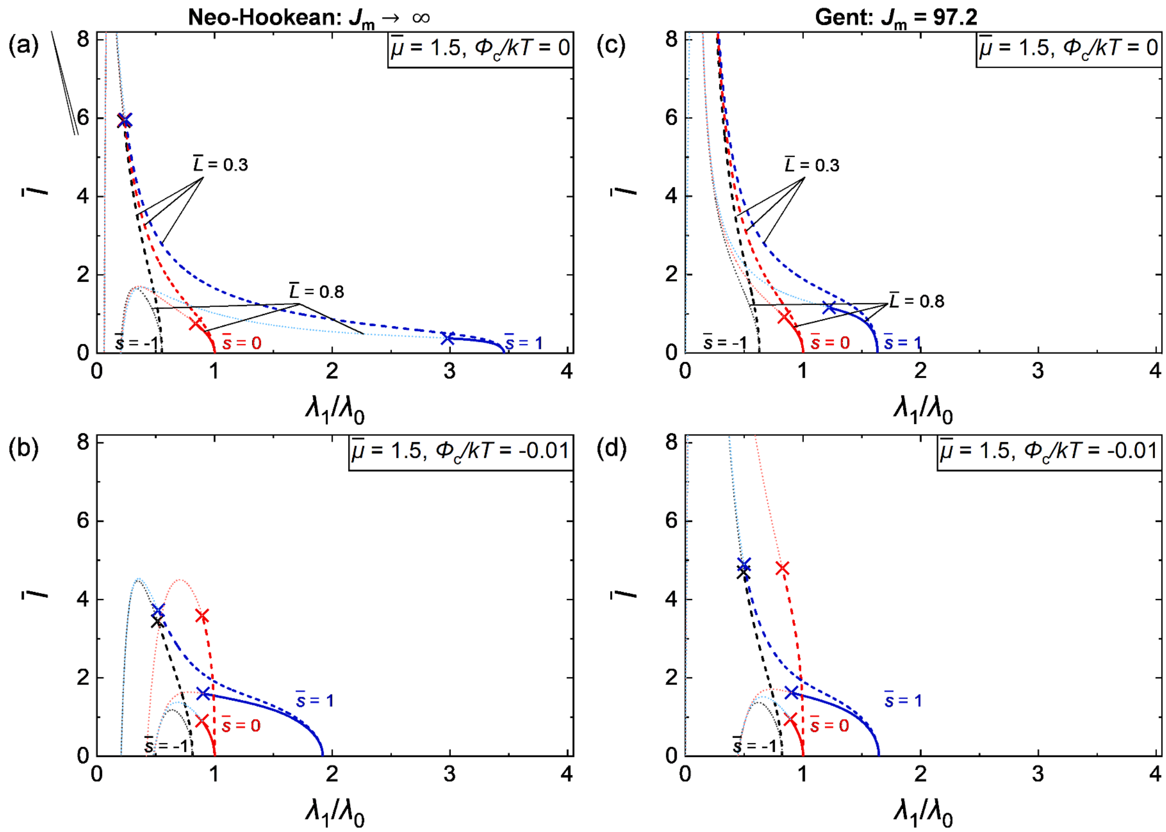

Fig. 5. Nonlinear responses of ideal MAH blocks immersed in a solvent with different chemical potentials are analyzed for the normalized permeability $\bar{\mu} = 1.5$. The responses are plotted for $\bar{L} = 0.8$ (solid curves) and $\bar{L} = 0.3$ (dash curves), respectively. (a) $\Phi_c/kT = 0$ and (b) $\Phi_c/kT = -0.01$ for the neo-Hookean case; (c) $\Phi_c/kT = 0$ and (d) $\Phi_c/kT = -0.01$ for the Gent ($J_m = 97.2$) case. The normalized in-plane normal stress $\bar{s} = -1,\ 0,\ 1$ correspond to the black, red, and blue curves, respectively. The dotted curves are excluded from the nonlinear responses due to the geometric constraint of the tank ($\lambda_3/\lambda_0 \le 1/\bar{L}$).

4.2. Bifurcation analysis

To ensure robustness and convenience in numerical computation, we specialize to the generalized ideal magnetoelastic model with decoupled variants I_1 and I_3 (i.e., $\overline{W}_{13} = 0$). In Section 3, explicit and compact bifurcation equations for wrinkling onset have been established, replacing the cumbersome general formulae (B20) derived based on the earlier work (Xia, 2024). Specifically, for the neo-Hookean case, given

$$\overline{W}_1 = \frac{1}{2},\ \overline{W}_{11} = 0,\ \overline{W}_{33} = \frac{3\overline{B}_3^2/2 + (2\zeta - \psi)/J}{4J^3}, \tag{22}$$

the explicit form of wrinkling criterion for the immersed block can be reduced from Eq. (8) as follows

$$\frac{(r_2^2+1)^2}{(r_2^2-1)r_2r_3}\left[\frac{\tanh(\pi r_3\lambda_3 L_g/\mathscr{L})}{\tanh(\pi\lambda_3 L_g/\mathscr{L})}\right]^{\pm1} - \frac{4}{(r_2^2-1)}\left[\frac{\tanh(\pi\lambda_1 L_g/\mathscr{L})}{\tanh(\pi\lambda_3 L_g/\mathscr{L})}\right]^{\pm1} = \frac{\lambda_2\overline{B}_3^2(1-\bar{\mu})^2}{1+\bar{\mu}\tanh\left[\pi\left(\frac{1}{\bar{L}}-\frac{\lambda_3}{\lambda_0}\right)\frac{L_g}{\mathscr{L}}\right]\tanh^{\pm1}(\pi\lambda_3 L_g/\mathscr{L})}, \tag{23}$$

where $r_2 = \lambda_1/\lambda_3$ and $r_3 = \sqrt{1-(\lambda_1^2-\lambda_3^2)/[(1-\bar{\mu})J\overline{B}_3^2/2+\psi-2\zeta]}$, with $\mathscr{L} = 2\pi/k_w$ being the "wavelength" of wrinkles. Note that, when the magnetic biasing field is removed, the bifurcation relation (23) recovers the purely elastic case as (Ogden and Roxburgh, 1993; Weiss et al., 2013)

$$\frac{(r_2^2+1)^2}{4r_2r_{30}} = \left[\frac{\tanh(\pi\lambda_1 L_g/\mathscr{L})}{\tanh(\pi r_3\lambda_3 L_g/\mathscr{L})}\right]^{\pm1},\ r_{30} = \sqrt{\frac{\lambda_1^2+\zeta}{\lambda_3^2+\zeta}}. \tag{24}$$

Using the first expression in Eq. (16), the bifurcation equation can be expressed as

$$\frac{\bar{I}}{(1-\bar{\mu})\bar{L}\lambda_3/\lambda_0+\bar{\mu}} = \sqrt{\frac{\bar{\mu}\tanh\left[\pi\left(\frac{1}{\bar{L}}-\frac{\lambda_3}{\lambda_0}\right)\frac{L_g}{\mathscr{L}}\right]+\coth^{\pm1}\left(\pi\lambda_3\frac{L_g}{\mathscr{L}}\right)}{\lambda_2(r_2^2-1)(1-\bar{\mu})^2}}\sqrt{\frac{(r_2^2+1)^2\tanh^{\pm1}\left(r_3\pi\lambda_3\frac{L_g}{\mathscr{L}}\right)}{r_2r_3}-4\tanh^{\pm1}\left(\pi\lambda_1\frac{L_g}{\mathscr{L}}\right)}. \tag{25}$$

The anti-symmetric thin- and thick-plate limits are then obtained by evaluating Eq. (25) for $L_g/\mathscr{L}\to0$ and $L_g/\mathscr{L}\to\infty$, respectively, as

$$\frac{\bar{I}}{(1-\bar{\mu})\bar{L}/\lambda_0+\bar{\mu}/\lambda_3} = \sqrt{\frac{\lambda_3(\lambda_1^2-\lambda_3^2)}{\lambda_1\lambda_2(\bar{\mu}-1)^2}}, \tag{26}$$

and

$$\frac{\bar{I}}{(1-\bar{\mu})\bar{L}/\lambda_0+\bar{\mu}/\lambda_3} = \begin{cases} \lambda_3\sqrt{\dfrac{1}{\lambda_2(\bar{\mu}-1)^2(r_2^2-1)}\left[\dfrac{(r_2^2+1)^2}{r_2r_3}-4\right]}, & \lambda_3=\lambda_0/\bar{L}, \\ \lambda_3\sqrt{\dfrac{(\bar{\mu}+1)}{\lambda_2(\bar{\mu}-1)^2(r_2^2-1)}\left[\dfrac{(r_2^2+1)^2}{r_2r_3}-4\right]}, & \lambda_3<\lambda_0/\bar{L}. \end{cases} \tag{27}$$

Note that the case of $\lambda_3>\lambda_0/\bar{L}$ is excluded automatically to satisfy the geometric constraint.

Recalling the nonlinear response $(19)_1$ with $\bar{s}_1=0$, $J_m\to\infty$, and $\bar{\mu}<1$, we find that the loading curve $\bar{I}$-λ_1 under no in-plane stress can be used to represent the thin-plate limit of winkling (26) by scaling the current $\bar{I}$ with a factor of $1/\sqrt{1-\bar{\mu}}$. These two cases become equivalent only when the effect of external field vanishes ($\bar{\mu}=0$). Additionally, the bifurcation relation for the short-wave limit takes the form of a piecewise function, which depends on the characteristic out-of-plane stretch $\lambda_0/\bar{L}$.

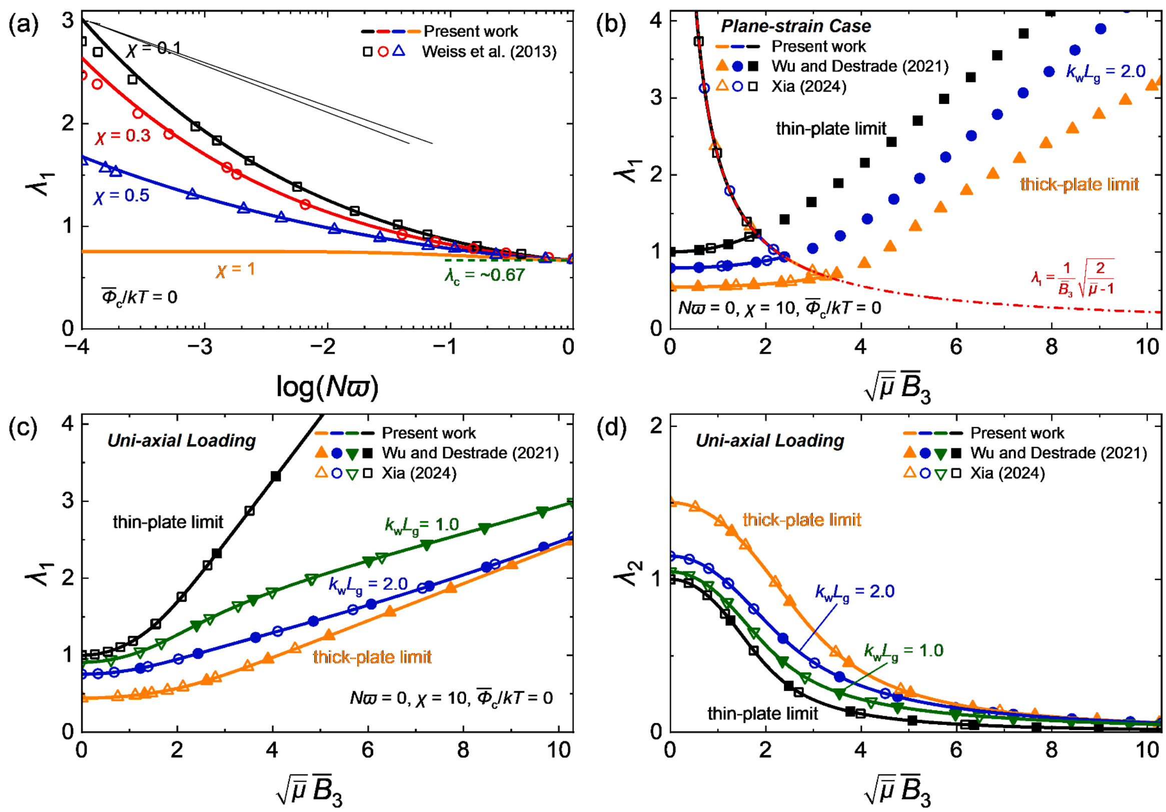

Fig. 6. Quantitative comparisons between present work and existing results are summarized as follows. (a) Critical stretch for the onset of wrinkles on the surface of a swollen hydrogel ($\chi=0.1\to0.3\to0.5\to1$) with varying $N\varpi$ (Weiss et al., 2013); (b) Critical stretch for the onset of wrinkles on a reduced neo-Hookean ideal MAH block and a perfectly incompressible magnetoelastic soft plate under plane-strain conditions with the in-plane stretch $\lambda_2=1$ and the out-of-plane stretch λ_3 adjusting accordingly; (c, d) Critical stretch for the onset of wrinkles under uni-axial loading with the external Maxwell stress (Wu and Destrade, 2021; Xia, 2024).

4.2.1. Comparison with existing results

To validate the present theory, we first revisit the surface wrinkling of a swollen hydrogel under an equal-biaxial pre-stretch (Weiss et al., 2013). Using the reduced bifurcation Eq. (24) with $L_g/\mathscr{L}\to\infty$, we reproduce the critical pre-stretch for the onset of wrinkles on the surface of the swollen gel, as shown in Fig. 6(a). For three values of χ (0.1, 0.3, 0.5), our results agree well with those obtained by Weiss et al. (2013), with neglectable differences observed for very small $N\varpi$ ($\sim 10^{-4}$). As the nondimensional χ increases from 0.1 to 1, the critical curves flatten with varying $N\varpi$, uniformly approaching the classical critical stretch for incompressible rubber under equi-biaxial compression ($\lambda_c = \sim 0.67$) (Biot, 1963). This suggests that, when the polymer network is highly crosslinked, the gel behaves like an incompressible elastomer/rubber.

To further validate our theory, we compare it with existing predictions for nearly/perfectly incompressible magnetoelastic soft plates (Wu and Destrade, 2021; Xia, 2024). Without loss of generality, we assign the MAH block the following parameters: $N\varpi = 1, \chi = 10$, and $\Phi_c/kT = 0$. The normalized permeability is set to $\overline{\mu} = 5/3$ to align with the existing works mentioned above. The critical stretch for onset of wrinkling under a magnetic biasing field is illustrated in Fig. 6 (b-d) for cases with the plane-strain constraint and uniaxial loading, respectively. As seen from the critical curves for the thin-plate limit ($k_w L_g = 0$), $k_w L_g = 1$ and/or 2, and short-wave limit ($k_w L_g \to \infty$), the predictions of present theory for a highly crosslinked hydrogel closely reproduce those previously reported for the wrinkling of nearly/perfectly incompressible magnetoelastic soft plates. This includes the differences induced by the constraint of deformation for resisting the external Maxwell stress ($\lambda_3 > \overline{B}_3\sqrt{(\overline{\mu}-1)/2}$).

4.2.2. Thin-plate and short-wave instabilities

We now consider the case of $\overline{L} = 0.8$ to examine the wrinkling behavior of equi-biaxially stretched ($\lambda_1 = \lambda_2$) neo-Hookean and Gent ideal MAH blocks immersed in a solvent with varying chemical potentials and a normalized permeability $\overline{\mu} = 0.1$, as shown in Fig. 8. The critical curves for the thin-plate limit ($L_g/\mathscr{L}\to 0$), $L_g/\mathscr{L} = 0.2$, and the thick-plate limit ($L_g/\mathscr{L}\to\infty$) are depicted by black, blue, and red lines, respectively. Only the solid parts of these curves are physically feasible due to the geometric constraint of the tank. The nonlinear responses of the block for $\overline{s} = 0$, depicted by gray lines, are reproduced from Fig. 3 to calibrate the initial reference state. As clearly seen in Fig. 8, the curves for the thin-plate limit are consistently positioned above those for $\overline{s} = 0$. This behavior is expected

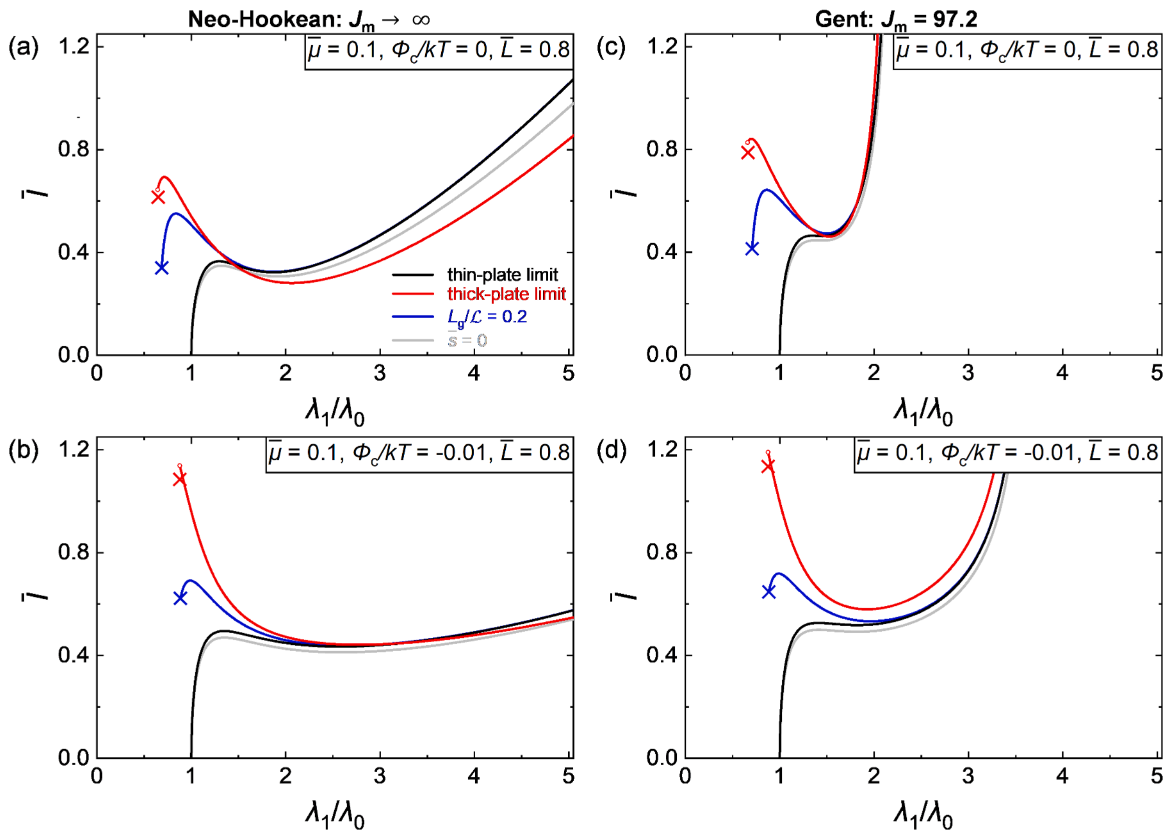

Fig. 7. The wrinkling behavior of ideal MAH blocks immersed in a solvent with varying chemical potentials is analyzed for a normalized permeability $\overline{\mu} = 0.1$ and a relative thickness $\overline{L} = 0.8$. (a) $\Phi_c/kT = 0$ and (b) $\Phi_c/kT = -0.01$ for the neo-Hookean case; (c) $\Phi_c/kT = 0$ and (d) $\Phi_c/kT = -0.01$ for the Gent ($J_m = 97.2$) case. The critical curves of $\overline{I}$ versus λ_1/λ_0 for the thin-plate limit, $L_g/\mathscr{L} = 0.2$, and the thick-plate limit, and the nonlinear response for $\overline{s} = 0$ are depicted by black, blue, red, and gray lines, respectively. All curves satisfy the geometric constraint of the tank ($\lambda_3 \le \lambda_0/\overline{L}$), with the case of $\lambda_3 = \lambda_0/\overline{L}$ marked by crosses.

because the scaling factor $1/\sqrt{1-\overline{\mu}}$ is always greater than 1. This suggests that wrinkling in an infinitely thin block must be induced by an in-plane compression ($\overline{s} < 0$). The critical compression required for the wrinkling in contraction decreases as $L_g/\mathscr{L}$ increases to 0.2, indicating a significant stabilizing effect with increasing thickness. However, this effect diminishes progressively as the normalized critical stretch λ_1/λ_0 increases. This is evidenced by the gradual convergence of the critical curves for $L_g/\mathscr{L} = 0.2$ toward those for the thin-plate limit Fig 7.

As seen in Fig. 8(a) for $\overline{\mu} = 0.1$ and $\Phi_c/kT = 0$, the critical curve for the thick-plate limit drops below that corresponding to $\overline{s} = 0$ when the critical stretch increases to a certain value. This implies that increasing thickness can eventually induce wrinkling of the block in extension. When compared with the observations from Figs. 8(b, c, d) and C4, wrinkling in extension may be suppressed by either increasing the normalized permeability $\overline{\mu}$, or decreasing the chemical potential Φ_c/kT and the extension limit J_m. Moreover, it is quite interesting to note that the magnitude of "mutation" at $\lambda_3 = \lambda_0/\overline{L}$, which has been explicitly predicted in Eq. (27), could be enhanced with the increasing $\overline{\mu}$, as seen in Fig. C4 for $\overline{\mu} = 0.6$. As a result, the critical curves for the thick-plate limit are entirely located above those for the thin-plate limit. This suggests that the surface wrinkling of the immersed block with $\overline{\mu} = 0.6$ always occurs at the thin-plate limit. The parallel results observed in Figs. 8 and C5 for $\overline{L} = 0.3$ exhibit essentially identical behavior to that shown in Figs. 8 and C4. The most notable distinction between them is that the critical curves are not influenced by the geometric constraint as the upper threshold value of the out-of-plane stretch increases from $1.25\lambda_0$ for $\overline{L} = 0.8$ to $\sim 3.33\lambda_0$ for $\overline{L} = 0.3$.

We now examine the wrinkling behave or of the similar immersed MAH blocks but with a normalized permeability of $\overline{\mu} = 1.5$, as shown in Fig. 9. The same critical situations and the initial state of $\overline{s} = 0$ as presented in Fig. 8 are applied here for easier comparison. The response curves for $\overline{s} = 0$ show that the magnetic biasing field generated by $\overline{I}$ induces an expansion in thickness ($\lambda_3\uparrow$) and a reduction in equi-biaxial in-plane stretch ($\lambda_1 = \lambda_2\downarrow$). Unlike the results shown in Fig. 8, these response curves exhibit a tendency opposite to the critical curves for the thin-plate limit, indicating the occurrence of wrinkling in extension for the thin blocks with $\overline{\mu} > 1$. Considering the exclusion of dotted parts for $\lambda_3 > \lambda_0/\overline{L}$, we observe that wrinkling in the blocks may occur with either an expansion in thickness, as shown in Fig. 9(a, c) for $\Phi_c/kT = 0$, or a reduction in thickness, as shown in Fig. 9(b, d) for $\Phi_c/kT = -0.01$. This reveals a possible competition mechanism between the effect of tensile external Maxwell stress applied on the thin blocks and the effect of the negative chemical potential on the critical in-plane stretch. The same mechanism remains valid for cases of $L_g/\mathscr{L} = 0.2$, as

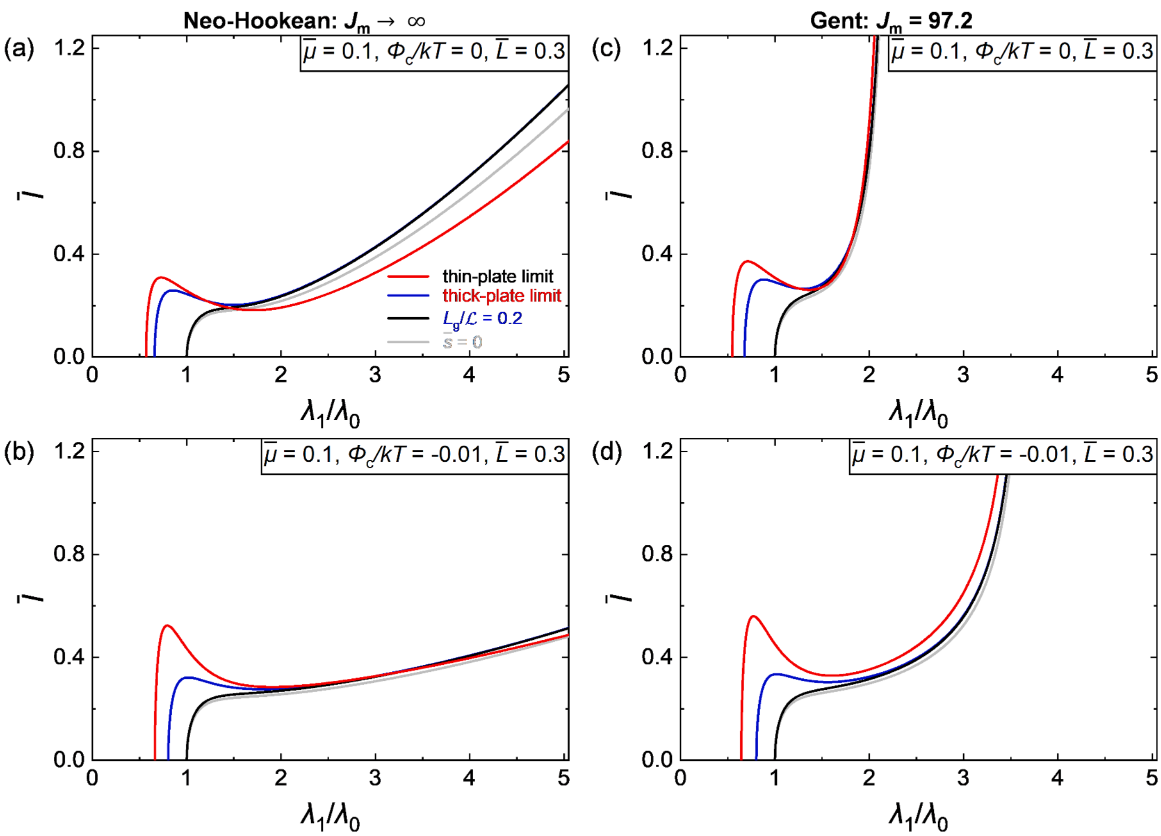

Fig. 8. The wrinkling behavior of ideal MAH blocks immersed in a solvent with varying chemical potentials is analyzed for a normalized permeability $\overline{\mu} = 0.1$ and a relative thickness $\overline{L} = 0.3$. (a) $\Phi_c/kT = 0$ and (b) $\Phi_c/kT = -0.01$ for the neo-Hookean case; (c) $\Phi_c/kT = 0$ and (d) $\Phi_c/kT = -0.01$ for the Gent ($J_m = 97.2$) case. The critical curves of $\overline{I}$ versus λ_1/λ_0 for the thin-plate limit, $L_g/\mathscr{L} = 0.2$, and the thick-plate limit, and the nonlinear response for $\overline{s} = 0$ are depicted by black, blue, red, and gray lines, respectively.

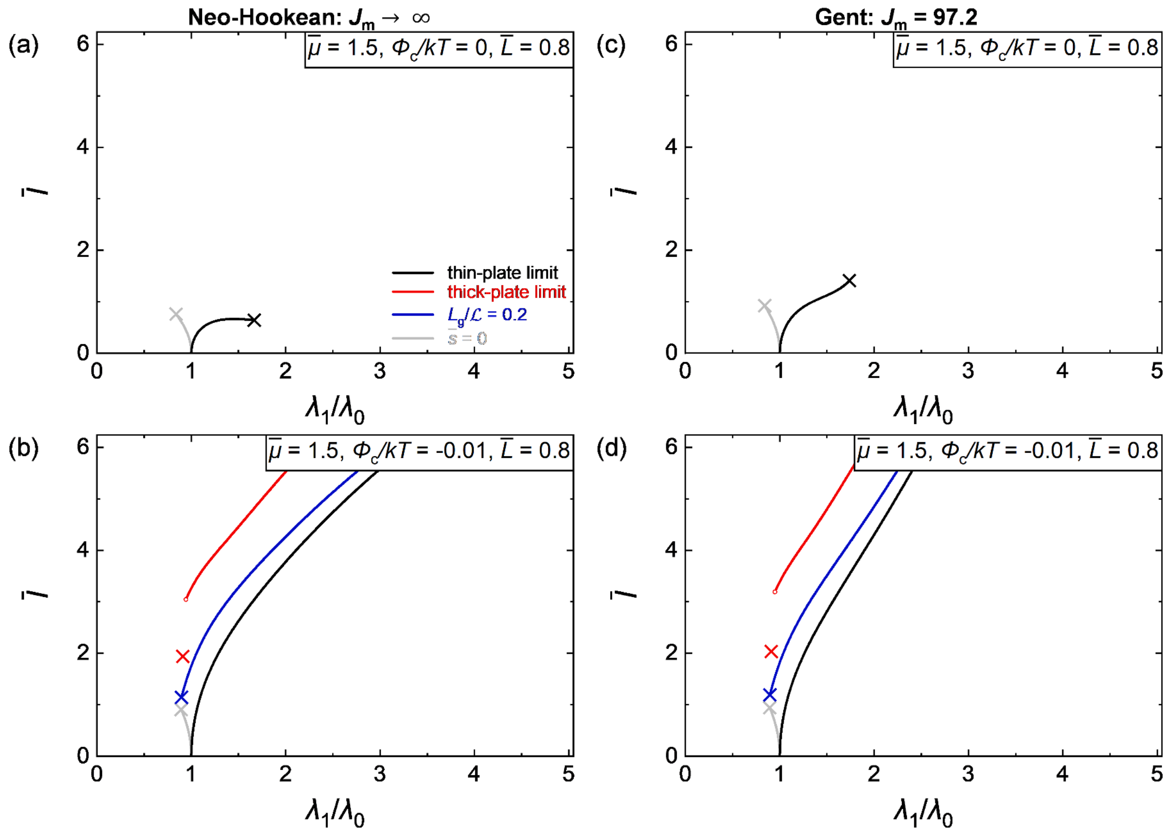

Fig. 9. The wrinkling behavior of ideal MAH blocks immersed in a solvent with varying chemical potentials is analyzed for a normalized permeability $\bar{\mu} = 1.5$ and a relative thickness $\bar{L} = 0.8$. (a) $\Phi_c/kT = 0$ and (b) $\Phi_c/kT = -0.01$ for the neo-Hookean case; (c) $\Phi_c/kT = 0$ and (d) $\Phi_c/kT = -0.01$ for the Gent ($J_m = 97.2$) case. The critical curves of $\bar{I}$ versus λ_1/λ_0 for the thin-plate limit, $L_g/\mathscr{L} = 0.2$, and the thick-plate limit, and the nonlinear response for $\bar{s} = 0$ are depicted by black, blue, red, and gray lines, respectively. All curves satisfy the geometric constraint of the tank ($\lambda_3 \le \lambda_0/\bar{L}$), with the case of $\lambda_3 = \lambda_0/\bar{L}$ marked by crosses.

demonstrated by the comparable evolution of the blue curves with increasing λ_1/λ_0 in Figs. C6(a, c) and C6(b, d). As observed in Figs. 9 (b, d) and C6(a-d), the critical curves for $L_g/\mathscr{L} = 0.2$ consistently initiate on the left-hand side of the response curves for $\bar{s} = 0$, indicating that wrinkling occurs during in-plane contraction. However, since the critical out-of-plane stretch exceeds $\lambda_0/\bar{L}$, the critical points near the initiation region are excluded and cut off by the crosses. When the critical curves shift to the right-hand side of the response curves, no convergence is observed toward the critical curves for the thin-plate limit with wrinkling emerging during in-plane extension.

As depicted in Figs. 9(a, c) and C6(a, c), the critical curves for the thick-plate limit are entirely excluded since the critical λ_3 is always greater than $\lambda_0/\bar{L}$ for the MAH blocks with $\bar{L} = 0.8$. In contrast, as seen in Fig. 10 for the parallel results with $\bar{L} = 0.3$, wrinkling occurs during both in-plane contraction and extension for the neo-Hookean case with $\Phi_c/kT = 0$, as shown by the solid red curves in Figs. 10(a) and C7(a). However, wrinkling is observed only during in-plane contraction in the Gent case with $\Phi_c/kT = 0$ as shown by the corresponding solid red curves in Figs. 10(c) and C7(c), and in both cases with $\Phi_c/kT = -0.01$, as shown in Figs. 10(b, d) and C7 (b, d). These observations suggest that the wrinkling behavior of the immersed MAH blocks is significantly influenced by the relative thickness $\bar{L}$, the normalized permeability $\bar{\mu}$, the extension limit J_m, and the chemical potential Φ_c/kT.

4.2.3. Critical curves for wrinkling under a certain magnetic field

We then further examine the specific wrinkling behaviors of the immersed MAH blocks under a given current. Figs. 11 and 12 show the critical curves of the normalized in-plane stretch λ_1/λ_0 versus the ratio of L_g to $\mathscr{L}$ for the equi-biaxially constrained neo-Hookean and Gent ideal MAH blocks immersed in the solvent, with the normalized permeabilities $\bar{\mu} = 0.1,\ 0.6,\ 1.0$ and $\bar{\mu} = 1,\ 1.5,\ 2.0$, respectively. The chemical potential between the block and the solvent is set as $\Phi_c/kT = 0$ for illustration. The blocks are subjected to sequential current $\bar{I} = 0.1$, 0.35, and 0.6. Since antisymmetric wrinkling typically occurs first, symmetric wrinkling is omitted for conciseness. In both figures, the critical curve for $\bar{\mu} = 1$ serves as a reference, where the block behaves as an effectively elastic material with vanishing Maxwell stress.

First, consider the case of $\bar{\mu} = 0.6$, shown by red curves in Fig. 11, as the biasing current increases from 0.1 to 0.6. These curves exhibit a pattern similar to the black critical curve for the reference case ($\bar{\mu} = 1$), monotonically decreasing from the thin-plate limit (L_g

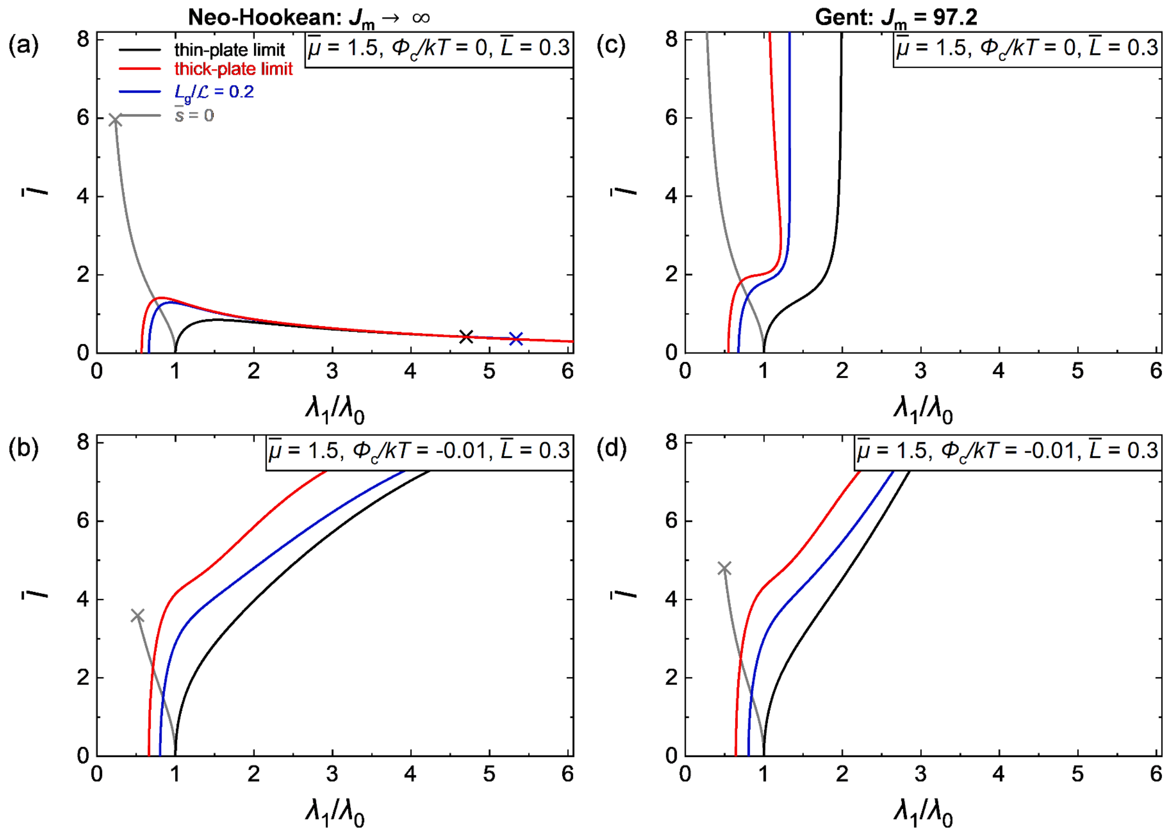

Fig. 10. The wrinkling behavior of ideal MAH blocks immersed in a solvent with varying chemical potentials is analyzed for a normalized permeability $\overline{\mu} = 1.5$ and a relative thickness $\overline{L} = 0.3$. (a) $\Phi_c/kT = 0$ and (b) $\Phi_c/kT = -0.01$ for the neo-Hookean case; (c) $\Phi_c/kT = 0$ and (d) $\Phi_c/kT = -0.01$ for the Gent ($J_m = 97.2$) case. The critical curves of $\overline{I}$ versus λ_1/λ_0 for the thin-plate limit, $L_g/\mathscr{L} = 0.2$, and the thick-plate limit, and the nonlinear response for $\overline{s} = 0$ are depicted by black, blue, red, and gray lines, respectively. All curves satisfy the geometric constraint of the tank ($\lambda_3 \le \lambda_0/\overline{L}$), with the case of $\lambda_3 = \lambda_0/\overline{L}$ marked by crosses.

$/\mathscr{L} = 0$) to the cut-off point at $\lambda_3 = \lambda_0/\overline{L}$. And the critical curves consistently reach the maximum stretch at the thin-plate limit, confirming that wrinkling first occurs at this limit, as suggested in Fig. C4(a).

We then move to the case of $\overline{\mu} = 0.1$ as depicted by the blue curves in Fig. 11. When the current applied is relatively low, see, Fig. 11 (a, d) for $\overline{I} = 0.1$, the critical curves show the same trend as those for other two cases ($\overline{\mu} = 0.6$ and 1.0). The critical stretches for the initiation of wrinkling (in contraction) are observed to increase as $\overline{\mu}$ decreases (1.0→0.6→0.1), with values of 1.0→1.0003→1.0080 and 1.0→1.0003→1.0052, respectively. This suggests that the increasing $\overline{\mu}$ (≤ 1) may stabilize the immersed block, which aligns with previous findings for magnetic soft plates (Xia, 2024).

As the biasing current increases to $\overline{I} = 0.35$, two additional critical curves emerge in Fig. 11(b) for the neo-Hookean case, indicating the first encounter of the wrinkling in extension at $\lambda_1/\lambda_0 = \sim 1.4617$. It should be noted that this critical stretch leads to wrinkling at $L_g/\mathscr{L} = \sim 1.04$, rather than at two previously mentioned limits with $\lambda_1/\lambda_0 = \sim 1.4757$ and ~ 1.4618, respectively. This anomalous local minimum has been reported in our previous work for the wrinkling of compressible soft electroactive plates (Xia et al., 2021), which may be attributed to the compressibility of block. When the biasing current further increases from $\overline{I} = 0.35$ to 0.6, see, Fig. 11(b, c, e, f), the stability of the block deteriorates. The minimum in-plane stretches required to remain stable in the antisymmetric mode are determined by the thick-plate limit at $\lambda_1/\lambda_0 = \sim 4.1242$ and at the thin-plate limit $\lambda_1/\lambda_0 = \sim 1.8297$, respectively. This highlights the stabilizing effect of decreasing the chain extension limit (J_m : ∞→97.2). For other values of applied current, and chemical potentials, the reader may refer to Figs. C8-C11 for additional details, which show the similar pattern.

From Fig. 11, it can be concluded that the geometric constraint of the tank may prevent the appearance of certain specific wrinkling cases but has no influence on the first encounter of wrinkling for immersed MAH blocks with $\overline{\mu} < 1$. This observation encourages us to further investigate the effect of this constraint on the wrinkling behaviors of immersed MAH blocks with $\overline{\mu} > 1$, as shown in Fig. 12. When the applied current is relatively low, see, Fig. 12(a, d) for $\overline{I} = 0.1$, the neo-Hookean and Gent MAH blocks wrinkle in both contraction and extension for $\overline{\mu} = 1.5$ and 2.0. Similar to Fig. 11 for $\overline{\mu} < 1$, wrinkling in contraction is triggered at the thin-plate limit and remains unaffected by the geometric constraint. However, this constraint may prevent wrinkling in extension from occurring at the thin-plate limit as expected. For instance, as seen in Fig. 12(b), such wrinkling is first observed at

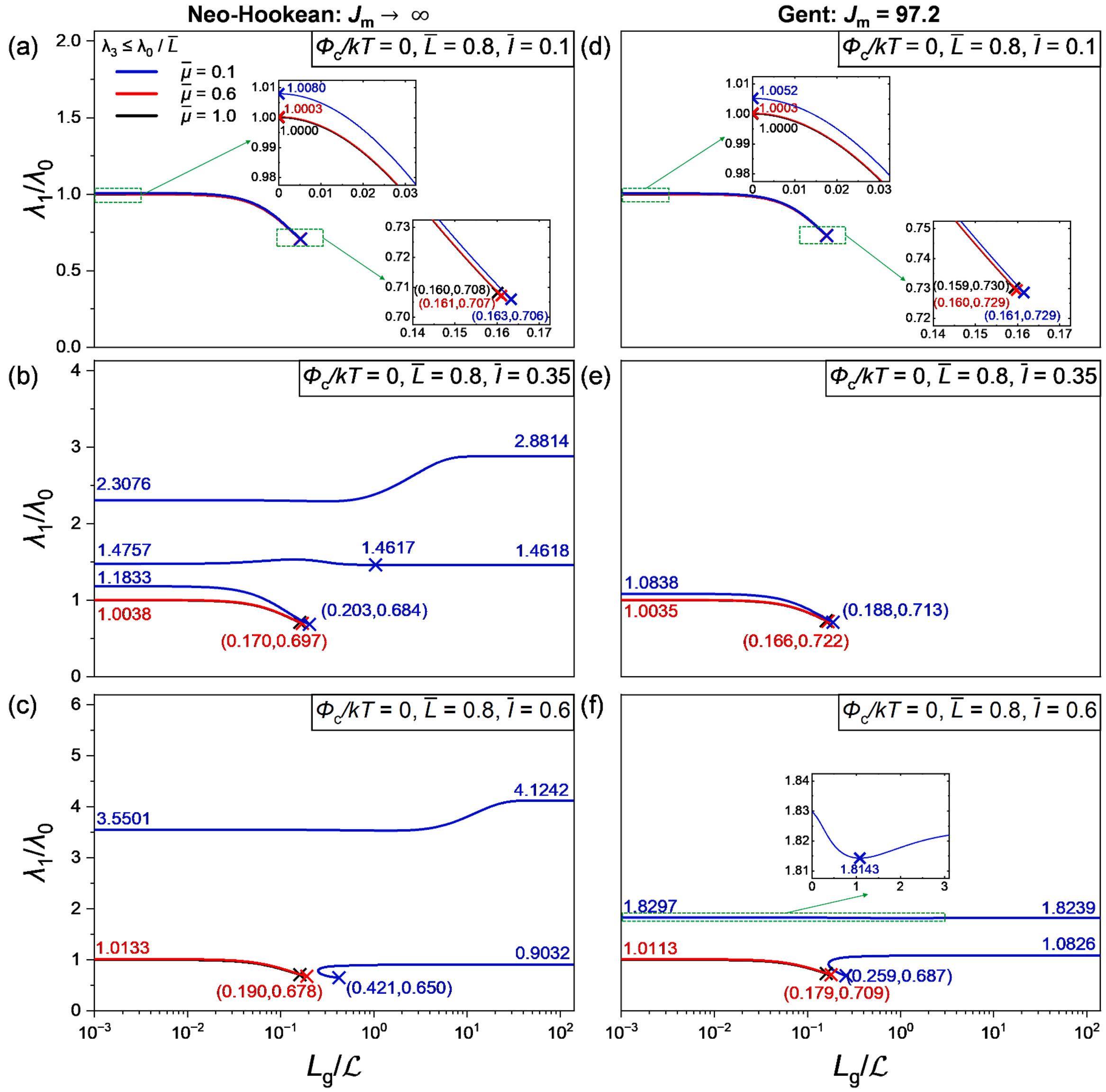

Fig. 11. The critical curves of λ_1/λ_0 versus $L_g/\mathcal{L}$ are shown for ideal MAH blocks with diverse permeabilities ($\bar{\mu} \le 1$) immersed in a solvent with $\Phi_c/kT = 0$ and $\bar{L} = 0.8$. Panels (a)-(c) correspond to the neo-Hookean case with $\bar{I} = 0.1,\ 0.35,\ 0.6$, respectively, while panels (d)-(f) correspond to the Gent ($J_m = 97.2$) case with the same $\bar{I}$ values. The blue, red, and black curves represent antisymmetric wrinkling for blocks with $\bar{\mu} = 0.1,\ 0.6,\ 1.0$, respectively, satisfying the geometric constraint of the tank ($\lambda_3 \le \lambda_0/\bar{L}$). Crosses mark the case where $\lambda_3 = \lambda_0/\bar{L}$.

$(L_g/\mathcal{L}, \lambda_1/\lambda_0) = (\sim 0.116,\ \sim 2.689)$ for $\bar{\mu} = 2.0$. As the biasing current increases ($\bar{I} = 0.35 \to 0.45 \to 0.5 \to 0.55 \to 0.6 \to 0.8 \to 1.0$), see, Figs. 12(b, c, e, f) and C12-C15, the stable region monotonically decreases and eventually vanishes. This again suggests that the immersed blocks with higher $\bar{\mu}$ (≥ 1) are more susceptible to instability, consistent with previous findings for magnetic soft plates (Xia, 2024).

However, an interesting question remains unanswered: Should the excluded critical in-plane stretch for the wrinkling be added to the stable region or not? To address this, we need to clarify whether other compatible stretches $\lambda_3 < \lambda_0/\bar{L}$ exist that can satisfy the out-of-plane boundary condition given in Eq. (18) while maintaining the prescribed in-plane stretches. To this end, the critical touching between the wrinkled MAH block and the tank is investigated, as illustrated in Fig. 13. For example, considering the neo-Hookean cases of $\bar{\mu} = 0.1,\ 0.6,\ 1.0,\ 1.5$ and 2.0, we plot the critical current $\bar{I}$ against the characteristic geometry of wrinkling $L_g/\mathcal{L}$ in Fig. 13(a) and the corresponding curves against the in-plane stretch in Fig. 13(b), respectively. Here the out-of-plane stretch λ_3 is fixed as $\lambda_0/\bar{L}$. Using the case of $\bar{\mu} = 1.0$, see, the black lines in both panels, as a reference, the correspondence between the curves of the same color in Fig. 13(a, b) can be easily identified.

For the case $\bar{\mu} < 1$, the critical $L_g/\mathcal{L}$ initially increases while the critical λ_1/λ_0 decreases with increasing biasing current $\bar{I}$.

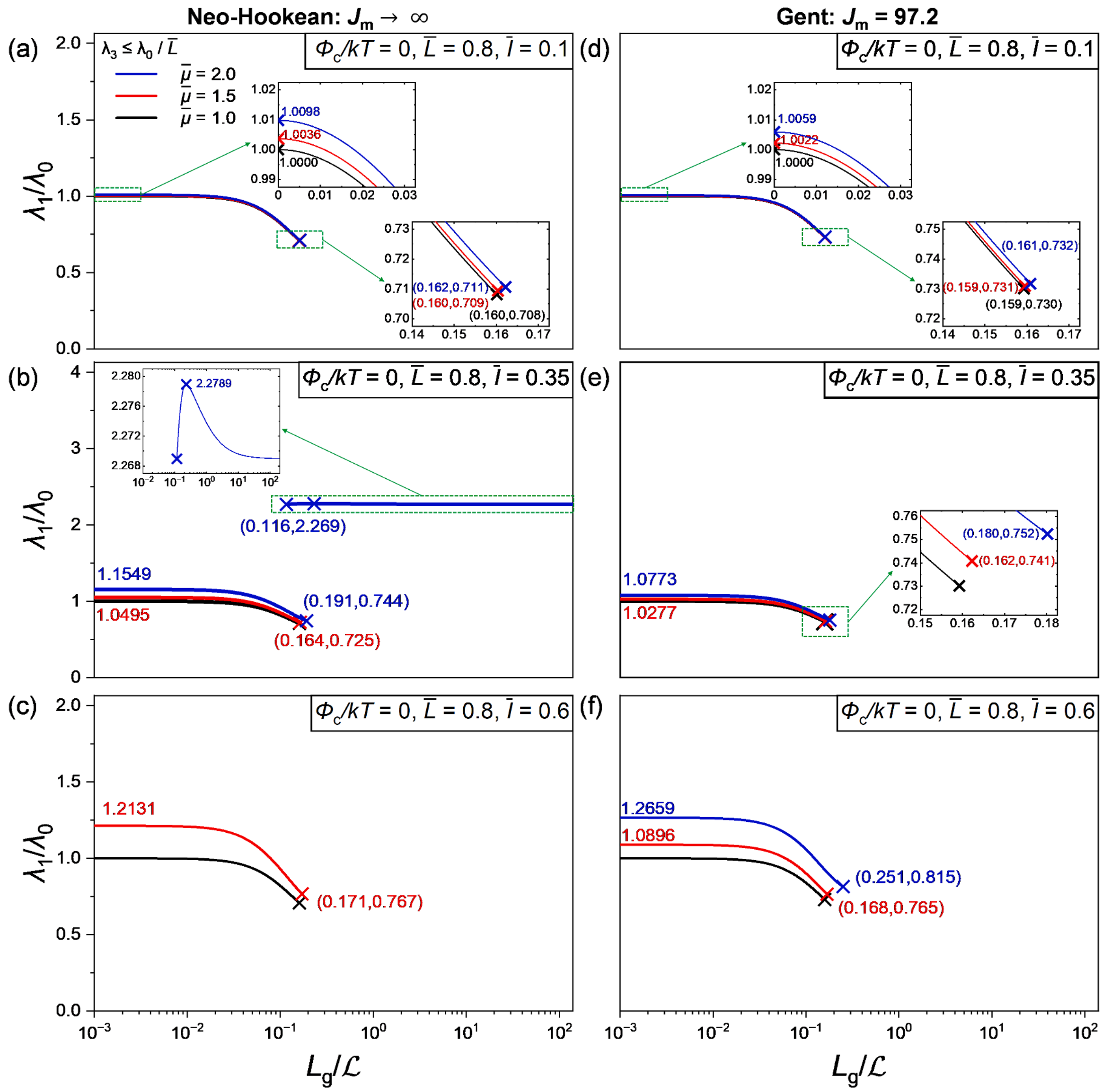

Fig. 12. The critical curves of λ_1/λ_0 versus $L_g/\mathscr{L}$ are shown for ideal MAH blocks with diverse permeabilities ($\bar{\mu} \le 1$) immersed in a solvent with $\Phi_c/kT = 0$ and $\bar{L} = 0.8$. Panels (a)-(c) correspond to the neo-Hookean case with $\bar{I} = 0.1, 0.35, 0.6$, respectively, while panels (d)-(f) correspond to the Gent ($J_m = 97.2$) case with the same $\bar{I}$ values. The blue, red, and black curves represent antisymmetric wrinkling for blocks with $\bar{\mu} = 2.0, 1.5, 1.0$, respectively, satisfying the geometric constraint of the tank ($\lambda_3 \le \lambda_0/\bar{L}$). Crosses mark the case where $\lambda_3 = \lambda_0/\bar{L}$.

Eventually, they both vanish when the current exceeds certain values, e.g., $\bar{I}_{\max}^{\bar{\mu}=0.1} =\sim 0.6146$ and $\bar{I}_{\max}^{\bar{\mu}=0.6} = \sim 1.368$, as seen in Fig. 13(a, b). These extreme values, as marked by crosses, correspond to critical $L_g/\mathscr{L}$ approaching infinity and minimum critical λ_1/λ_0 of ~ 0.6475 and ~ 0.6041, respectively. Recalling the wrinkling behaviors shown in Fig. 11, these critical points always occur during wrinkling in contraction and do not affect the onset of surface instability in the immersed MAH blocks with $\bar{\mu} < 1$.

For the case of $\bar{\mu} > 1$, as shown by the olive and orange curves in Fig. 13(a, b), two branches may exist. Taking the case of $\bar{\mu} = 2.0$ as an example, one branch begins at $(\bar{I}, L_g/\mathscr{L}, \lambda_1/\lambda_0) = (0, \sim 0.1601, \sim 0.7082)$ and ends close to $(\sim 0.5281, +\infty, \sim 0.8273)$, while the other begins at $(\sim 0.3841, 0, \sim 2.0419)$ and ends close to $(\sim 0.3285, +\infty, \sim 2.4343)$. Referring to the wrinkling behaviors as shown in Fig. 12, we suggest that the first branch corresponds to the critical points during wrinkling in contraction, while the second one corresponds to those during wrinkling in extension. Thus, the first branch exhibits a pattern similar to the critical curves for $\bar{\mu} < 1$, whereas the second branch requires further clarification.

We now turn to Fig. 13(c) to examine the nonlinear responses of the immersed MAH blocks with $\bar{\mu} = 1.5$, represented by the curves of λ_3/λ_0 versus λ_1/λ_0 under diverse currents of $\bar{I} = 0.1, 0.2, 0.35, 0.5, 0.6, 0.8$, and 1.0. These response curves exhibit closed-loop behavior, likely due to the interplay between the material compressibility and the tensile Maxwell stress. Notably, the area of these

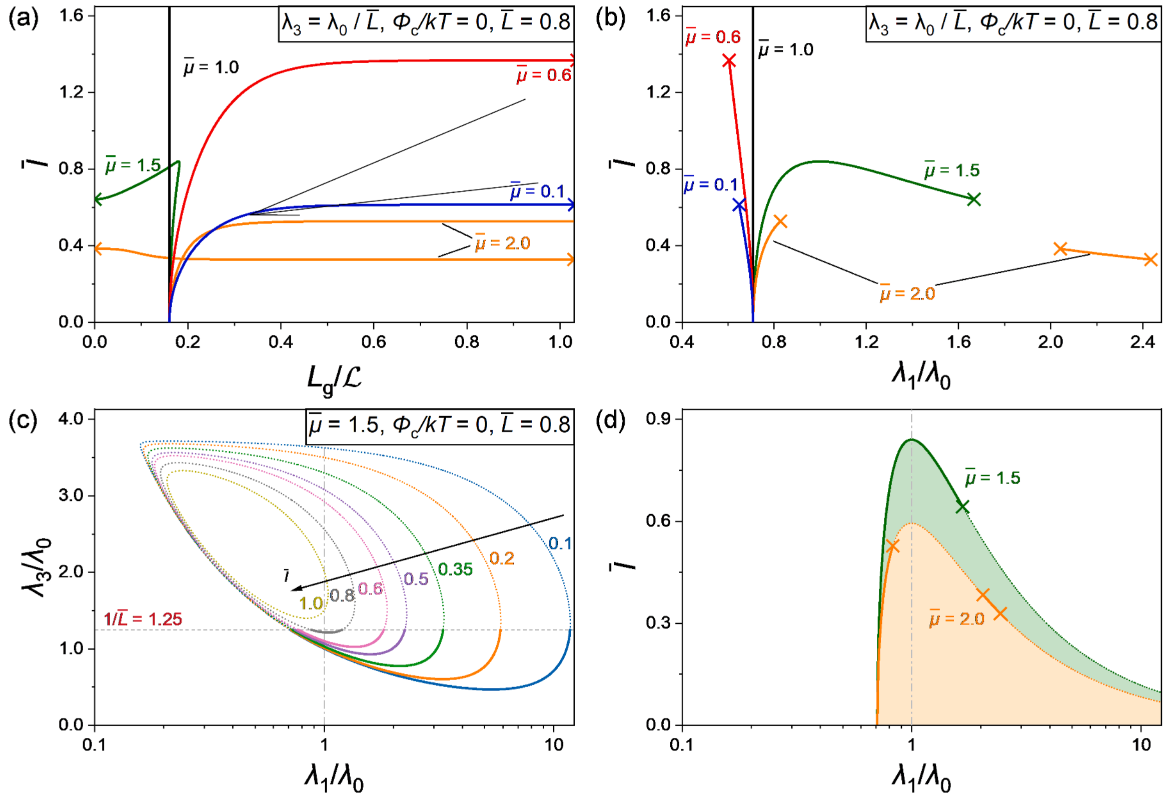

Fig. 13. Encounter of critical touching between the immersed neo-Hookean ideal MAH block during wrinkling and the tank with $\Phi_c/kT = 0$ and $\bar{L} = 0.8$. (a) Critical curves of $\bar{I}$ versus $L_g/\mathscr{L}$ for $\lambda_3 = \lambda_0/\bar{L}$ and $\bar{\mu} = 0.1$, 0.6, 1.0, 1.5 and 2.0; (b) Critical curves of $\bar{I}$ versus λ_1/λ_0 for $\lambda_3 = \lambda_0/\bar{L}$ and $\bar{\mu} = 0.1$, 0.6, 1.0, 1.5 and 2.0; (c) Nonlinear responses under diverse currents $\bar{I} = 0.1$, 0.2, 0.35, 0.5, 0.6, 0.8, 1.0 and $\bar{\mu} = 1.5$; (d) Combination of enlarged critical curves of $\bar{I}$ versus λ_1/λ_0 for $\lambda_3 = \lambda_0/\bar{L}$ and nonlinear responses of the MAH blocks with $\bar{\mu} = 1.5$ and 2.0, respectively. The dotted curves are excluded from the nonlinear responses due to the geometric constraint of the tank ($\lambda_3 \leq \lambda_0/\bar{L}$).

loops monotonically shrinks as the biasing current increases. By applying the geometric constraint, points above the reference line $\lambda_3/\lambda_0 = 1/\bar{L}$ are excluded, as indicated by the dotted curves. Recalling the in-plane stretch of ~ 0.709 for the excluded critical curve in Fig. 12(a) for $\bar{I} = 0.1$, we observe two out-of-plane stretches along the reference line $\lambda_3/\lambda_0 = 1/\bar{L}$, respectively. The critical curves shown in Fig. 13(b) for $\bar{\mu} = 1.5$ and 2.0, with the nonlinear responses under varying biasing currents, are then enlarged in Fig. 13(d). Interestingly, both branches of the critical curve, see, the olive and orange solid curves, in fact belong to the same response curve, see, the olive and orange dotted curves. Since the regions below these response curves define the available range of the in-plane stretch, we can conclude that the geometric constraint may enhance the surface stability by preventing certain critical deformation states that lead to wrinkling in extension. For additional insights, the reader may also refer to Fig. C16, which presents parallel results of the Gent case.

5. Conclusions

5.1. Results of the current paper

This paper presents a comprehensive investigation into the wrinkling instability of a magneto-active hydrogel block under the influence of an external magnetic field. The block is immersed in a tank filled with a magnetic solvent, where a magnetic biasing field is established by an electromagnet with poles situated at the top and bottom of the tank. By incorporating Ampère's circuital law, we formulate the nominal magnetic field intensity as a function of the current passing through the electromagnet's coils.

Utilizing generalized neo-Hookean and Gent ideal magnetoelastic models, we first derive the nonlinear responses characterized by the normalized in-plane nominal stress $\bar{s}$ and the normalized current $\bar{I}$ for the hydrogel block undergoing in-plane biaxial stretching and a transverse magnetic biasing field. The identification of magneto-mechanical instability (if exists) is achieved through the *Hessian criterion*, i.e., $\mathrm{d}\bar{I}/\mathrm{d}\lambda_1 = 0$. We then establish compact explicit bifurcation relations for both antisymmetric and symmetric wrinkling patterns by integrating the surface impedance matrix method with the Stroh formulation.

Through numerical analysis, we have identified two distinct scenarios based on the normalized permeability $\bar{\mu}$.

For the case of $\bar{\mu} < 1$, the nonlinear response curves may exhibit a characteristic pull-in phenomenon, e.g., Figs. 3 and 4, which arises directly from the geometric constraint. While the wrinkling evolution maintains an essential similarity to that observed in magnetoelastic plates without external fields, the critical curves in the thick-plate limit undergo a significant "mutation" around $\lambda_3 = \lambda_0/\overline{L}$. Importantly, although the geometric constraint can inhibit the development of certain wrinkles, it does not affect the initial onset of wrinkling. Furthermore, surface instability intensifies as the normalized permeability decreases, eventually reaching a state equivalent to that of an elastic body when $\overline{\mu} = 1$.

In the contrasting scenario of $\overline{\mu} > 1$, the corresponding nonlinear response curves may show a pull-out instability. However, this abnormal phenomenon may not occur in practice due to the geometric constraint. Increasing $\overline{\mu}$ can significantly destabilize the immersed blocks, leading to wrinkling patterns that differ from those observed in the case of $\overline{\mu} < 1$. Nevertheless, the geometric constraint may suppress such wrinkling conditions to some extent, providing a stabilizing effect on the block.

5.2. Potential implications

MAHs operating in liquid environments are not merely of academic interest but address real technological needs across multiple domains. The revealed pull-in/pull-out phenomena provide fundamental insights into how environmental conditions (e.g., solvent properties) dramatically alter instability mechanisms compared to conventional MAH systems in air. The discovery that geometric constraints suppress certain wrinkling modes—while not affecting initial onset—offers new design principles for controlling surface morphology in fluid-structure-field coupled systems. Our predictions can guide practical implementations for designing smart actuators and sensors operating in aqueous environments.

Potential applications include providing a theoretical understanding of instability-driven mechanisms in untethered magnetic soft actuators (Hu et al., 2018; Huang et al., 2016) and underwater shape-morphing soft machines (Alapan et al., 2020), as well as modulating the release kinetics of magnetically controlled drug delivery systems (Li and Mooney, 2016; Zhao et al., 2011). Additionally, our findings can aid in preventing failure in lab-on-chip devices fabricated using ferrofluids and soft magnetic materials (Nguyen et al., 2007). Furthermore, recent work on ferrogels—hydrogels with embedded magnetic particles immersed in carrier fluids (Thévenot et al., 2013; Zrínyi et al., 1997)—demonstrates the practical feasibility of such systems.

Our theoretical framework provides the predictive capability to rationally design these systems, enabling the determination of critical field strengths, optimal permeability ratios, and geometric constraints to achieve desired morphological transitions while avoiding unwanted instabilities.

5.3. Limitations

In the present work, we adopt a quasi-static approach by focusing on the mechanical stability of the hydrogel after it has reached thermodynamic equilibrium with a solvent. At this equilibrium state, the chemical potential of the solvent molecules within the gel network equals that in the external solvent. This simplification allows us to decouple the mechanical instability problem from the transient diffusion dynamics, enabling a tractable analytical framework for understanding the fundamental wrinkling mechanics under magnetic actuation. However, this simplification neglects the potential influence of transient chemo-mechanical coupling on the onset and evolution of instabilities. It should be noted that the time-dependent inhomogeneous swelling may trigger different instability modes during the transient phase. Future research should incorporate transient chemo-mechanical coupling effects to provide a more comprehensive understanding of magneto-active hydrogel instabilities.

In addition, the application of a magnetic field can influence both the viscosity and diffusivity of magnetic solvents or magnetic soft materials. For the latter, such as magnetorheological elastomers, this may lead to magnetic-driven anisotropy due to the redistribution of magneto-active components (Gonzalez-Saiz et al., 2025). This anisotropy inevitably introduces additional complexity in predicting the surface instability of MAH blocks, potentially either enhancing or suppressing the onset of wrinkling when compared to the isotropic case. To simplify the mathematical modeling, we assume field-independent diffusion in our work, which is consistent with the standard framework widely used in the active gel study (Gebhart and Wallmersperger, 2019; Liu et al., 2023; Tang et al., 2025; Xia, 2025). Previous theoretical and experimental studies on similar systems have routinely decoupled the magnetic effects from the mass transport process (Garcia-Gonzalez and Landis, 2020; Gonzalez-Rico et al., 2024). This approach is justified when the characteristic time for magnetic particle reorganization is much shorter than that of solvent diffusion, allowing these processes to be treated separately in the leading-order approximation.

CRediT authorship contribution statement

Guozhan Xia: Writing – original draft, Visualization, Methodology, Funding acquisition, Formal analysis, Conceptualization. **Renwei Mao:** Writing – review & editing, Writing – original draft, Validation, Investigation, Formal analysis. **Weiqiu Chen:** Writing – review & editing, Validation, Supervision, Funding acquisition. **Yipin Su:** Writing – review & editing, Validation, Supervision, Resources, Methodology, Funding acquisition.

Declaration of competing interest

The authors declare that they have no known competing financial interests or personal relationships that could have appeared to influence the work reported in this paper.

Acknowledgments

The work was supported by the National Natural Science Foundation of China (Nos. 12202171, 12192210 and 12402193), the specialized research projects of Huanjiang Laboratory, Zhuji, Zhejiang Province, as well as the 111 Project (No. B21034). The first author would like to thank Prof. Wei Hong at Southern University of Science and Technology for his invaluable suggestions on the realistic generation of the magnetic biasing field, as well as the research group led by Prof. Diego Misseroni at the University of Trento for fostering a supportive and open academic environment, which greatly facilitated the completion of this work.

Appendix A. Nonlinear magnetoelasticity and its linearized incremental version

The primary motivation of this section is to provide additional details about the formulations presented in the main text. The appendix is self-contained, and some expressions from the main text are repeated for the sake of readability.

As assumed in the main text, the MAH block swelling in a solvent with magneto-mechanical biasing fields always stays in an equilibrium state, allowing it to be treated as an effective magneto-active elastomer. Hence, we begin by introducing the nonlinear field theory of soft magneto-active (SMA) materials, following the framework established by Dorfmann and Ogden (2014). Taking the virtual dry network as the reference configuration, the "gel" body initially occupies a region, Ω_0, with boundary, $\partial\Omega_0$, where any material element is denoted by its position vector, $\boldsymbol{X}(X_1, X_2, X_3)$. When the dry body absorbs the solvent and reaches an equilibrium state under mechanical load and magnetic stimuli, the material points in the body move to new positions, one of which is described by spatial coordinates, $\boldsymbol{x}(x_1, x_2, x_3)$ in the initial configuration. The gel in such state occupies a new region of Ω with boundary of $\partial\Omega$. The overall deformation of the body can be defined via the deformation gradient $\boldsymbol{F} = \partial\boldsymbol{x}/\partial\boldsymbol{X}$, with the volume ratio $J = \det\boldsymbol{F}$. The left and right Cauchy-Green tensors associated with the deformation gradient are given by $\boldsymbol{b} = \boldsymbol{F}\boldsymbol{F}^{\mathrm{T}}$ and $\boldsymbol{c} = \boldsymbol{F}^{\mathrm{T}}\boldsymbol{F}$, respectively, where the superscript "T" denotes transpose. The free energy density function of the gel $W(\boldsymbol{F}, \boldsymbol{B}_{\mathrm{l}})$ satisfies $W(\boldsymbol{I}, 0) = 0$, where $\boldsymbol{I}$ is the identity tensor for undeformed state, $\boldsymbol{B}_{\mathrm{l}}$ is the nominal magnetic induction field. The nonlinear constitutive relations are then expressed as

$$\boldsymbol{T} = \frac{\partial W}{\partial \boldsymbol{F}}, \quad \boldsymbol{H}_{\mathrm{l}} = \frac{\partial W}{\partial \boldsymbol{B}_{\mathrm{l}}}, \tag{A1}$$

where the nominal stress tensor $\boldsymbol{T} = J\boldsymbol{F}^{-1}\boldsymbol{\tau}$ and the nominal magnetic field intensity $\boldsymbol{H}_{\mathrm{l}} = \boldsymbol{F}^{\mathrm{T}}\boldsymbol{H}$ are the pull-back versions of the Cauchy stress $\boldsymbol{\tau}$ and the true magnetic field $\boldsymbol{H}$. For a general isotropic and homogeneous SMA body, the constitutive relations can be further expressed as

$$\begin{aligned} J\boldsymbol{\tau} &= 2W_1\boldsymbol{b} + 2W_2\left(I_1\boldsymbol{b} - \boldsymbol{b}^2\right) + 2I_3W_3\boldsymbol{I} + 2J^2W_5\boldsymbol{B}\otimes\boldsymbol{B} + 2W_6J^2(\boldsymbol{B}\otimes\boldsymbol{b}\boldsymbol{B} + \boldsymbol{b}\boldsymbol{B}\otimes\boldsymbol{B}), \\ J\tau_{ji} &= 2W_1b_{ji} + 2W_2\left(I_1b_{ji} - b_{jk}b_{ki}\right) + 2W_3I_3\delta_{ji} + 2J^2W_5B_jB_i + 2W_6J^2\left(B_jb_{ik}B_k + b_{jk}B_kB_i\right), \end{aligned} \tag{A2}$$

$$\boldsymbol{H} = 2J\left(W_4\boldsymbol{b}^{-1}\boldsymbol{B} + W_5\boldsymbol{B} + W_6\boldsymbol{b}\boldsymbol{B}\right), \quad H_k = 2J\left(W_4b_{ki}^{-1}B_i + W_5B_k + W_6b_{ik}B_i\right), \tag{A3}$$

where $i,\ j,\ k = 1,\ 2,\ 3$, $W_m = \partial W/\partial I_m$ ($m = 1,\ 2,\ \ldots,\ 6$), the true magnetic induction field $\boldsymbol{B}$ is related to the nominal one by $\boldsymbol{B} = J^{-1}\boldsymbol{F}\boldsymbol{B}_{\mathrm{l}}$, and the six independent invariants for isotropic SMA gels are given by: $I_1 = \mathrm{tr}\boldsymbol{c}$, $I_2 = \left[(\mathrm{tr}\boldsymbol{c})^2 - \mathrm{tr}\left(\boldsymbol{c}^2\right)\right]/2$, $I_3 = \det\boldsymbol{c}$, $I_4 = \boldsymbol{B}_{\mathrm{l}}\cdot\boldsymbol{B}_{\mathrm{l}}$, $I_5 = \boldsymbol{B}_{\mathrm{l}}\cdot(\boldsymbol{c}\boldsymbol{B}_{\mathrm{l}})$, $I_6 = \boldsymbol{B}_{\mathrm{l}}\cdot\left(\boldsymbol{c}^2\boldsymbol{B}_{\mathrm{l}}\right)$.

The constitutive relations in Eqs. (A2) and (A3) are rather lengthy but can be significantly simplified for some special forms of the free energy density. In this study, the free energy of a polymeric gel arises from stretching, and we adopt the following form for the free energy density function

$$W = W_{\mathrm{s}} + W_{\mathrm{m}} + W_{\mathrm{p}} - \Phi_{\mathrm{c}}C, \tag{A4}$$

where Φ_{c} is the constant chemical potential of the swollen gel or external solvent at equilibrium, C is the nominal concentration of the solvent in the gel, and W_{s}, W_{m} and W_{p} represent the free energy contributions from the stretching of the polymer network, the mixing between the polymer network and solvent, and the polarization of the gel. Below, we describe each of these contributions in detail. First, the free energy associated with stretching the polymer network is given by (e.g., Flory (1953))

$$W_{\mathrm{s}} = \frac{1}{2}NkT(F_{iK}F_{iK} - 3 - 2\ln J) = \frac{1}{2}NkT(I_1 - 3 - \ln I_3), \tag{A5}$$

where N is the number of polymer chains per unit volume of the dry network, k is the Boltzmann constant and T is the temperature.

Second, the free energy of mixing the polymers and the solvent takes the form (Flory, 1942; Huggins, 1941)

$$W_{\mathrm{m}} = -\frac{kT}{\varpi}\left[\left(\sqrt{I_3} - 1\right)\ln\left(1 + \frac{1}{\sqrt{I_3} - 1}\right) + \frac{\chi}{\sqrt{I_3}}\right], \tag{A6}$$

where ϖ is the volume per solvent molecule, and χ is a dimensionless parameter characterizing the enthalpy of mixing. Here, the assumption of molecular incompressibility is applied implicitly, leading to

$$J = 1 + \varpi C. \tag{A7}$$

In this paper, we assume the gel is an ideal magneto-elastic body (Xia, 2024), with the free energy of polarization given by

$$W_{\mathrm{p}} = \frac{\boldsymbol{B}^2}{2\mu} = \frac{I_5}{2\mu\sqrt{I_3}}, \tag{A8}$$

where μ is the total magnetic permeability of the gel. This implies that the magnetic constitutive Eq. (A3) is not influenced by deformation. However, since the magnetic properties of the solvent and the network molecules are usually different, the total permeability is thus a function of the solvent concentration, $\mu(C)$. The effective magnetic permeability of the gel may be estimated based on the volumetric average of the fluid and the solid phases as

$$\mu = \frac{\mu_{\mathrm{s}} + \varpi C \mu_{\mathrm{f}}}{\varpi C + 1}, \tag{A9}$$

where μ_{f} and μ_{s} are the permeability of the fluid and the solid phases, respectively.

By substituting Eqs. (A5), (A6) and (A8) into (A4) and incorporating the constraint (A7), we construct the specific free energy function in terms of deformation gradient $\boldsymbol{F}$, the nominal magnetic induction field $\boldsymbol{B}_{\mathrm{l}}$, and chemical potential of solvent, μ, as

$$W(I_1, I_3, I_5) = W_{\mathrm{s}}(I_1, I_3) + W_{\mathrm{m}}(I_3) + \frac{I_5}{2\mu\sqrt{I_3}} - \frac{\Phi_{\mathrm{c}}}{\varpi}\left(\sqrt{I_3} - 1\right). \tag{A10}$$

Correspondingly, the nonlinear response and magnetic field of the gel simplify to

$$\tau = \frac{2W_1}{J}[\boldsymbol{b} - (\zeta - \psi)\boldsymbol{I}] + \frac{1}{\mu}\left(\boldsymbol{B}\otimes\boldsymbol{B} - \frac{1}{2}\boldsymbol{B}\cdot\boldsymbol{B}\boldsymbol{I}\right), \quad \tau_{ji} = \frac{2W_1}{J}\left[b_{ji} - (\zeta - \psi)\delta_{ji}\right] + \frac{1}{\mu}\left(B_j B_i - \frac{1}{2}B_m B_m \delta_{ji}\right), \tag{A11}$$

$$\boldsymbol{H} = \boldsymbol{B}/\mu, \quad H_k = B_k/\mu, \tag{A12}$$

where $\boldsymbol{I}$ is the identity tensor, and

$$\zeta = \frac{J^2}{W_1}\left(W_3 + 2J^2 W_{33}\right) - \frac{J B_m B_m}{2W_1\mu}, \quad \psi = \frac{2J^2}{W_1}\left(W_3 + J^2 W_{33}\right) - \frac{J B_m B_m}{4W_1\mu}, \tag{A13}$$

with $W_{33} = \partial^2 W/\partial I_3^2$. Here and below, repeated indices follow the Einstein summation convention unless otherwise stated.

For the wrinkling problem presented in the main text, the magnitude of wrinkles can be approximated as an incremental infinitesimal perturbation superimposed on the constrained swelling state. We denote the infinitesimal deformation by $\dot{\boldsymbol{x}}$, where dotted variables represent incremental quantities. For example, $\dot{\boldsymbol{T}}$, $\dot{\boldsymbol{H}}_{\mathrm{l}}$, and $\dot{\boldsymbol{B}}_{\mathrm{l}}$ are increments in $\boldsymbol{T}$, $\boldsymbol{H}_{\mathrm{l}}$, and $\boldsymbol{B}_{\mathrm{l}}$, respectively. In this manner, the incremental equilibrium equations can be written in the Eulerian form as

$$\mathrm{div}\dot{\boldsymbol{T}}_0 = 0, \quad \mathrm{curl}\dot{\boldsymbol{H}}_{\mathrm{l}0}, \quad \mathrm{div}\dot{\boldsymbol{B}}_{\mathrm{l}0} = 0, \tag{A14}$$

where $\dot{\boldsymbol{T}}_0 = J^{-1}\boldsymbol{F}\dot{\boldsymbol{T}}$, $\dot{\boldsymbol{H}}_{\mathrm{l}0} = \boldsymbol{F}^{-\mathrm{T}}\dot{\boldsymbol{H}}_{\mathrm{l}}$, and $\dot{\boldsymbol{B}}_{\mathrm{l}0} = J^{-1}\boldsymbol{F}\dot{\boldsymbol{B}}_{\mathrm{l}}$ are "push-forward" versions of the incremental stress, incremental magnetic field vector, and incremental magnetic induction vector, respectively. The corresponding constitutive equations can be obtained by linear differentiation of Eq. (A1) and rearranged as

$$\dot{\boldsymbol{T}}_0 = \mathscr{A}_0\boldsymbol{L} + \boldsymbol{\Gamma}_0\dot{\boldsymbol{B}}_{\mathrm{l}0}, \quad \dot{\boldsymbol{H}}_{\mathrm{l}0} = \boldsymbol{\Gamma}_0^{\mathrm{T}}\boldsymbol{L} + \boldsymbol{K}_0\dot{\boldsymbol{B}}_{\mathrm{l}0}, \tag{A15}$$

where $\mathscr{A}_0$, $\boldsymbol{\Gamma}_0$, and $\boldsymbol{K}_0$ are the fourth-, third-, and second-order instantaneous material tensors, respectively. Their components are defined by

$$\mathscr{A}_{0jilk} = J^{-1}F_{j\alpha}F_{l\beta}\left(\sum_{m=1,m\neq 4}^{6}\sum_{n=1,n\neq 4}^{6} W_{mn}\frac{\partial I_m}{\partial F_{i\alpha}}\frac{\partial I_n}{\partial F_{k\beta}} + \sum_{m=1,m\neq 4}^{6} W_m\frac{\partial^2 I_m}{\partial F_{i\alpha}\partial F_{k\beta}}\right) = \mathscr{A}_{0lkji}, \tag{A16}$$

$$\Gamma_{0jik} = F_{j\alpha}F_{\beta k}^{-1}\left(\sum_{m=1,m\neq 4}^{6}\sum_{n=4}^{6} W_{mn}\frac{\partial I_m}{\partial F_{i\alpha}}\frac{\partial I_n}{\partial B_{\mathrm{l}\beta}} + \sum_{m=5}^{6} W_m\frac{\partial^2 I_m}{\partial F_{i\alpha}\partial B_{\mathrm{l}\beta}}\right) = \Gamma_{0ijk}, \tag{A17}$$

$$K_{0jk} = JF_{\alpha j}^{-1}F_{\beta k}^{-1}\left(\sum_{m=4}^{6}\sum_{n=4}^{6} W_{mn}\frac{\partial I_m}{\partial B_{\mathrm{l}\alpha}}\frac{\partial I_n}{\partial B_{\mathrm{l}\beta}} + \sum_{m=4}^{6} W_m\frac{\partial^2 I_m}{\partial B_{\mathrm{l}\alpha}\partial B_{\mathrm{l}\beta}}\right) = K_{0kj}, \tag{A18}$$

where $W_{mn} = \partial^2 W/(\partial I_m \partial I_n)$. The Roman and Greek subscripts correspond to the reference and initial configurations, respectively. $\boldsymbol{L} = \mathrm{grad}\boldsymbol{u}$ is the displacement gradient with respect to $\boldsymbol{x}$ and $\boldsymbol{u} = \dot{\boldsymbol{x}}(\boldsymbol{X}) = \boldsymbol{u}(\boldsymbol{x})$ is the incremental displacement vector. With substitution of $\boldsymbol{F} = \mathrm{diag}(\lambda_1, \lambda_2, \lambda_3)$ and combination of Eqs. (A10)), (A16)-(A18) reduce to

$$\mathscr{A}_{0jilk} = 2J^{-1}W_1\left[F_{j\alpha}F_{l\alpha}\delta_{ik} + \psi\delta_{ji}\delta_{lk} + (\zeta - \psi)\delta_{jk}\delta_{li}\right] + \mu^{-1}\left[B_j B_l \delta_{ik} - \delta_{ji}B_l B_k - \delta_{lk}B_j B_i + \frac{1}{2}B_m B_m\left(\delta_{ji}\delta_{lk} + \delta_{jk}\delta_{li}\right)\right] = \mathscr{A}_{0lkji}, \tag{A19}$$

$$\Gamma_{0jik} = \mu^{-1}\left(\delta_{jk}B_i + \delta_{ki}B_j - \delta_{ji}B_k\right) = \Gamma_{0ijk}, \tag{A20}$$

$$K_{0jk} = \mu^{-1}\delta_{jk} = K_{0kj}, \tag{A21}$$

with the following nonzero components:

$$\begin{aligned}
&\mathscr{A}_{01111} = 2J^{-1}W_1\left(\lambda_1^2+\zeta\right) + \mu^{-1}B_3^2,\ \mathscr{A}_{02222} = 2J^{-1}W_1\left(\lambda_2^2+\zeta\right) + \mu^{-1}B_3^2,\\
&\mathscr{A}_{03333} = 2J^{-1}W_1\left(\lambda_3^2+\zeta\right),\ \mathscr{A}_{01122} = 2J^{-1}W_1\psi + \mu^{-1}B_3^2/2,\\
&\mathscr{A}_{01133} = \mathscr{A}_{03311} = \mathscr{A}_{02233} = \mathscr{A}_{03322} = 2J^{-1}W_1\psi - \mu^{-1}B_3^2/2,\\
&\mathscr{A}_{01212} = \mathscr{A}_{01313} = 2J^{-1}W_1\lambda_1^2,\ \mathscr{A}_{02121} = \mathscr{A}_{02323} = 2J^{-1}W_1\lambda_2^2,\\
&\mathscr{A}_{01221} = \mathscr{A}_{02112} = \mathscr{A}_{01331} = \mathscr{A}_{03113} = \mathscr{A}_{02332} = \mathscr{A}_{03223} = 2J^{-1}W_1(\zeta-\psi) + \mu^{-1}B_3^2/2,\\
&\mathscr{A}_{03131} = \mathscr{A}_{03232} = 2J^{-1}W_1\lambda_3^2 + \mu^{-1}B_3^2,
\end{aligned} \tag{A22}$$

$$\Gamma_{0113} = \Gamma_{0223} = -\mu^{-1}B_3,\ \Gamma_{0131} = \Gamma_{0311} = \Gamma_{0232} = \Gamma_{0322} = \Gamma_{0333} = \mu^{-1}B_3, \tag{A23}$$

$$K_{011} = K_{022} = K_{033} = \mu^{-1}. \tag{A24}$$

With the effect of the external magnetic field considered, the incremental boundary conditions are generally given by

$$\left[\dot{\boldsymbol{T}}_0^{\mathrm{T}} - \dot{\boldsymbol{\tau}}^* + \boldsymbol{\tau}^*\boldsymbol{L}^{\mathrm{T}} - (\mathrm{div}\boldsymbol{u})\boldsymbol{\tau}^*\right]\boldsymbol{n} = \dot{\boldsymbol{t}}_{\mathrm{a}},\quad \left[\dot{\boldsymbol{B}}_{l0} + \boldsymbol{L}\boldsymbol{B}^* - \dot{\boldsymbol{B}}^* - (\mathrm{div}\boldsymbol{u})\boldsymbol{B}^*\right]\cdot\boldsymbol{n} = 0,\quad \left(\dot{\boldsymbol{H}}_{l0} - \boldsymbol{L}^{\mathrm{T}}\boldsymbol{H}^* - \dot{\boldsymbol{H}}^*\right)\times\boldsymbol{n} = 0, \tag{A25}$$

where $\dot{\boldsymbol{t}}_{\mathrm{a}}$ denotes the incremental mechanical traction per unit area on $\partial\Omega$, the Maxwell stress tensor $\boldsymbol{\tau}^*$ outside the material reads

$$\boldsymbol{\tau}^* = (\mu')^{-1}\left[\boldsymbol{B}^*\otimes\boldsymbol{B}^* - \frac{1}{2}(\boldsymbol{B}^*\cdot\boldsymbol{B}^*)\boldsymbol{I}\right], \tag{A26}$$

and its incremental version $\dot{\boldsymbol{\tau}}^*$ becomes

$$\dot{\boldsymbol{B}}^* = \mu'\dot{\boldsymbol{H}}^*,\quad \dot{\boldsymbol{\tau}}^* = (\mu')^{-1}[\dot{\boldsymbol{B}}^*\otimes\boldsymbol{B}^* + \boldsymbol{B}^*\otimes\dot{\boldsymbol{B}}^* - (\dot{\boldsymbol{B}}^*\cdot\boldsymbol{B}^*)\boldsymbol{I}]. \tag{A27}$$

In the present case, magnetization is ignored. Hence, the external magnetic induction $\boldsymbol{B}^*$ relates to the external magnetic field intensity $\boldsymbol{H}^*$ by $\boldsymbol{B}^* = \mu'\boldsymbol{H}^*$, and their increments follow $\dot{\boldsymbol{B}}^* = \mu'\dot{\boldsymbol{H}}^*$. Here μ' is the permeability exterior to the material.

Appendix B. In-plane wrinkles under out-of-plane magnetic bias

In this appendix we focus on the formation of wrinkles on the traction-free surface of the MAH block using linearized incremental theory of magneto-elasticity (Dorfmann and Ogden, 2014). The incremental fields induced by wrinkling are assumed to be harmonic in one of the in-plane principal direction and exhibit a plane-strain character. Without loss of generality, we consider two dimensional (2D) wrinkles characterized by the incremental displacement $\boldsymbol{u} = \boldsymbol{u}(x_1, x_3)$ and incremental magnetic scalar potential $\dot{\varphi} = \dot{\varphi}(x_1, x_3)$. The incremental magnetic scalar potential $\dot{\varphi}$ is defined via $\dot{\boldsymbol{H}}_{l0} = -\mathrm{grad}\dot{\varphi}$, where dotted variables represent incremental quantities throughout this analysis.

B.1. Stroh Formulation

Following the solution routine as shown in Xia (2024) but omitting details, we may formulate the boundary value problem of wrinkling in the Stroh form and then obtain the bifurcation relations by utilizing the surface impedance matrix method. We use the following form

$$\{u_1, u_3, \dot{B}_{l03}, \dot{T}_{031}, \dot{T}_{033}, \dot{\varphi}\} = \mathrm{e}^{\mathrm{i}kx_1}\{k^{-1}U_1, k^{-1}U_3, \mathrm{i}\Delta, \mathrm{i}\Sigma_{31}, \mathrm{i}\Sigma_{33}, k^{-1}\Phi\}, \tag{B1}$$

where u_1 and u_3 are the components of the incremental displacement in x_1- and x_3-directions, respectively, $\dot{T}_{031}$ and $\dot{T}_{033}$ are the corresponding incremental stresses at the main surfaces of gel, $\dot{B}_{l03}$ is the only non-zero component of the incremental magnetic induction field, U_1, U_3, Σ_{31}, Σ_{33}, Δ and Φ are functions of kx_3 only, $\mathscr{L} = 2\pi/k$ is the 'wavelength' of wrinkles with k being the positive 'wavenumber'.

We introduce the non-dimensional Stroh vector as $\bar{\boldsymbol{\eta}} = [\bar{\boldsymbol{U}} \quad \bar{\boldsymbol{S}}]^{\mathrm{T}}$ with following normalization notations implicitly applied

$$\bar{\boldsymbol{U}} = [\bar{U}_1 \quad \bar{U}_3 \quad \bar{\Delta}]^{\mathrm{T}} = \left[U_1 \quad U_3 \quad \Delta\Big/\sqrt{G\mu_g}\right]^{\mathrm{T}},\quad \bar{\boldsymbol{S}} = [\bar{\Sigma}_{31} \quad \bar{\Sigma}_{33} \quad \bar{\Phi}]^{\mathrm{T}} = \left[\Sigma_{31}/G \quad \Sigma_{33}/G \quad \Phi\sqrt{\mu_g/G}\right]^{\mathrm{T}}, \tag{B2}$$

where G denotes the initial shear modulus of the gel block. Here, the superimposed bar indicates a dimensionless measure throughout the paper. The boundary value problem can then be expressed in the Stroh form as

$$\bar{\boldsymbol{\eta}}^{\cdot} = \mathrm{i}\bar{\boldsymbol{N}}\bar{\boldsymbol{\eta}} = \mathrm{i}\begin{bmatrix} \bar{\boldsymbol{N}}_1 & \bar{\boldsymbol{N}}_2 \\ \bar{\boldsymbol{N}}_3 & \bar{\boldsymbol{N}}_1^{\dagger} \end{bmatrix}\bar{\boldsymbol{\eta}}, \tag{B3}$$

where $\bar{\boldsymbol{N}}$ is the Stroh matrix and "†" denotes the Hermitian operator, and

$$\begin{aligned} \bar{\boldsymbol{N}}_1 &= \begin{bmatrix} 0 & \bar{\tau}_{33}/\bar{a}_1 - 1 & 0 \\ -\bar{a}_3/\bar{a}_2 & 0 & -\bar{c}_1/\bar{a}_2 \\ 0 & -\bar{b}_1\bar{\tau}_{33}/\bar{a}_1 & 0 \end{bmatrix}, \quad \bar{\boldsymbol{N}}_2 = \begin{bmatrix} 1/\bar{a}_1 & 0 & -\bar{b}_1/\bar{a}_1 \\ 0 & 1/\bar{a}_2 & 0 \\ -\bar{b}_1/\bar{a}_1 & 0 & \bar{a}_4/\bar{a}_1 \end{bmatrix}, \\ \bar{\boldsymbol{N}}_3 &= \begin{bmatrix} \bar{a}_3^2/\bar{a}_2 - a_5 & 0 & \bar{a}_3\bar{c}_1/\bar{a}_2 - \bar{c}_2 \\ 0 & \bar{\tau}_{33}^2/\bar{a}_1 - \bar{\tau}_{33} - \bar{\tau}_{11} & 0 \\ \bar{a}_3\bar{c}_1/\bar{a}_2 - \bar{c}_2 & 0 & \bar{c}_1^2/\bar{a}_2 - \bar{d}_1 \end{bmatrix}. \end{aligned} \tag{B4}$$

Here, $\bar{a}_1,\ldots,\bar{a}_5$, $\bar{b}_1$, $\bar{c}_1$, $\bar{c}_2$, $\bar{d}_1$ are magneto-elastic coefficients evaluated for a given biasing fields and a specific constitutive model with general expressions provided in Xia (2024). Additionally, $\bar{\tau}_{11} = \tau_{11}/G$ and $\bar{\tau}_{33} = \tau_{33}/G$ are normalized Cauchy stresses. In this study, we consider the effect of magnetic field exterior to the block, yielding: $\bar{\tau}_{33} = \tau_{33}^{*}/G = \bar{\mu}\bar{B}_3^2/2$ with $\bar{\mu} = \mu_{\mathrm{g}}/\mu_{\mathrm{f}}$ and $\bar{B}_3 = B_3 / \sqrt{G\mu_{\mathrm{g}}}$.

For Eq. (B3), where the Stroh matrix $\bar{\boldsymbol{N}}$ has constant entries, the solution can be expressed in an exponential form as

$$\bar{\boldsymbol{\eta}}(kx_3) = \begin{bmatrix} \bar{\boldsymbol{U}}(kx_3) \\ \bar{\boldsymbol{S}}(kx_3) \end{bmatrix} = \sum_{j=1}^{6} h_j \bar{\boldsymbol{\eta}}^{(j)} \mathrm{e}^{\mathrm{i}p_j kx_3}, \tag{B5}$$

where h_j are undetermined parameters, and p_j are the eigenvalues obtained from the characteristic equations:

$$\det(\bar{\boldsymbol{N}} - p\boldsymbol{I}) = 0. \tag{B6}$$

Substituting Eqs. (B3) and (B4) into Eq. (B6) yields a bicubic equation:

$$\begin{aligned} &(\bar{a}_5\bar{d}_1 - \bar{c}_2^2)\left[\bar{a}_1\bar{a}_4 - (\bar{b}_1^2 - \bar{a}_4)(\bar{\tau}_{11} - \bar{\tau}_{33})\right] + \left\{ \begin{aligned} &\bar{d}_1(\bar{b}_1^2 - \bar{a}_4)(\bar{\tau}_{33} - \bar{a}_3)^2 + 2\bar{c}_1\bar{c}_2(\bar{b}_1^2 - \bar{a}_4)(\bar{\tau}_{33} - \bar{a}_3) \\ &+\bar{a}_1[(\bar{d}_1\bar{a}_4 - \bar{a}_5)(\bar{\tau}_{11} + \bar{\tau}_{33}) + 2(\bar{a}_5 - \bar{b}_1\bar{c}_2)\bar{\tau}_{11}] + \bar{a}_5(\bar{a}_1 - \bar{b}_1\bar{c}_1)^2 \\ &+\bar{a}_1[\bar{a}_4(\bar{c}_1\bar{c}_2 - \bar{a}_3\bar{d}_1) + \bar{c}_2(\bar{a}_4\bar{c}_1 + \bar{a}_3\bar{b}_1) - \bar{a}_3(\bar{a}_4\bar{d}_1 - \bar{b}_1\bar{c}_2)] \\ &-\bar{a}_4\bar{a}_5\bar{c}_1^2 - \bar{a}_2(\bar{b}_1^2 - \bar{a}_4)(\bar{a}_5\bar{d}_1 - \bar{c}_2^2) \end{aligned} \right\} p^2 \\ &-\bar{a}_1\left[(\bar{\tau}_{33} - \bar{a}_3 + \bar{b}_1\bar{c}_1)^2 - \bar{a}_1(\bar{\tau}_{11} + \bar{\tau}_{33} - 2\bar{a}_3) + (\bar{a}_4 - \bar{b}_1^2)\bar{c}_1^2 + \bar{a}_2(2\bar{b}_1\bar{c}_2 - \bar{a}_4\bar{d}_1 - \bar{a}_5)\right]p^4 + \bar{a}_1^2\bar{a}_2 p^6 = 0. \end{aligned} \tag{B7}$$

In general, six eigenvalues can be obtained from this equation, with corresponding eigenvectors $\bar{\boldsymbol{\eta}}^{(j)}$ given by

$$\bar{\boldsymbol{\eta}}^{(j)} = \begin{bmatrix} p_j\left\{\dfrac{p_j^2\bar{b}_1}{\bar{a}_1} - \dfrac{\bar{a}_1[\bar{b}_1(\bar{a}_3 - \bar{\tau}_{11}) + \bar{a}_4\bar{c}_1]}{\bar{a}_1^2\bar{a}_2} + \dfrac{(\bar{b}_1^2 - \bar{a}_4)(\bar{a}_3\bar{c}_1 - \bar{a}_2\bar{c}_2 - \bar{c}_1\bar{\tau}_{33})}{\bar{a}_1^2\bar{a}_2}\right\} + \dfrac{\bar{a}_4\bar{c}_2}{p_j\bar{a}_1\bar{a}_2} - \dfrac{(\bar{b}_1^2 - \bar{a}_4)(\bar{\tau}_{11} - \bar{\tau}_{33})}{p_j\bar{a}_1^2\bar{a}_2\big/\bar{c}_2} \\ -\left\{p_j^2\dfrac{(\bar{a}_3 - \bar{\tau}_{33})\bar{b}_1 - \bar{a}_4\bar{c}_1}{\bar{a}_1\bar{a}_2} + \dfrac{(\bar{b}_1^2 - \bar{a}_4)[\bar{a}_5\bar{c}_1 - (\bar{a}_3 - \bar{\tau}_{33})\bar{c}_2]}{\bar{a}_1^2\bar{a}_2} + \dfrac{\bar{a}_4\bar{c}_2 - \bar{a}_5\bar{b}_1}{\bar{a}_1\bar{a}_2}\right\} \\ -\dfrac{\bar{a}_4}{\bar{a}_1}p_j^3 + p_j\left\{\dfrac{(\bar{b}_1^2 - \bar{a}_4)[\bar{a}_2\bar{a}_5 - (\bar{a}_3 - \bar{\tau}_{33})^2]}{\bar{a}_1^2\bar{a}_2} + \dfrac{\bar{a}_4(2\bar{a}_3 - \bar{\tau}_{11} - \bar{\tau}_{33})}{\bar{a}_1\bar{a}_2}\right\} + \dfrac{1}{p_j}\left[\dfrac{(\bar{b}_1^2 - \bar{a}_4)\bar{a}_5(\bar{\tau}_{11} - \bar{\tau}_{33})}{\bar{a}_1^2\bar{a}_2} - \dfrac{\bar{a}_4\bar{a}_5}{\bar{a}_1\bar{a}_2}\right] \\ p_j^2\left\{\dfrac{\bar{a}_4\bar{c}_2 - \bar{a}_5\bar{b}_1}{\bar{a}_1} + \dfrac{[(\bar{a}_3 - \bar{\tau}_{33})\bar{b}_1 - \bar{a}_4\bar{c}_1]\bar{a}_3}{\bar{a}_1\bar{a}_2}\right\} + \left\{\left[\bar{a}_4 - (\bar{a}_4 - \bar{b}_1^2)\dfrac{\bar{\tau}_{33}}{\bar{a}_1}\right]\dfrac{\bar{a}_5\bar{c}_1 - \bar{a}_3\bar{c}_2 + \bar{c}_2\bar{\tau}_{33}}{\bar{a}_1\bar{a}_2} + \dfrac{(\bar{a}_4\bar{c}_2 - \bar{a}_5\bar{b}_1)\bar{\tau}_{11}}{\bar{a}_1\bar{a}_2}\right\} \\ \begin{gathered} \left\{\dfrac{\bar{b}_1\bar{\tau}_{33}}{\bar{a}_1}p_j^3 + \dfrac{\bar{a}_5\bar{c}_1 - \bar{a}_3\bar{c}_2}{p_j\bar{a}_1^2\bar{a}_2}\begin{bmatrix} (\bar{b}_1^2 - \bar{a}_4)(\bar{\tau}_{11} - \bar{\tau}_{33}) \\ -\bar{a}_1\bar{a}_4 \end{bmatrix}\right\} - p_j\left\{\dfrac{\bar{c}_1\bar{\tau}_{33}}{\bar{a}_1\bar{a}_2}\left[\bar{a}_4 - (\bar{a}_4 - \bar{b}_1^2)\dfrac{\bar{\tau}_{33} - \bar{a}_3}{\bar{a}_1}\right]\right. \\ \left. +(\bar{a}_3\bar{b}_1 - \bar{a}_4\bar{c}_1)\dfrac{\bar{a}_3 - \bar{\tau}_{11}}{\bar{a}_1\bar{a}_2} + \dfrac{\left[\bar{a}_4 - (\bar{a}_4 - \bar{b}_1^2)\dfrac{\bar{\tau}_{33}}{\bar{a}_1}\right]\bar{c}_2 - \bar{a}_5\bar{b}_1}{\bar{a}_1}\right\} \end{gathered} \\ -\left[p_j^4 + \dfrac{\bar{a}_3 - \bar{\tau}_{11}}{\bar{a}_1\bar{a}_2/(\bar{b}_1\bar{c}_2)} + \dfrac{\bar{a}_1 - \bar{b}_1\bar{c}_1 + \bar{\tau}_{11} - \bar{\tau}_{33}}{\bar{a}_1\bar{a}_2/\bar{a}_5} + p_j^2\dfrac{\bar{a}_3\bar{b}_1\bar{c}_1 - (\bar{a}_3 - \bar{\tau}_{33})^2 + (\bar{a}_1 - \bar{b}_1\bar{c}_1)\bar{\tau}_{33} + \bar{a}_2(\bar{a}_5 - \bar{b}_1\bar{c}_2) - \bar{a}_1(2\bar{a}_3 - \bar{\tau}_{11})}{\bar{a}_1\bar{a}_2}\right] \end{bmatrix} \tag{B8}$$

It should be noted that, for a specific free-energy function of interest, the eigenvalues come in conjugate pairs such that $p_{1,2,3} = \overline{p_{4,5,6}}$

and $\overline{\boldsymbol{\eta}}^{(1,2,3)} = \overline{\overline{\boldsymbol{\eta}}^{(4,5,6)}}$.

B.2. Bifurcation relation

We now consider the incremental interfacial conditions on the top and bottom faces of the block ($x_3 = \pm l_g/2$) given by

$$\dot{T}_{031} = \dot{\tau}^*_{31} - u_{3,1}\tau^*_{11}, \quad \dot{B}_{l03} = u_{1,1}B^*_3 + \dot{B}^*_3, \quad \dot{T}_{033} = \dot{\tau}^*_{33} + u_{1,1}\tau^*_{33}, \quad \dot{H}_{l01} = u_{3,1}H^*_3 + \dot{H}^*_{l01}. \tag{B9}$$

The incremental magnetic field outside the block is also irrotational and can thus be expressed as the gradient of an incremental magnetic scalar potential in the solvent:

$$\dot{\boldsymbol{H}}^* = -\mathrm{grad}\dot{\varphi}^*, \quad \dot{\boldsymbol{B}}^* = -\mu_f \mathrm{grad}\dot{\varphi}^*. \tag{B10}$$

From Eq. (B10), it follows that the incremental magnetic scalar potential $\dot{\varphi}^*$ satisfies $\Delta\dot{\varphi}^* = \mathrm{div}\dot{\boldsymbol{B}}^* = 0$. The explicit form of $\dot{\varphi}^*$ can then be written as

$$\dot{\varphi}^* = k^{-1}\left(C^*_1 e^{kx_3} + C^*_2 e^{-kx_3}\right)e^{ikx_1}, \tag{B11}$$

where C^*_1 and C^*_2 are undetermined constants of integration related to the incremental interfacial and boundary conditions. In the present case, recalling that the top and bottom of the tank are covered by films with perfect diamagnetism and the applied current intensity i_0 is fixed, the incremental magnetic potential at $x_3 = \pm L_t/2$ is assumed to satisfy the decay condition:

$$\dot{\varphi}^*\left(x_1, \ \pm\frac{L_t}{2}\right) = 0. \tag{B12}$$

The associated components of the incremental Maxwell stress can be expressed in terms of $\dot{\varphi}^*$ as

$$\dot{\tau}^*_{11} = \dot{\tau}^*_{22} = -\dot{\tau}^*_{33} = \dot{\varphi}^*_{,3}B^*_3, \qquad \dot{\tau}^*_{13} = \dot{\tau}^*_{31} = -\dot{\varphi}^*_{,1}B^*_3. \tag{B13}$$

Substituting Eq. (B11) into Eqs. (B9) and (B12), and combining with Eq. (B13), we finally arrive at

$$C^*_1 = \frac{i\left[B_3 U_1\left(kl_g/2\right) - \Delta\left(kl_g/2\right)\right]e^{kl_g/2}}{\mu_f\left(e^{kL_t} + e^{kl_g}\right)}, \quad C^*_2 = -\frac{i\left[B_3 U_1\left(kl_g/2\right) - \Delta\left(kl_g/2\right)\right]e^{k\left(2L_t + l_g\right)/2}}{\mu_f\left(e^{kL_t} + e^{kl_g}\right)}, \tag{B14}$$

for the solvent in the region $L_t/2 \leq x_3 \leq l_g/2$, and

$$C^*_1 = \frac{i\left[B_3 U_1\left(-kl_g/2\right) - \Delta\left(-kl_g/2\right)\right]e^{k\left(2L_t + l_g\right)/2}}{\mu_f\left(e^{kl_g} + e^{kL_t}\right)}, \quad C^*_2 = -\frac{i\left[B_3 U_1\left(-kl_g/2\right) - \Delta\left(-kl_g/2\right)\right]e^{kl_g/2}}{\mu_f\left(e^{kl_g} + e^{kL_t}\right)}, \tag{B15}$$

for the solvent in the region $-l_g/2 \geq x_3 \geq -L_t/2$, respectively.

Using Eqs. (6), (B1), (B8)$_2$, and (B9)-(B15), we write the remaining interfacial conditions (B8)$_{1,3,4}$ in impedance matrix form, as

$$\overline{\boldsymbol{S}}(kl_g/2) = i\overline{\boldsymbol{Z}}^*_+\overline{\boldsymbol{U}}(kl_g/2), \quad \overline{\boldsymbol{S}}(-kl_g/2) = i\overline{\boldsymbol{Z}}^*_-\overline{\boldsymbol{U}}(-kl_g/2), \tag{B16}$$

with

$$\overline{\boldsymbol{Z}}^*_+ = \overline{\mu}\begin{bmatrix} \overline{B}^2_3\tanh(k\widetilde{h}/2) & -i\overline{B}^2_3/2 & -\overline{B}_3\tanh(k\widetilde{h}/2) \\ i\overline{B}^2_3/2 & 0 & -i\overline{B}_3 \\ -\overline{B}_3\tanh(k\widetilde{h}/2) & i\overline{B}_3 & \tanh(k\widetilde{h}/2) \end{bmatrix}, \quad \overline{\boldsymbol{Z}}^*_- = \overline{\mu}\begin{bmatrix} -\overline{B}^2_3\tanh(k\widetilde{h}/2) & -i\overline{B}^2_3/2 & \overline{B}_3\tanh(k\widetilde{h}/2) \\ i\overline{B}^2_3/2 & 0 & -i\overline{B}_3 \\ \overline{B}_3\tanh(k\widetilde{h}/2) & i\overline{B}_3 & -\tanh(k\widetilde{h}/2) \end{bmatrix}, \tag{B17}$$

where the short-hand notation is given as $\widetilde{h} = L_t - l_g = L_t - \lambda_3 L_g/\lambda_0$, and the subscripts "±" identify the interfaces $x_3 = \pm l_g/2$, respectively. Rearranging Eq. (B16) using Eq. (B5), we obtain the following matrix form

$$
\begin{bmatrix} \overline{\boldsymbol{S}}(kl_g/2) \\ \overline{\boldsymbol{S}}(-kl_g/2) \end{bmatrix} - \mathrm{i}\begin{bmatrix} \overline{\boldsymbol{Z}}_+^* & 0 \\ 0 & \overline{\boldsymbol{Z}}_-^* \end{bmatrix}\begin{bmatrix} \overline{\boldsymbol{U}}(kl_g/2) \\ \overline{\boldsymbol{U}}(-kl_g/2) \end{bmatrix} = \begin{bmatrix} F_1^+E_1^- & F_2^+E_2^- & F_3^+E_3^- & F_1^-E_1^+ & F_2^-E_2^+ & F_3^-E_3^+ \\ G_1E_1^- & G_2E_2^- & G_3E_3^- & -G_1E_1^+ & -G_2E_2^+ & -G_3E_3^+ \\ H_1^+E_1^- & H_2^+E_2^- & H_3^+E_3^- & H_1^-E_1^+ & H_2^-E_2^+ & H_3^-E_3^+ \\ F_1^-E_1^+ & F_2^-E_2^+ & F_3^-E_3^+ & F_1^+E_1^- & F_2^+E_2^- & F_3^+E_3^- \\ G_1E_1^+ & G_2E_2^+ & G_3E_3^+ & -G_1E_1^- & -G_2E_2^- & -G_3E_3^- \\ H_1^-E_1^+ & H_2^-E_2^+ & H_3^-E_3^+ & H_1^+E_1^- & H_2^+E_2^- & H_3^+E_3^- \end{bmatrix}\begin{bmatrix} h_1 \\ h_2 \\ h_3 \\ h_4 \\ h_5 \\ h_6 \end{bmatrix} = 0, \tag{B18}
$$

where

$$
\begin{aligned}
F_j^{\pm} &= \overline{\mu}\left[\overline{B}_3^2\left(\mp \mathrm{i}\eta_1^{(j)}\tanh(k\widetilde{h}/2) - \frac{1}{2}\eta_2^{(j)}\right) \pm \mathrm{i}\overline{B}_3\eta_3^{(j)}\tanh(k\widetilde{h}/2)\right] + \eta_4^{(j)}, \\
G_j &= \overline{\mu}\overline{B}_3\left(\frac{1}{2}\overline{B}_3\eta_1^{(j)} - \eta_3^{(j)}\right) + \eta_5^{(j)}, \\
H_j^{\pm} &= \overline{\mu}\left[\overline{B}_3\left(\pm \mathrm{i}\eta_1^{(j)}\tanh(k\widetilde{h}/2) + \eta_2^{(j)}\right) \mp \mathrm{i}\eta_3^{(j)}\tanh(k\widetilde{h}/2)\right] + \eta_6^{(j)}.
\end{aligned} \tag{B19}
$$

The bifurcation equation for the antisymmetric and symmetric modes can then be resolved by decoupling Eq. (B18) into two 3 $\times$ 3 blocks with its determinant factorizing as

$$
\begin{vmatrix} P_{11}^{\mathrm{anti}} & P_{12}^{\mathrm{anti}} & P_{13}^{\mathrm{anti}} \\ P_{21}^{\mathrm{anti}} & P_{22}^{\mathrm{anti}} & P_{23}^{\mathrm{anti}} \\ P_{31}^{\mathrm{anti}} & P_{32}^{\mathrm{anti}} & P_{33}^{\mathrm{anti}} \end{vmatrix} \times \begin{vmatrix} P_{11}^{\mathrm{sym}} & P_{12}^{\mathrm{sym}} & P_{13}^{\mathrm{sym}} \\ P_{21}^{\mathrm{sym}} & P_{22}^{\mathrm{sym}} & P_{23}^{\mathrm{sym}} \\ P_{31}^{\mathrm{sym}} & P_{32}^{\mathrm{sym}} & P_{33}^{\mathrm{sym}} \end{vmatrix} = 0, \tag{B20}
$$

where, defining $p_j = \mathrm{i}r_j$,

$$
\begin{aligned}
P_{1j}^{\mathrm{anti}} &= G_j\tanh(kl_gr_j/2), \\
P_{2j}^{\mathrm{anti}} &= \frac{1}{2}\left[F_j^- + F_j^+ + \left(F_j^- - F_j^+\right)\tanh(kl_gr_j/2)\right], \\
P_{3j}^{\mathrm{anti}} &= \frac{1}{2}\left[H_j^- + H_j^+ + \left(H_j^- - H_j^+\right)\tanh(kl_gr_j/2)\right],
\end{aligned} \tag{B21}
$$

$$
\begin{aligned}
P_{1j}^{\mathrm{sym}} &= G_j\coth(kl_gr_j/2), \\
P_{2j}^{\mathrm{sym}} &= \frac{1}{2}\left[F_j^- + F_j^+ + \left(F_j^- - F_j^+\right)\coth(kl_gr_j/2)\right], \\
P_{3j}^{\mathrm{sym}} &= \frac{1}{2}\left[H_j^- + H_j^+ + \left(H_j^- - H_j^+\right)\coth(kl_gr_j/2)\right].
\end{aligned} \tag{B22}
$$

Appendix C. Complementary figures

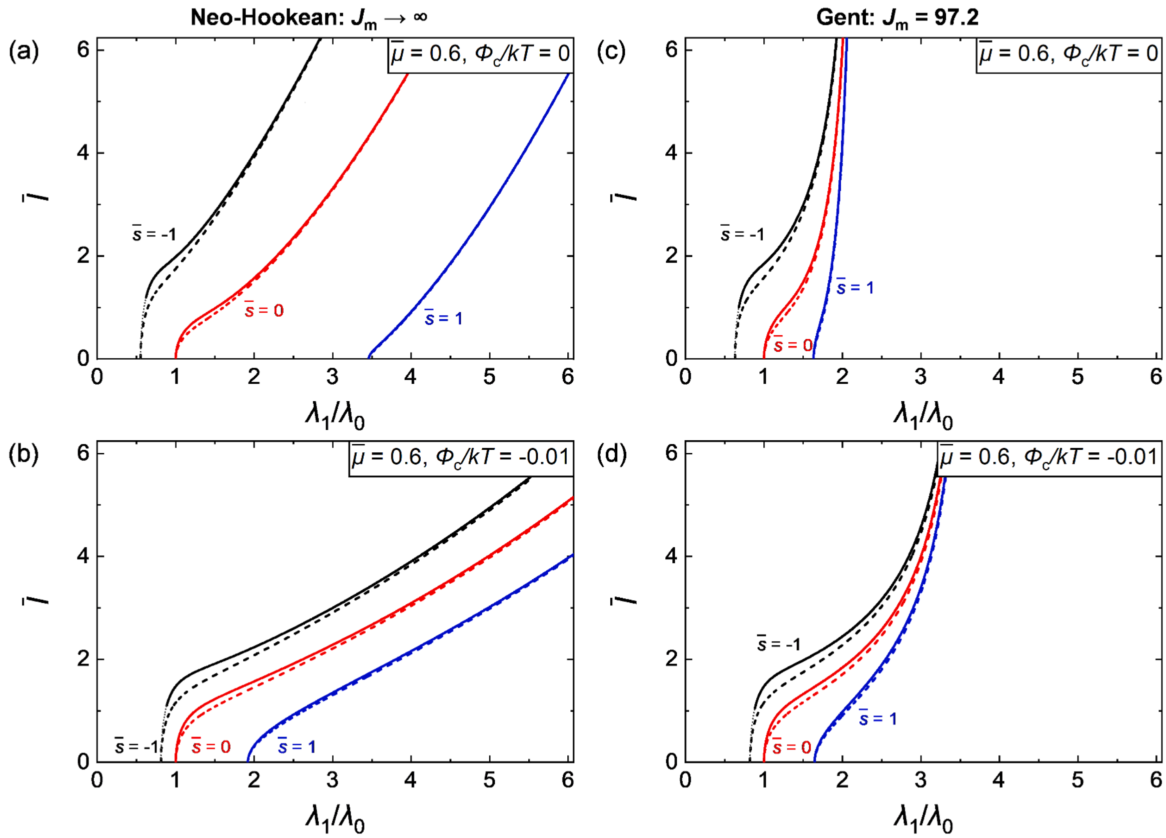

Fig C1. Nonlinear responses of ideal MAH blocks immersed in the solvent with different chemical potentials are analyzed for the normalized permeability $\bar{\mu} = 0.6$. The responses are plotted for $\bar{L} = 0.8$ (solid curves) and $\bar{L} = 0.3$ (dash curves), respectively. (a) $\Phi_c/kT = 0$ and (b) $\Phi_c\ /kT = -0.01$ for the neo-Hookean case; (c) $\Phi_c/kT = 0$ and (d) $\Phi_c/kT = -0.01$ for the Gent ($J_m\ = 97.2$) case. The normalized in-plane normal stress $\bar{s} = 0,\ \pm 1$ correspond to the black, red, and blue curves, respectively. The dotted curves are excluded from the nonlinear responses due to the geometric constraint imposed by the tank ($\lambda_3 \le \lambda_0/\bar{L}$). No pull-in phenomenon is observed in these panels.

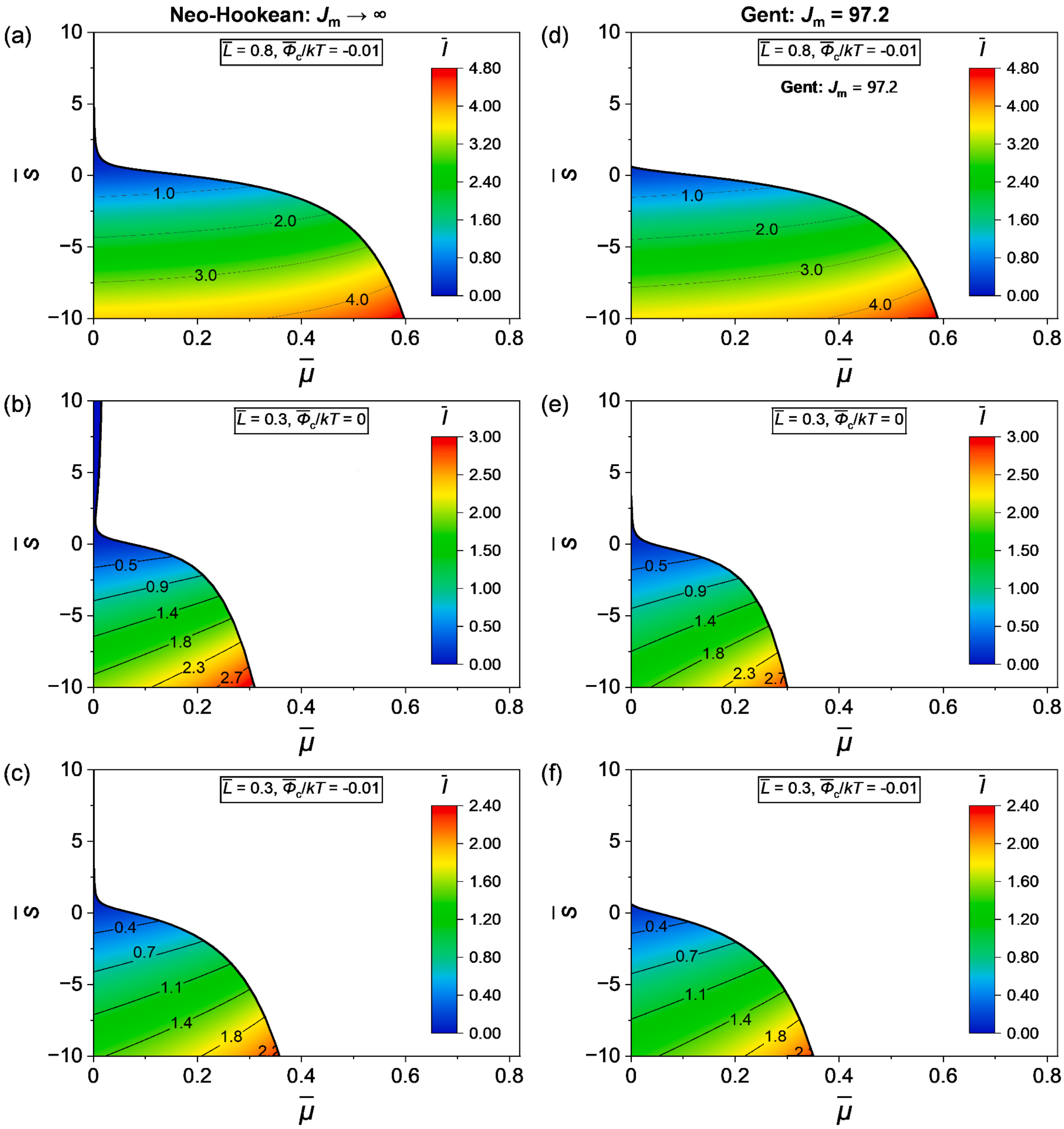

Fig C2. Effect of normalized permeability on the pull-in instability of neo-Hookean and Gent ($J_m = 97.2$) ideal MAH blocks ($\bar{\mu} < 1$) immersed in a solvent. (a) and (d) Contours of critical current for $\bar{L} = 0.8$ and $\Phi_c/kT = -0.01$; (b) and (e) Contours of critical current for $\bar{L} = 0.3$ and $\Phi_c/kT = 0$; (c) and (f) Contours of critical current for $\bar{L} = 0.3$ and $\Phi_c/kT = -0.01$.

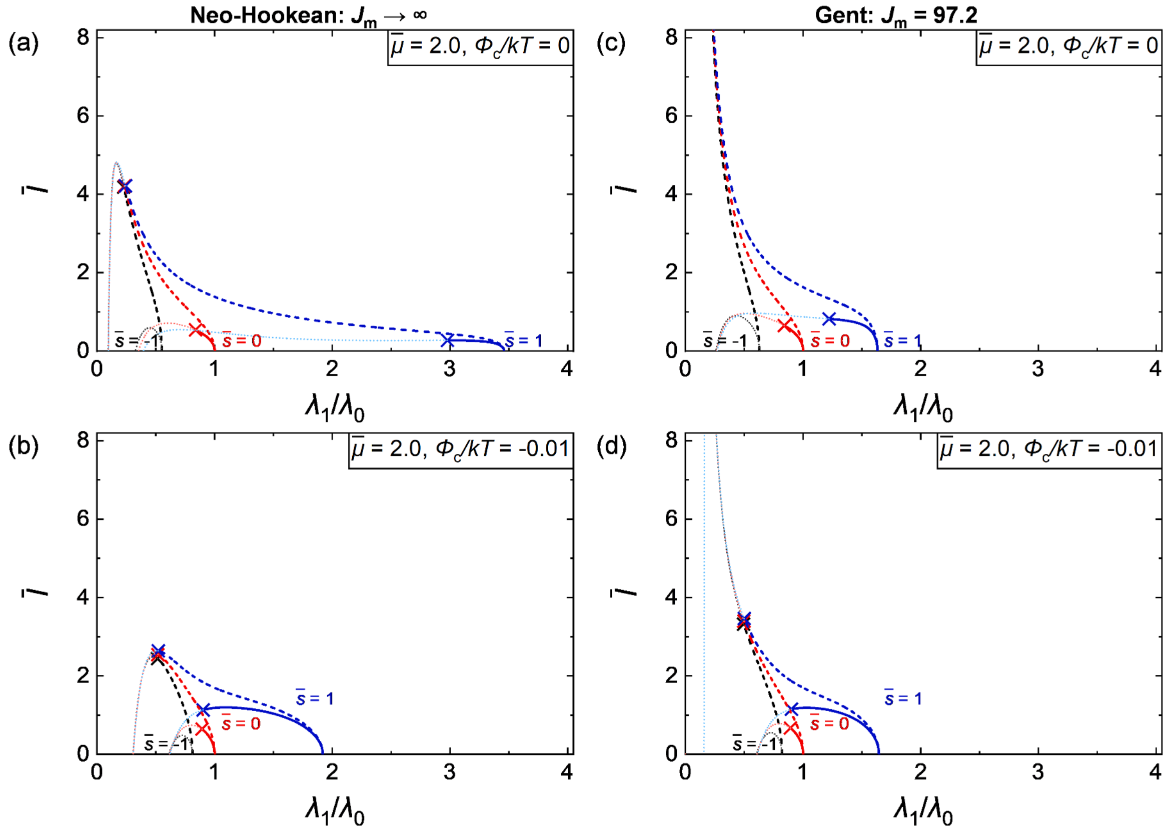

Fig C3. Nonlinear responses of ideal MAH blocks immersed in a solvent with different chemical potentials are analyzed for the normalized permeability $\bar{\mu} = 2.0$. The responses are plotted for $\bar{L} = 0.8$ (solid curves) and $\bar{L} = 0.3$ (dash curves), respectively. (a) $\Phi_c/kT = 0$ and (b) $\Phi_c/kT = -0.01$ for the neo-Hookean case; (c) $\Phi_c/kT = 0$ and (d) $\Phi_c/kT = -0.01$ for the Gent ($J_m = 97.2$) case. The normalized in-plane normal stress $\bar{s} = -1, 0, 1$ correspond to the black, red, and blue curves, respectively. The dotted curves are excluded from the nonlinear responses due to the geometric constraint of the tank ($\lambda_3/\lambda_0 \leq 1/\bar{L}$). No pull-out behavior can be observed in all the panels except for the case of $(\bar{\mu}, \bar{s}, \Phi_c/kT) = (2, 1, -0.01)$.

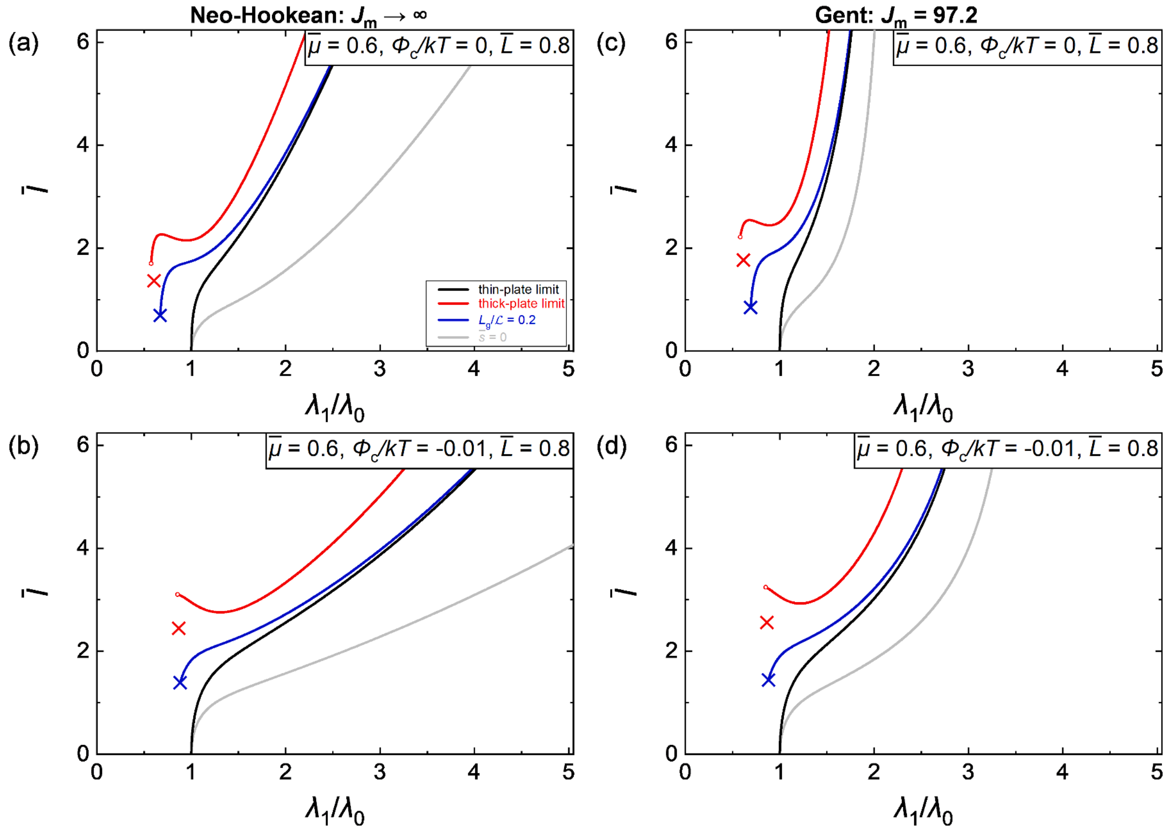

Fig C4. The wrinkling behavior of ideal MAH blocks immersed in a solvent with varying chemical potentials is analyzed for a normalized permeability $\bar{\mu} = 0.6$ and a relative thickness $\bar{L} = 0.8$. (a) $\Phi_c/kT = 0$ and (b) $\Phi_c/kT = -0.01$ for the neo-Hookean case; (c) $\Phi_c/kT = 0$ and (d) $\Phi_c/kT = -0.01$ for the Gent ($J_m = 97.2$) case. The critical curves of $\bar{I}$ versus λ_1/λ_0 for the thin-plate limit, $L_g/\mathscr{L} = 0.2$, and the thick-plate limit, and the nonlinear response for $\bar{s} = 0$ are depicted by black, blue, red, and gray lines, respectively. All curves satisfy the geometric constraint of the tank ($\lambda_3 \le \lambda_0/\bar{L}$), with the case of $\lambda_3 = \lambda_0/\bar{L}$ marked by crosses.

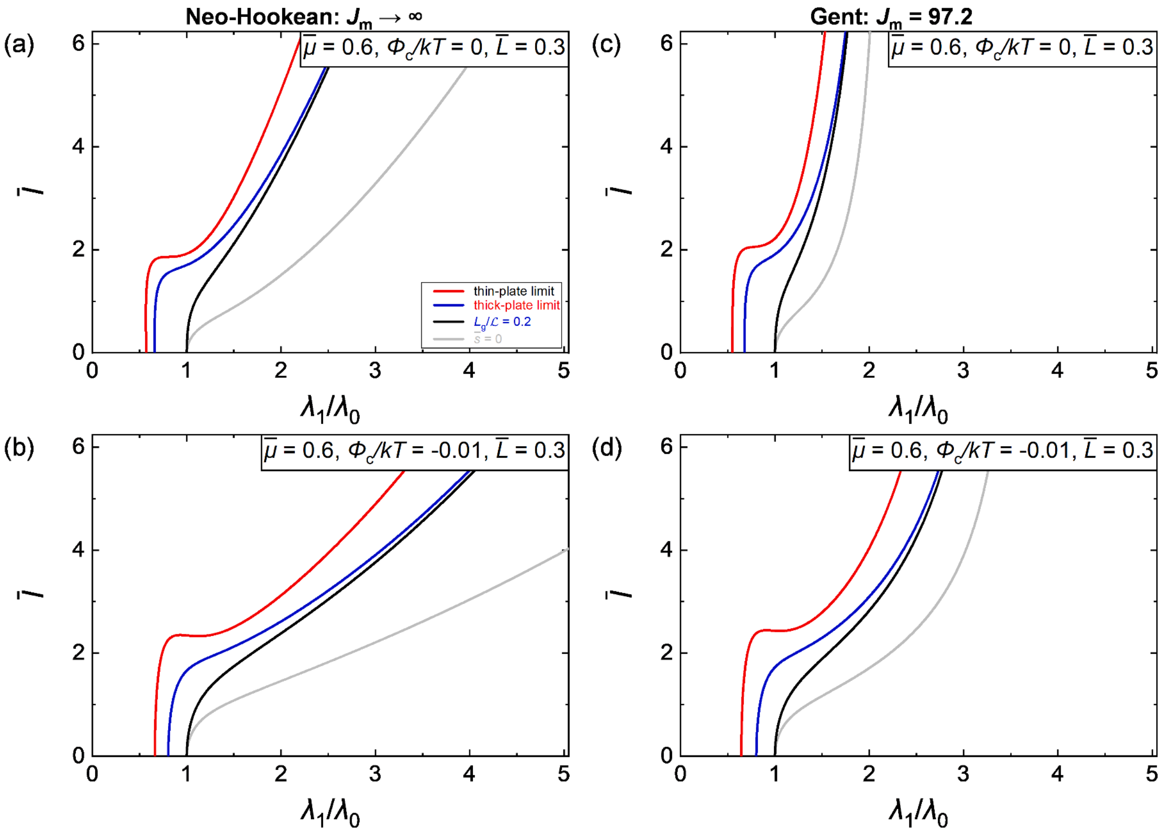

Fig C5. The wrinkling behavior of ideal MAH blocks immersed in a solvent with varying chemical potentials is analyzed for a normalized permeability $\bar{\mu} = 0.6$ and a relative thickness $\bar{L} = 0.3$. (a) $\Phi_c/kT = 0$ and (b) $\Phi_c/kT = -0.01$ for the neo-Hookean case; (c) $\Phi_c/kT = 0$ and (d) $\Phi_c/kT = -0.01$ for the Gent ($J_m = 97.2$) case. The critical curves of $\bar{I}$ versus λ_1/λ_0 for the thin-plate limit, $L_g/\mathscr{L} = 0.2$, and the thick-plate limit, and the nonlinear response for $\bar{s} = 0$ are depicted by black, blue, red, and gray lines, respectively.

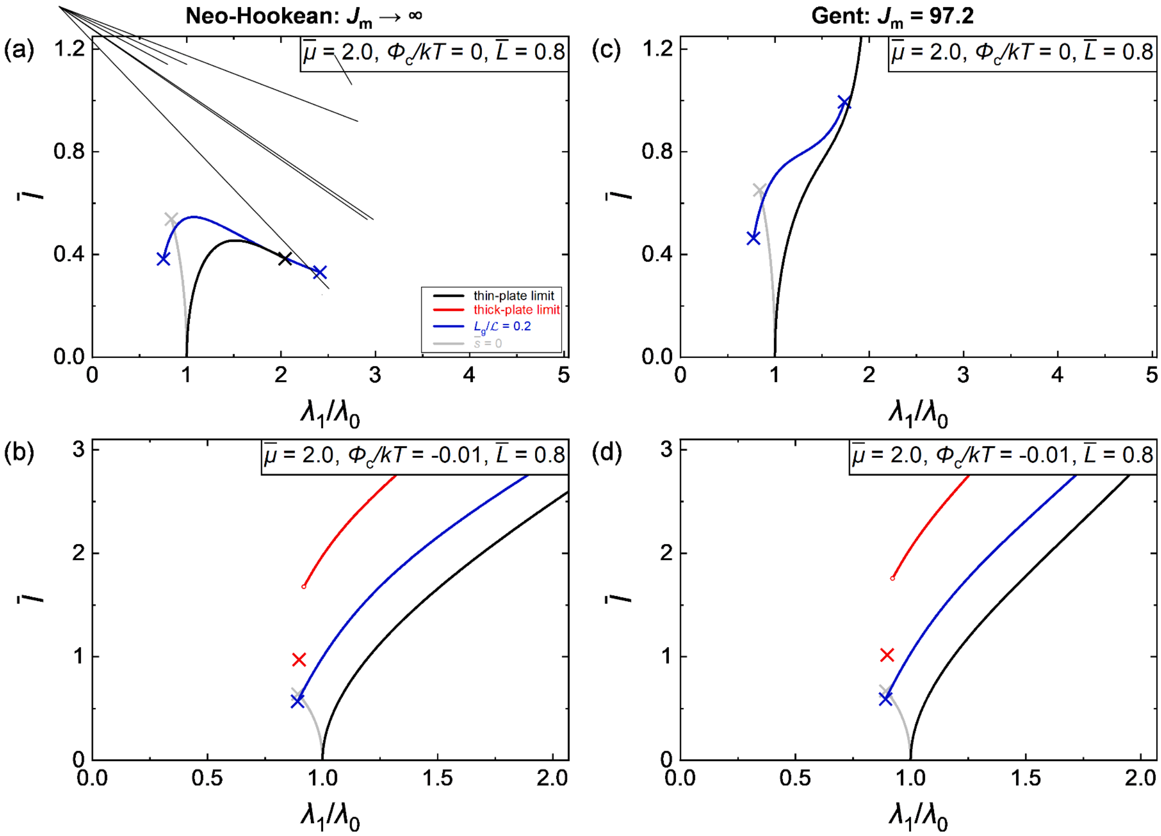

Fig C6. The wrinkling behavior of ideal MAH blocks immersed in a solvent with varying chemical potentials is analyzed for a normalized permeability $\bar{\mu} = 2.0$ and a relative thickness $\bar{L} = 0.8$. (a) $\Phi_c/kT = 0$ and (b) $\Phi_c/kT = -0.01$ for the neo-Hookean case; (c) $\Phi_c/kT = 0$ and (d) $\Phi_c/kT = -0.01$ for the Gent ($J_m = 97.2$) case. The critical curves of $\bar{I}$ versus λ_1/λ_0 for the thin-plate limit, $L_g/\mathscr{L} = 0.2$, and the thick-plate limit, and the nonlinear response for $\bar{s} = 0$ are depicted by black, blue, red, and gray lines, respectively. All curves satisfy the geometric constraint of the tank ($\lambda_3 \le \lambda_0/\bar{L}$), with the case of $\lambda_3 = \lambda_0/\bar{L}$ marked by crosses.

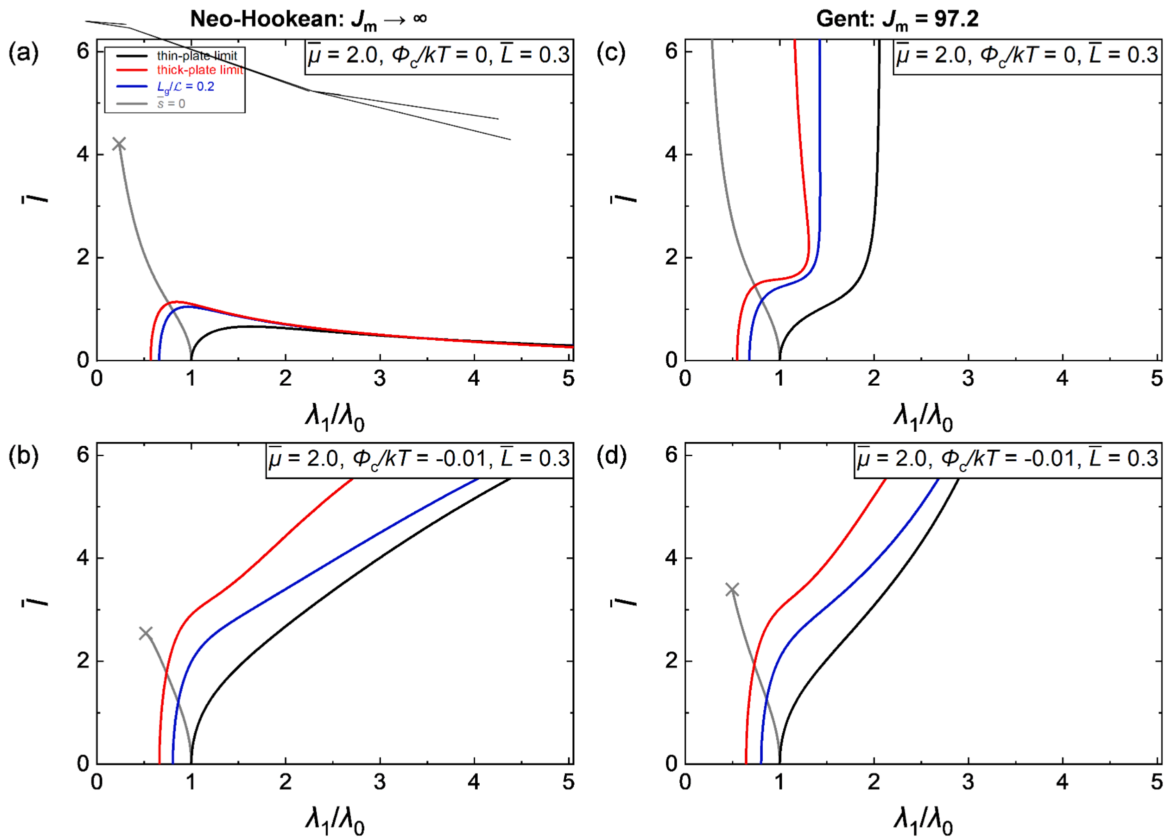

Fig C7. The wrinkling behavior of ideal MAH blocks immersed in a solvent with varying chemical potentials is analyzed for a normalized permeability $\overline{\mu} = 2.0$ and a relative thickness $\overline{L} = 0.3$. (a) $\Phi_c/kT = 0$ and (b) $\Phi_c/kT = -0.01$ for the neo-Hookean case; (c) $\Phi_c/kT = 0$ and (d) $\Phi_c/kT = -0.01$ for the Gent ($J_m = 97.2$) case. The critical curves of $\overline{I}$ versus λ_1/λ_0 for the thin-plate limit, $L_g/\mathscr{L} = 0.2$, and the thick-plate limit, and the nonlinear response for $\bar{s} = 0$ are depicted by black, blue, red, and gray lines, respectively. All curves satisfy the geometric constraint of the tank ($\lambda_3 \leq \lambda_0/\bar{L}$), with the case of $\lambda_3 = \lambda_0/\bar{L}$ marked by crosses.

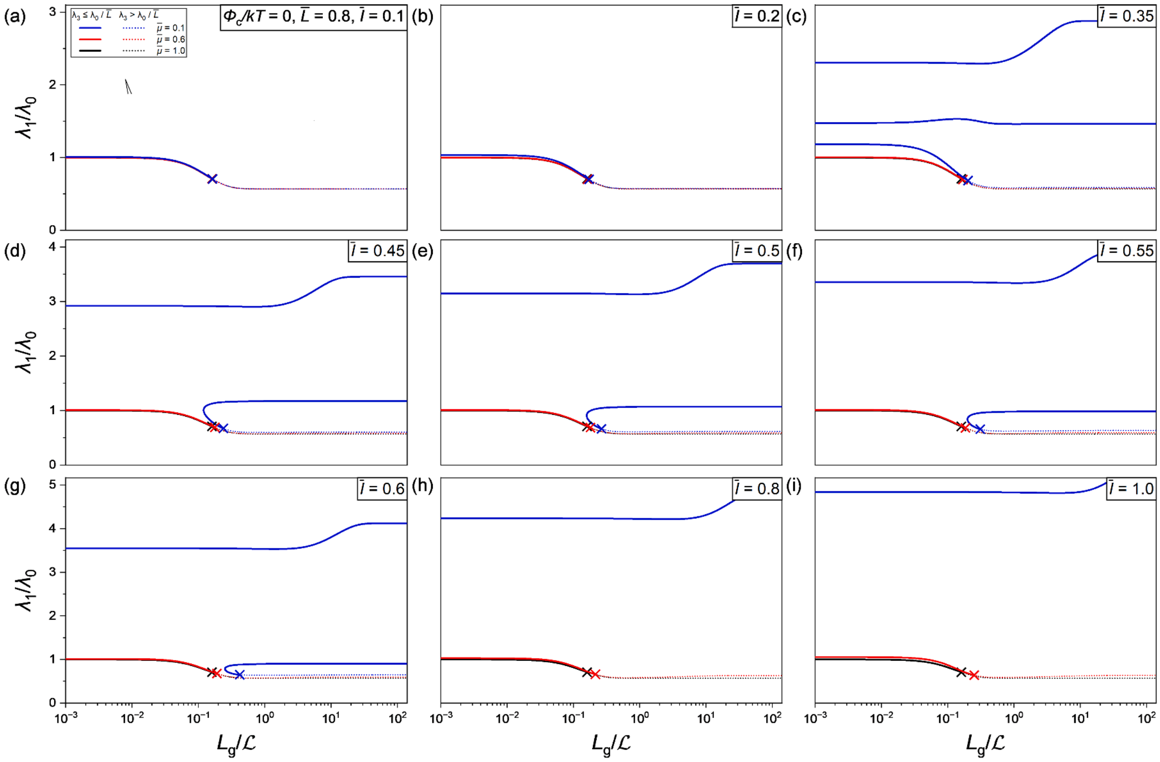

Fig C8. The critical curves of λ_1/λ_0 versus $L_g/\mathscr{L}$ are shown for ideal MAH blocks with diverse permeabilities ($\bar{\mu} \leq 1$) immersed in a solvent with $\Phi_c/kT = 0$ and $\bar{L} = 0.8$. Panels (a)-(i) correspond to the neo-Hookean case with $\bar{l} = 0.1,\ 0.2,\ 0.35,\ 0.45,\ 0.5,\ 0.55,\ 0.6,\ 0.8,\ 1.0$, respectively. The blue, red, and black curves represent antisymmetric wrinkling for blocks with $\bar{\mu} = 0.1,\ 0.6,\ 1.0$, respectively, satisfying the geometric constraint of the tank ($\lambda_3 \leq \lambda_0/\overline{L}$). Crosses mark the case where $\lambda_3 = \lambda_0/\overline{L}$. The dotted curves are excluded from the critical curves due to the geometric constraint of the tank ($\lambda_3 \leq \lambda_0/\overline{L}$).

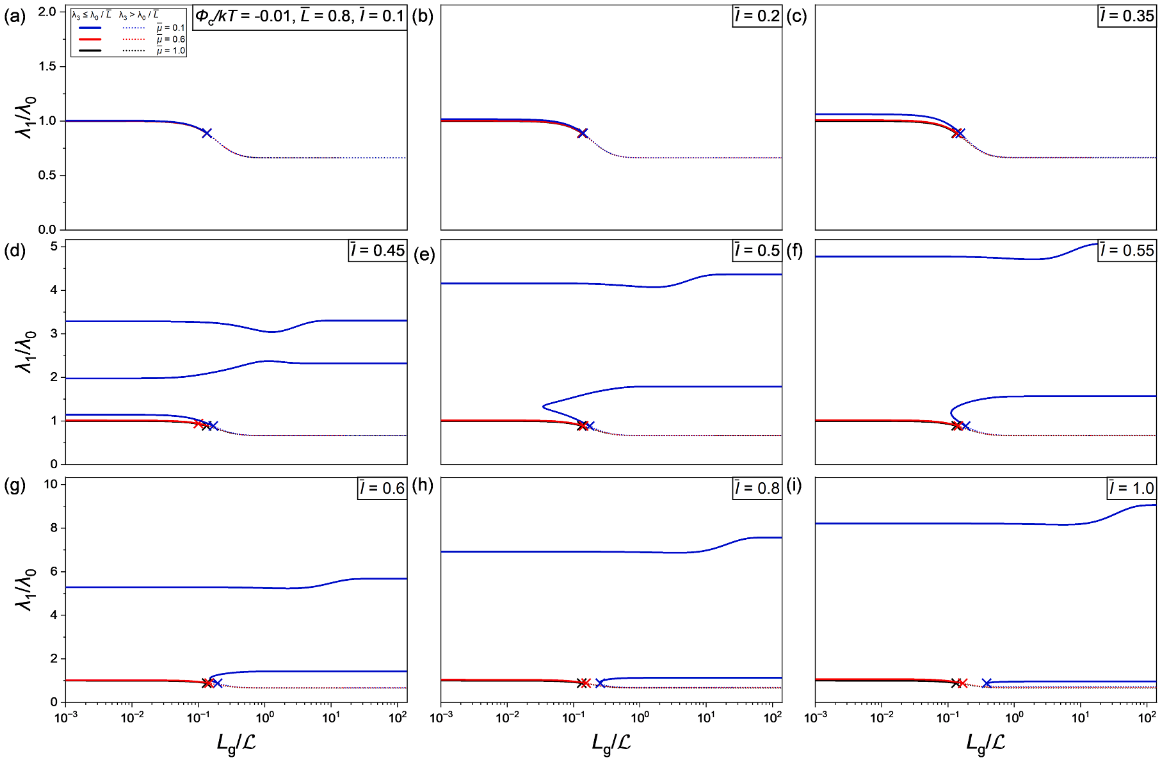

Fig C9. The critical curves of λ_1/λ_0 versus $L_g/\mathscr{L}$ are shown for ideal MAH blocks with diverse permeabilities ($\overline{\mu} \leq 1$) immersed in a solvent with $\Phi_c/kT = -0.01$ and $\overline{L} = 0.8$. Panels (a)-(i) correspond to the neo-Hookean case with $\overline{l} = 0.1,\ 0.2,\ 0.35,\ 0.45,\ 0.5,\ 0.55,\ 0.6,\ 0.8,\ 1.0$, respectively. The blue, red, and black curves represent antisymmetric wrinkling for blocks with $\overline{\mu} = 0.1,\ 0.6,\ 1.0$, respectively, satisfying the geometric constraint of the tank ($\lambda_3 \leq \lambda_0/\overline{L}$). Crosses mark the case where $\lambda_3 = \lambda_0/\overline{L}$. The dotted curves are excluded from the critical curves due to the geometric constraint of the tank ($\lambda_3 \leq \lambda_0/\overline{L}$).

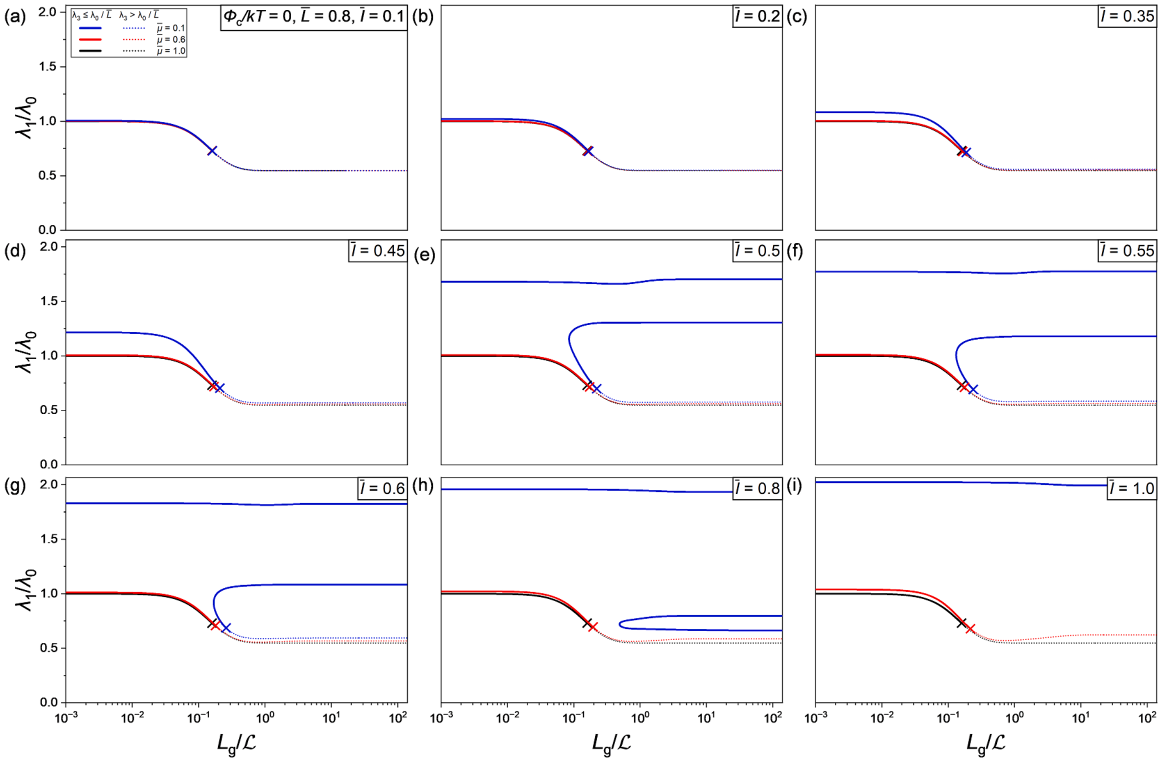

Fig C10. The critical curves of λ_1/λ_0 versus $L_g/\mathscr{L}$ are shown for ideal MAH blocks with diverse permeabilities ($\bar{\mu} \le 1$) immersed in a solvent with $\Phi_c/kT = 0$ and $\bar{L} = 0.8$. Panels (a)-(i) correspond to the Gent ($J_m = 97.2$) case with $\bar{l} = 0.1,\ 0.2,\ 0.35,\ 0.45,\ 0.5,\ 0.55,\ 0.6,\ 0.8,\ 1.0$, respectively. The blue, red, and black curves represent antisymmetric wrinkling for blocks with $\bar{\mu} = 0.1,\ 0.6,\ 1.0$, respectively, satisfying the geometric constraint of the tank ($\lambda_3 \le \lambda_0/\bar{L}$). Crosses mark the case where $\lambda_3 = \lambda_0/\bar{L}$. The dotted curves are excluded from the critical curves due to the geometric constraint of the tank ($\lambda_3 \le \lambda_0/\bar{L}$).

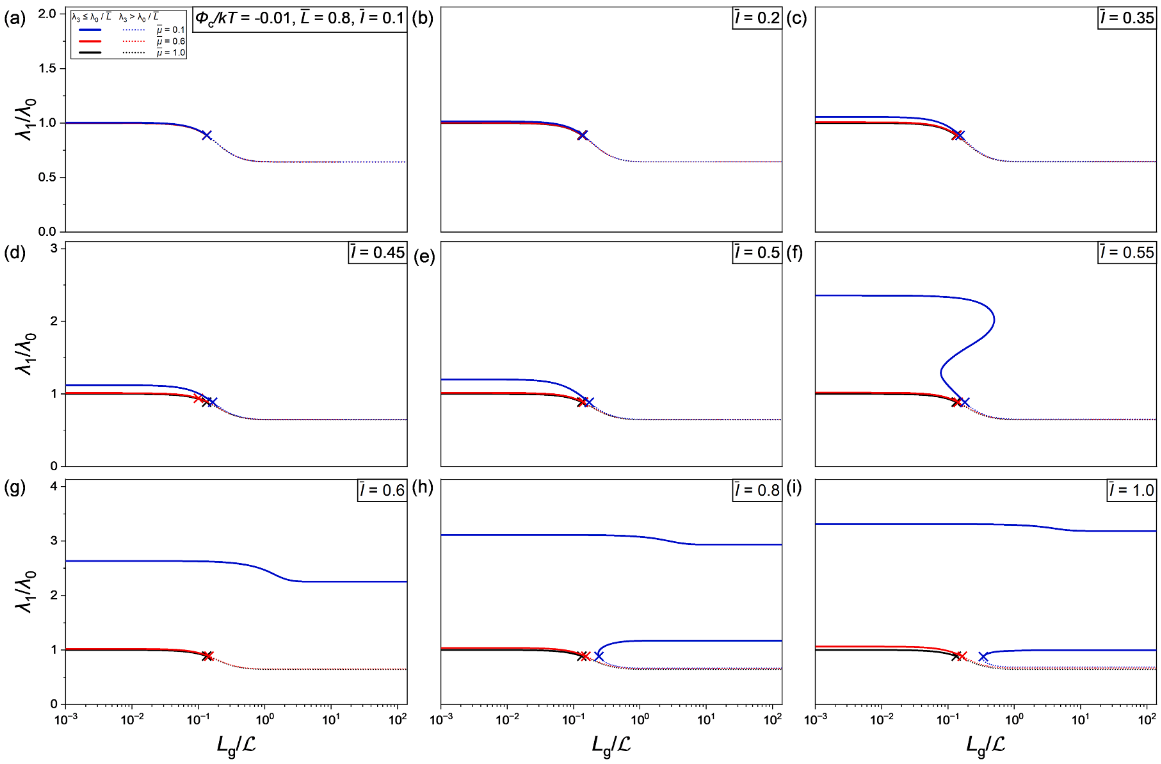

Fig C11. The critical curves of λ_1/λ_0 versus $L_g/\mathscr{L}$ are shown for ideal MAH blocks with diverse permeabilities ($\overline{\mu} \leq 1$) immersed in a solvent with $\Phi_c/kT = -0.01$ and $\overline{L} = 0.8$. Panels (a)-(i) correspond to the Gent ($J_m = 97.2$) case with $\overline{l} = 0.1,\ 0.2,\ 0.35,\ 0.45,\ 0.5,\ 0.55,\ 0.6,\ 0.8,\ 1.0$, respectively. The blue, red, and black curves represent antisymmetric wrinkling for blocks with $\overline{\mu} = 0.1,\ 0.6,\ 1.0$, respectively, satisfying the geometric constraint of the tank ($\lambda_3 \leq \lambda_0/\overline{L}$). Crosses mark the case where $\lambda_3 = \lambda_0/\overline{L}$. The dotted curves are excluded from the critical curves due to the geometric constraint of the tank ($\lambda_3 \leq \lambda_0/\overline{L}$).

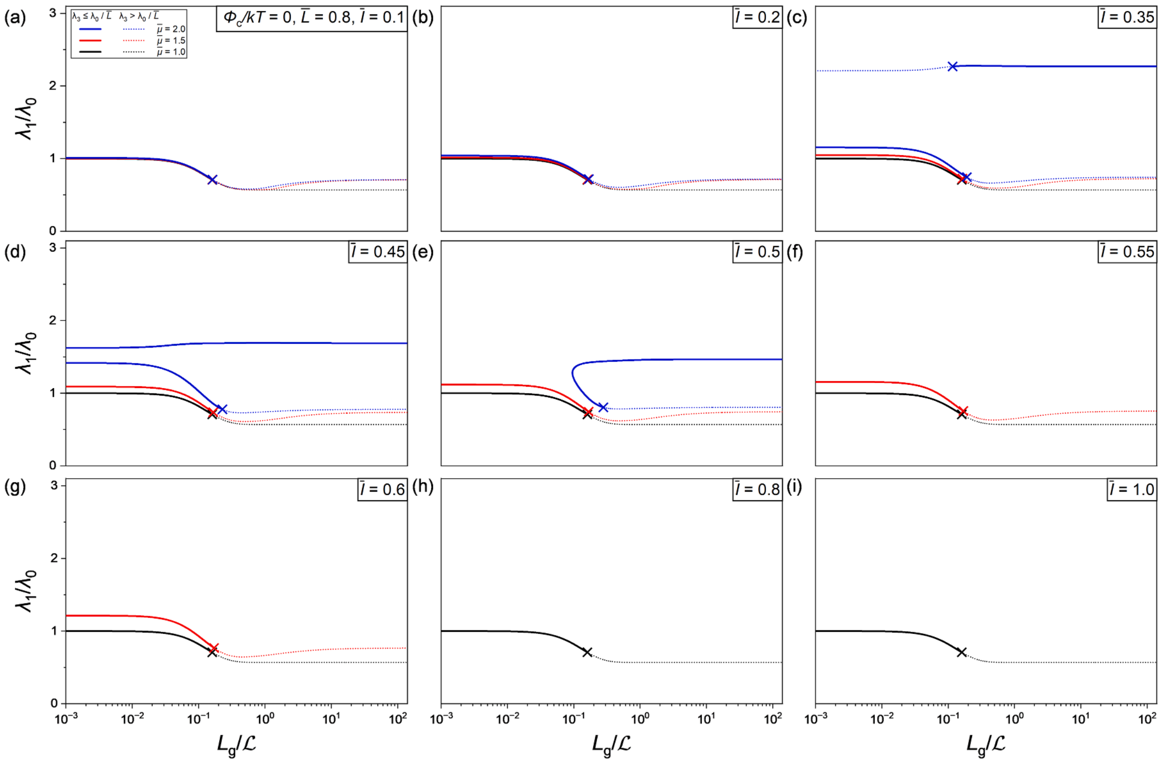

Fig C12. The critical curves of λ_1/λ_0 versus $L_g/\mathscr{L}$ are shown for ideal MAH blocks with diverse permeabilities ($\overline{\mu} \le 1$) immersed in a solvent with $\Phi_c/kT = 0$ and $\overline{L} = 0.8$. Panels (a)-(i) correspond to the neo-Hookean case with $\overline{l} = 0.1,\ 0.2,\ 0.35,\ 0.45,\ 0.5,\ 0.55,\ 0.6,\ 0.8,\ 1.0$, respectively. The blue, red, and black curves represent antisymmetric wrinkling for blocks with $\overline{\mu} = 2.0, 1.5,\ 1.0$, respectively, satisfying the geometric constraint of the tank ($\lambda_3 \le \lambda_0/\overline{L}$). Crosses mark the case where $\lambda_3 = \lambda_0/\overline{L}$. The dotted curves are excluded from the critical curves due to the geometric constraint of the tank ($\lambda_3 \le \lambda_0/\overline{L}$).

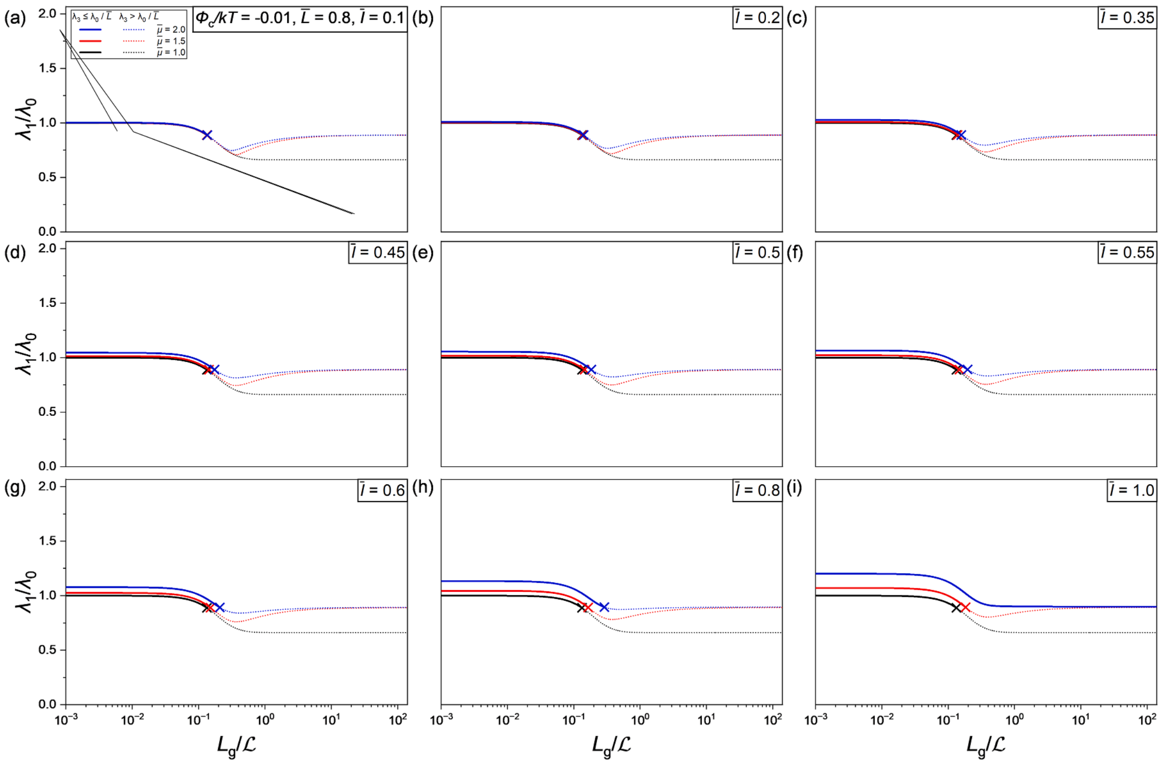

Fig C13. The critical curves of λ_1/λ_0 versus $L_g/\mathscr{L}$ are shown for ideal MAH blocks with diverse permeabilities ($\overline{\mu} \le 1$) immersed in a solvent with $\Phi_c/kT = -0.01$ and $\overline{L} = 0.8$. Panels (a)-(i) correspond to the neo-Hookean case with $\overline{I} = 0.1, 0.2, 0.35, 0.45, 0.5, 0.55, 0.6, 0.8, 1.0$, respectively. The blue, red, and black curves represent antisymmetric wrinkling for blocks with $\overline{\mu} = 2.0, 1.5, 1.0$, respectively, satisfying the geometric constraint of the tank ($\lambda_3 \le \lambda_0/\overline{L}$). Crosses mark the case where $\lambda_3 = \lambda_0/\overline{L}$. The dotted curves are excluded from the critical curves due to the geometric constraint of the tank ($\lambda_3 \le \lambda_0/\overline{L}$).

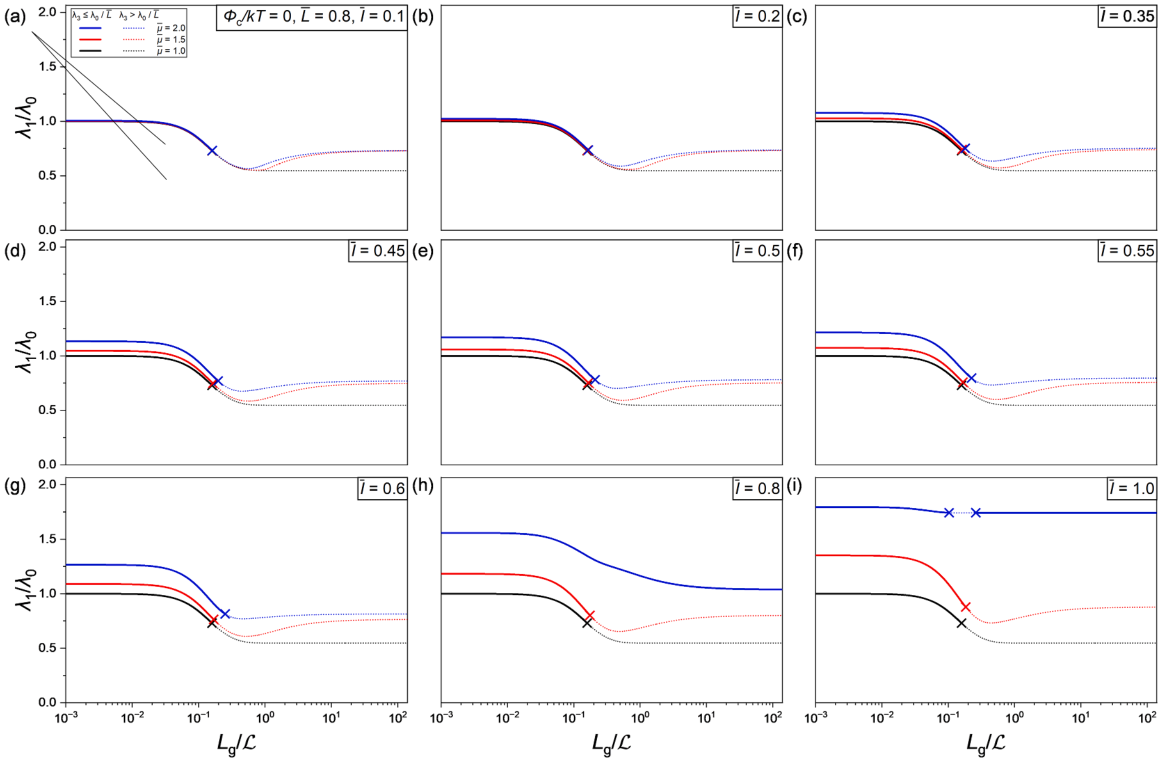

Fig C14. The critical curves of λ_1/λ_0 versus $L_g/\mathscr{L}$ are shown for ideal MAH blocks with diverse permeabilities ($\bar{\mu} \le 1$) immersed in a solvent with $\Phi_c/kT = 0$ and $\bar{L} = 0.8$. Panels (a)-(i) correspond to the Gent ($J_m = 97.2$) case with $\bar{l} = 0.1,\ 0.2,\ 0.35,\ 0.45,\ 0.5,\ 0.55,\ 0.6,\ 0.8,\ 1.0$, respectively. The blue, red, and black curves represent antisymmetric wrinkling for blocks with $\bar{\mu} = 2.0, 1.5,\ 1.0$, respectively, satisfying the geometric constraint of the tank ($\lambda_3 \le \lambda_0/\bar{L}$). Crosses mark the case where $\lambda_3 = \lambda_0/\bar{L}$. The dotted curves are excluded from the critical curves due to the geometric constraint of the tank ($\lambda_3 \le \lambda_0/\bar{L}$).

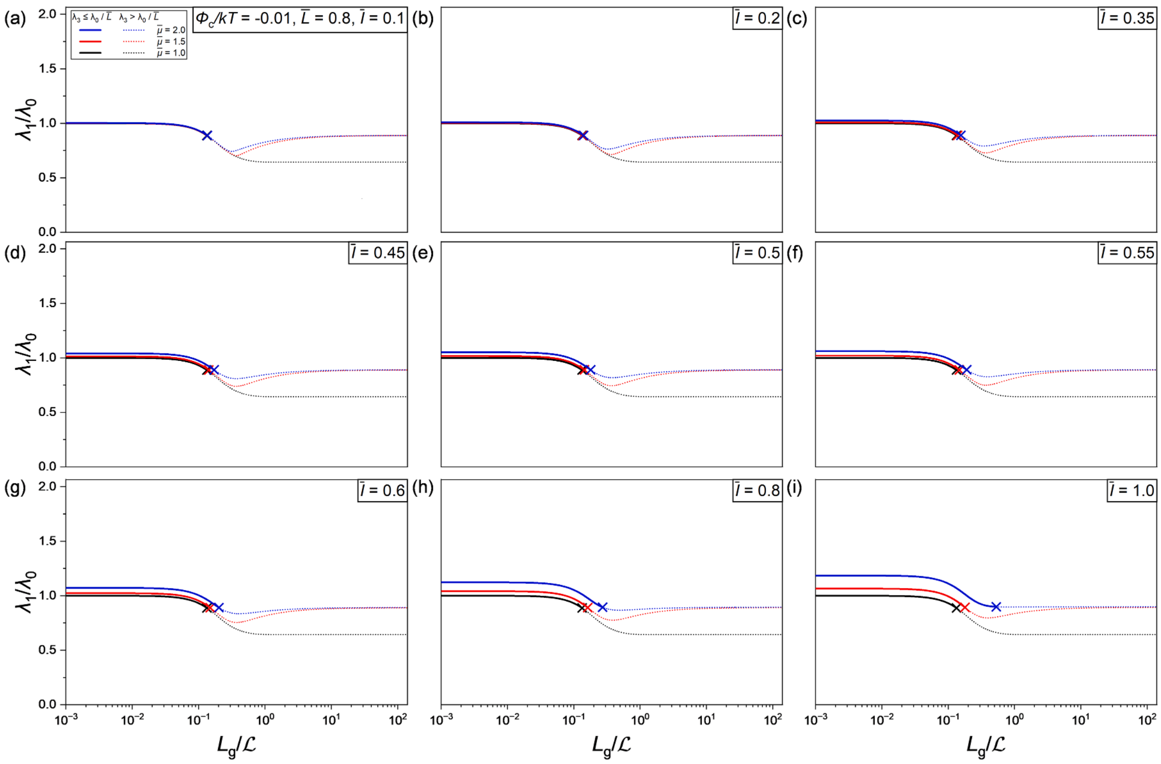

Fig C15. The critical curves of λ_1/λ_0 versus $L_g/\mathscr{L}$ are shown for ideal MAH blocks with diverse permeabilities ($\overline{\mu} \le 1$) immersed in a solvent with $\Phi_c/kT = -0.01$ and $\overline{L} = 0.8$. Panels (a)-(i) correspond to the Gent ($J_m = 97.2$) case with $\overline{I} = 0.1,\ 0.2,\ 0.35,\ 0.45,\ 0.5,\ 0.55,\ 0.6,\ 0.8,\ 1.0$, respectively. The blue, red, and black curves represent antisymmetric wrinkling for blocks with $\overline{\mu} = 2.0, 1.5,\ 1.0$, respectively, satisfying the geometric constraint of the tank ($\lambda_3 \le \lambda_0/\overline{L}$). Crosses mark the case where $\lambda_3 = \lambda_0/\overline{L}$. The dotted curves are excluded from the critical curves due to the geometric constraint of the tank ($\lambda_3 \le \lambda_0/\overline{L}$).

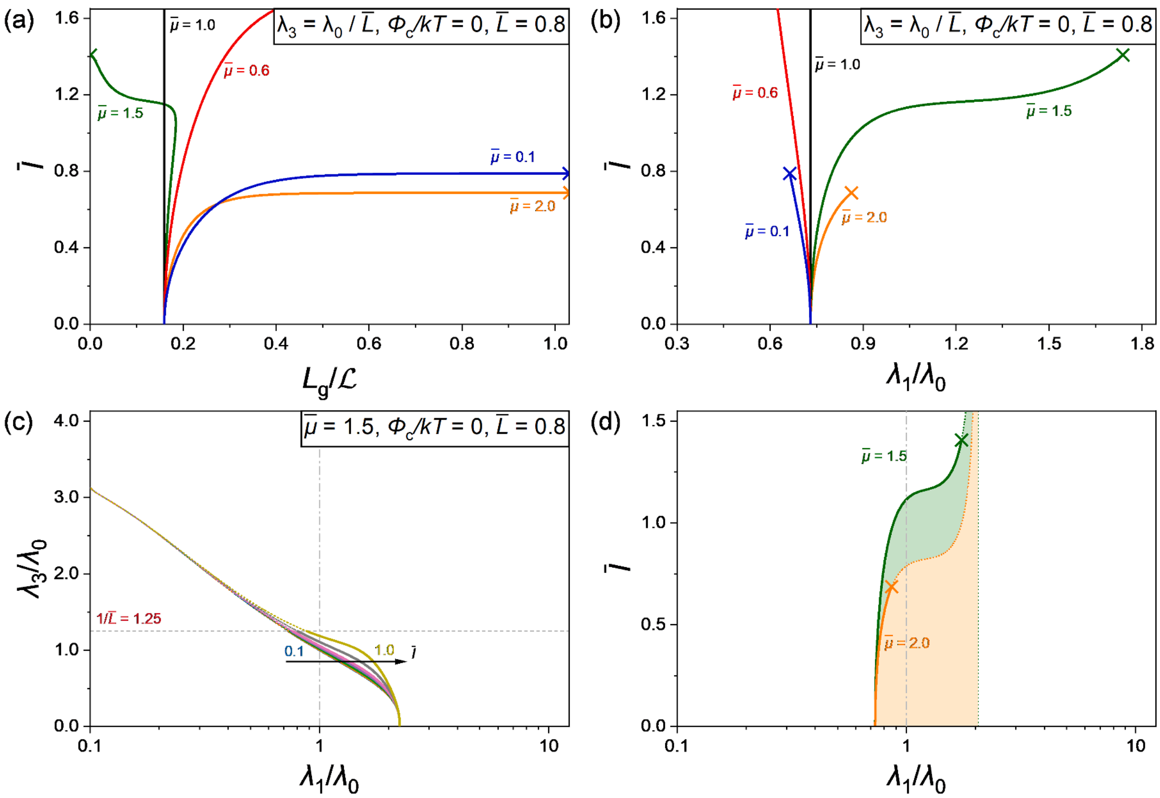

Fig C16. Encounter of critical touching between the immersed Gent ($J_m = 97.2$) ideal MAH block during wrinkling and the tank with $\Phi_c / kT = 0$ and $\bar{L} = 0.8$. (a) Critical curves of $\bar{I}$ versus $L_g/\mathscr{L}$ for $\lambda_3 = \lambda_0/\bar{L}$ and $\bar{\mu} = 0.1, 0.6, 1.0, 1.5$ and 2.0; (b) Critical curves of $\bar{I}$ versus λ_1/λ_0 for $\lambda_3 = \lambda_0/\bar{L}$ and $\bar{\mu} = 0.1, 0.6, 1.0, 1.5$ and 2.0; (c) Nonlinear responses under diverse currents $\bar{I} = 0.1, 0.2, 0.35, 0.5, 0.6, 0.8, 1.0$ and $\bar{\mu} = 1.5$; (d) Combination of enlarged critical curves of $\bar{I}$ versus λ_1/λ_0 for $\lambda_3 = \lambda_0/\bar{L}$ and nonlinear responses of the MAH blocks with $\bar{\mu} = 1.5$ and 2.0, respectively. The dotted curves are excluded from the nonlinear responses due to the geometric constraint of the tank ($\lambda_3 \le \lambda_0/\bar{L}$).

Data availability

No data was used for the research described in the article.

References

Ahmadinejad, M., Marshall, J.S., 2024. Magnetic nanoparticle interaction with a hydrogel in an oscillating magnetic field. Phys. Fluids 36 (1).

Alapan, Y., Karacakol, A.C., Guzelhan, S.N., Isik, I., Sitti, M., 2020. Reprogrammable shape morphing of magnetic soft machines. Sci. Adv. 6 (38), eabc6414.

Biot, M.A., 1963. Surface instability of rubber in compression. Applied Scientific Research, Section A 12 (2), 168–182.

Chen, Y., Zhang, Y., Li, H., Shen, J., Zhang, F., He, J., Lin, J., Wang, B., Niu, S., Han, Z., Guo, Z., 2023. Bioinspired hydrogel actuator for soft robotics: Opportunity and challenges. Nano Today 49, 101764.

Chen, Z., Zhao, D., Liu, B., Nian, G., Li, X., Yin, J., Qu, S., Yang, W., 2019. 3D Printing of Multifunctional Hydrogels. Adv. Funct. Mater. 29 (20), 1900971.

Dorfmann, L., Ogden, R.W., 2014. Nonlinear theory of electroelastic and magnetoelastic interactions, XI. Springer, New York, p. 313.

Flory, P.J., 1942. Thermodynamics of High Polymer Solutions. J. Chem. Phys. 10 (1), 51–61.

Flory, P.J., 1953. Principles of polymer chemistry. Cornell university press, Ithaca, NY.

Galli, M., Comley, K.S.C., 2009. Viscoelastic and poroelastic mechanical characterization of hydrated gels. J. Mater. Res. 24 (3), 973–979.

Garcia-Gonzalez, D., Landis, C.M., 2020. Magneto-diffusion-viscohyperelasticity for magneto-active hydrogels: Rate dependences across time scales. J. Mech. Phys. Solids 139, 103934.

Gebhart, P., Wallmersperger, T., 2019. A general framework for the modeling of porous ferrogels at finite strains. J. Mech. Phys. Solids 122, 69–83.

Gonzalez-Rico, J., Garzon-Hernandez, S., Landis, C.M., Garcia-Gonzalez, D., 2024. Magneto-mechanically derived diffusion processes in ultra-soft biological hydrogels. J. Mech. Phys. Solids 192, 105791.

Gonzalez-Saiz, E., Lopez-Donaire, M.L., Gutiérrez, L., Danas, K., Garcia-Gonzalez, D., 2025. Magnetic-Driven Viscous Mechanisms in Ultra-Soft Magnetorheological Elastomers Offer History-Dependent Actuation with Reprogrammability Options. Adv. Sci. 12 (35), e06790.

Goshkoderia, A., Chen, V., Li, J., Juhl, A., Buskohl, P., Rudykh, S., 2020. Instability-Induced Pattern Formations in Soft Magnetoactive Composites. Phys. Rev. Lett. 124 (15), 158002.

Holzapfel, G.A., 2000. Nonlinear Solid Mechanics, A Continuum Approach for Engineering. John Wiley & Sons, West Sussex, England.

Hong, W., Liu, Z., Suo, Z., 2009. Inhomogeneous swelling of a gel in equilibrium with a solvent and mechanical load. Int. J. Solids Struct. 46 (17), 3282–3289.

Hong, W., Zhao, X., Zhou, J., Suo, Z., 2008. A theory of coupled diffusion and large deformation in polymeric gels. J. Mech. Phys. Solids 56 (5), 1779–1793.

Hou, X., Liu, Y., Wan, G., Xu, Z., Wen, C., Yu, H., Zhang, J.X.J., Li, J., Chen, Z., 2018. Magneto-sensitive bistable soft actuators: Experiments, simulations, and applications. Appl. Phys. Lett. 113 (22).
Hu, W., Lum, G.Z., Mastrangeli, M., Sitti, M., 2018. Small-scale soft-bodied robot with multimodal locomotion. Nature 554 (7690), 81–85.
Huang, H.-W., Sakar, M.S., Petruska, A.J., Pané, S., Nelson, B.J., 2016. Soft micromachines with programmable motility and morphology. Nat. Commun. 7 (1), 12263.
Huggins, M.L., 1941. Solutions of Long Chain Compounds. J. Chem. Phys. 9 (5), 440.
Jahanban-Esfahlan, R., Derakhshankhah, H., Haghshenas, B., Massoumi, B., Abbasian, M., Jaymand, M., 2020. A bio-inspired magnetic natural hydrogel containing gelatin and alginate as a drug delivery system for cancer chemotherapy. Int. J. Biol. Macromol. 156, 438–445.
Kaufman, J.D., Miller, G.J., Morgan, E.F., Klapperich, C.M., 2008. Time-dependent mechanical characterization of poly(2-hydroxyethyl methacrylate) hydrogels using nanoindentation and unconfined compression. J. Mater. Res. 23 (5), 1472–1481.
Khan, M.A., Mujahid, M., Loo, S.C.J., Chamundeswari, V.N., 2020. Nanophotonics based label free detection mechanism for real-time monitoring of interleukin-6. Nanoscale 12 (16), 9194–9207.
Li, J., Mooney, D.J., 2016. Designing hydrogels for controlled drug delivery. Nat. Rev. Mater. 1 (12), 16071.
Li, Y., Huang, G., Zhang, X., Li, B., Chen, Y., Lu, T., Lu, T.J., Xu, F., 2013. Magnetic Hydrogels and Their Potential Biomedical Applications. Adv. Funct. Mater. 23 (6), 660–672.
Liu, K., VanLandingham, M.R., Ovaert, T.C., 2009. Mechanical characterization of soft viscoelastic gels via indentation and optimization-based inverse finite element analysis. J. Mech. Behav. Biomed. Mater. 2 (4), 355–363.
Liu, Q., Li, H., Lam, K.Y., 2017. Development of a Multiphysics Model to Characterize the Responsive Behavior of Magnetic-Sensitive Hydrogels with Finite Deformation. J. Phys. Chem. B 121 (22), 5633–5646.
Liu, Q., Ye, X., Chui, E.C.-s., Pu, Z., 2023. Impact of interface stress on responsive deformation of magnetic hydrogel. Int. J. Mech. Sci. 247, 108151.
Liu, X., Yang, Y., Inda, M.E., Lin, S., Wu, J., Kim, Y., Chen, X., Ma, D., Lu, T.K., Zhao, X., 2021. Magnetic Living Hydrogels for Intestinal Localization, Retention, and Diagnosis. Adv. Funct. Mater. 31 (27), 2010918.
Meng, Y., Li, C., Liu, X., Lu, J., Cheng, Y., Xiao, L.-P., Wang, H., 2019. Preparation of magnetic hydrogel microspheres of lignin derivate for application in water. Sci. Total Environ. 685, 847–855.
Miya, K., Hara, K., Someya, K., 1978. Experimental and Theoretical Study on Magnetoelastic Buckling of a Ferromagnetic Cantilevered Beam-Plate. J. Appl. Mech. 45 (2), 355–360.
Moon, F.C., Pao, Y.-H., 1968. Magnetoelastic Buckling of a Thin Plate. J. Appl. Mech. 35 (1), 53–58.
Nguyen, N.-T., Beyzavi, A., Ng, K.M., Huang, X., 2007. Kinematics and deformation of ferrofluid droplets under magnetic actuation. Microfluidics and Nanofluidics 3 (5), 571–579.
Ogden, R.W., Roxburgh, D.G., 1993. The effect of pre-stress on the vibration and stability of elastic plates. Int. J. Eng. Sci. 31 (12), 1611–1639.
Psarra, E., Bodelot, L., Danas, K., 2017. Two-field surface pattern control via marginally stable magnetorheological elastomers. Soft Matter 13 (37), 6576–6584.
Psarra, E., Bodelot, L., Danas, K., 2019. Wrinkling to crinkling transitions and curvature localization in a magnetoelastic film bonded to a non-magnetic substrate. J. Mech. Phys. Solids 133, 103734.
Rotjanasuworapong, K., Lerdwijitjarud, W., Sirivat, A., 2023. Dual electro- and magneto-induced bending actuators of magnetite-loaded agarose ionogels. Carbohydr. Polym. 310, 120741.
Rosensweig, R.E., 1985. Ferrohydrodynamics. Cambridge University Press.
Stewart, E.M., Anand, L., 2025. Magnetostriction of soft-magnetorheological elastomers. J. Mech. Phys. Solids 194, 105934.
Su, Y., Chen, W., Dorfmann, L., Destrade, M., 2020. The effect of an exterior electric field on the instability of dielectric plates. Proc. R. Soc. A: Math. Phys. Eng. Sci. 476 (2239), 20200267.
Su, Y., Conroy Broderick, H., Chen, W., Destrade, M., 2018. Wrinkles in soft dielectric plates. J. Mech. Phys. Solids 119, 298–318.
Su, Y.P., Chen, W.Q., Destrade, M., 2019. Tuning the pull-in instability of soft dielectric elastomers through loading protocols. Int. J. Non-Linear Mech. 113, 62–66.
Tang, J., Wei, H., Zhang, W., Lin, J., Yuan, C., Wang, T., 2025. Magnetothermal dehydration induced deformation of hydrogel structures: Modelling and experiment. J. Mech. Phys. Solids 197, 106061.
Thévenot, J., Oliveira, H., Sandre, O., Lecommandoux, S., 2013. Magnetic responsive polymer composite materials. Chem. Soc. Rev. 42 (17), 7099–7116.
Weiss, F., Cai, S., Hu, Y., Kyoo Kang, M., Huang, R., Suo, Z., 2013. Creases and wrinkles on the surface of a swollen gel. J. Appl. Phys. 114 (7).
Wu, B., Destrade, M., 2021. Wrinkling of soft magneto-active plates. Int. J. Solids Struct. 208-209 13–30.
Wu, J., Gong, X., Fan, Y., Xia, H., 2011. Physically crosslinked poly(vinyl alcohol) hydrogels with magnetic field controlled modulus. Soft Matter 7 (13), 6205–6212.
Xia, G., 2024. Wrinkling of compressible magnetic soft plates. Extreme Mech. Lett. 73, 102255.
Xia, G., 2025. Indentation on a constrained electroactive gel. J. Mech. Phys. Solids 197, 106045.
Xia, G., Su, Y., Chen, W., 2021. Instability of compressible soft electroactive plates. Int. J. Eng. Sci. 162, 103474.
Xia, G., Su, Y., Chen, W., 2025. Magnetoelastic surface Green's function and the stability of a soft magnetoactive half-space. Int. J. Eng. Sci. 214, 104289.
Yu, Z., Zhang, X., Huang, Y., 2013. Magnetic Chitosan–Iron(III) Hydrogel as a Fast and Reusable Adsorbent for Chromium(VI) Removal. Ind. Eng. Chem. Res. 52 (34), 11956–11966.
Zhao, X., Kim, J., Cezar, C.A., Huebsch, N., Lee, K., Bouhadir, K., Mooney, D.J., 2011. Active scaffolds for on-demand drug and cell delivery. Proc. Natl. Acad. Sci. 108 (1), 67–72.
Zhao, X., Suo, Z., 2007. Method to analyze electromechanical stability of dielectric elastomers. Appl. Phys. Lett. 91 (6), 061921.
Zrínyi, M., Barsi, L., Büki, A., 1997. Ferrogel: a new magneto-controlled elastic medium. Polymer Gels and Networks 5 (5), 415–427.